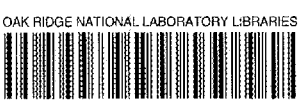

ORNL-TM-4368

cy. 1

TRANSPORT OF RESONANCE RADIATION IN ARGON

J. E. Talmage, Jr. (Thesis)
G. S. Hurst
M. G. Payne
E. B. Wagner

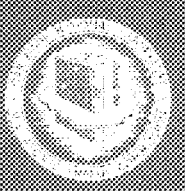

OAK RIDGE NATIONAL LABORATORY
OPERATED BY UNION CARBIDE CORPORATION • FOR THE U.S. ATOMIC ENERGY COMMISSION

ORNL-TM-4368

Contract No. W-7405-eng-26

HEALTH PHYSICS DIVISION

TRANSPORT OF RESONANCE RADIATION IN ARGON

J. E. Talmage, Jr., G. S. Hurst, M. G. Payne, and E. B. Wagner

Submitted by J. E. Talmage, Jr. as a dissertation to the
Graduate School of The University of Kentucky
in partial fulfillment of the requirements
for the degree of
Doctor of Philosophy

OCTOBER 1973

OAK RIDGE NATIONAL LABORATORY
Oak Ridge, Tennessee 37830
operated by
UNION CARBIDE CORPORATION
for the
U. S. ATOMIC ENERGY COMMISSION

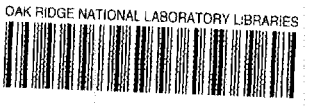

ACKNOWLEDGEMENTS

The authors wish to express their sincere thanks to J. P. Judish for operation and maintenance of the Van de Graaff accelerator and to J. T. Cox for the design of the reaction cell and related equipment for ionization measurements. The authors express gratitude to H. C. Schweinler, R. H. Ritchie, D. M. Bartell, J. E. Parks, T. E. Stewart, and H. L. Weidner for useful discussions and assistance with the experiment. The authors are indebted to E. T. Arakawa for the measurements of the lithium fluoride window transmission and several useful discussions on the properties of monochromators. The authors appreciate the help of the Radiation Physics and High Voltage staff members at Oak Ridge National Laboratory.

During the research work, one of the authors (JET) received financial support through the Laboratory Graduate Participation Program of the Oak Ridge Associated Universities.

ABSTRACT

The transport of resonance radiation in argon has been studied over a wide pressure range (0.002 to 600 torr). A line source of argon $^1P_1$ states was produced by a collimated, pulsed beam of protons traveling down the axis of a cylinder filled with a pure grade of argon. The time dependence of escaping resonance radiation was examined. The geometrical arrangement and initial conditions are simple, and a detailed comparison can be made between theory and experiment.

The basic assumptions of resonance transport theory have been examined for the $^1P_1$ state in argon, and it is found that revisions are required at lower pressures where collisions between excited atoms and ground state atoms are infrequent. Comparison between this experiment and theory shows a discrepancy of as much as a factor of three. A newer theory, which allows for coherent re-emission (in the rest frame of the atom) when no collision occurs during the lifetime of an excited state, is examined and found to be in reasonable agreement with the data. At higher pressures, the two transport theories give the same results and are in agreement with this experiment to within 10%.

The role of the transport of resonance radiation in the pathways taken by the energy deposited by the proton beam is examined. Various

effects are observed, and tentative explanations are presented for the behavior of the radiation escaping from the $^1P_1$ state. An estimate is made on the energy escaping near 1048 Å and in the continuum around 1250 Å and is found to be consistent with the model of Hurst and Thonnard.

TABLE OF CONTENTS

LIST OF TABLES

LIST OF ILLUSTRATIONS

SECTION 1

INTRODUCTION

1.1 Resonance Radiation

The transport of electromagnetic radiation in gaseous media has been under study for many years. It is fundamental to astrophysics, atmospheric physics, atomic physics, and other fields. An interesting and important part of this broad topic is the study of resonance radiation.[1] Resonance radiation occurs in a gas of identical atoms if these atoms have an excited state with two important properties: the energy of the state is sharply defined, and the transition to the ground state is both allowed and is the preferred mode of de-excitation. When an atom decays from such a state, the emitted photon will have that energy which enables another ground state atom to absorb it. Thus the photon will usually travel only a short distance before being absorbed and reemitted. Indeed, this trapping mechanism is often so efficient that a photon may be emitted and reabsorbed thousands of times before escaping to the walls of a container. The containment time and angular distribution of the escaping photons will depend in a detailed way on the emission and absorption probabilities of these photons (as a function of photon frequency). Measurements of the rate and intensity of escaping

resonance radiation will provide information on these probabilities and, in addition, provide a crucial test for assumptions on the correlation between absorption and reemission by the individual atom.

1.2 Theoretical Treatment

The first successful treatment of the transport of resonance radiation was achieved by Holstein[2,3] and Bieberman.[4] Earlier attempts,[5] based on the existence of a photon mean free path, neglect the rapid variation of the absorption coefficient with frequency in the neighborhood of a resonance line. Rather than using diffusion techniques, Holstein introduced an integrodifferential equation describing the time evolution of the spatial distribution of excited atoms in the gas. In this work, he restricted his analysis to the situation where there is no correlation between the frequency of the emitted photon and the previously absorbed photon (i.e., a complete redistribution of the emitted photon frequency occurs so that the emission probability and the absorption profile are proportional). Holstein examined the way in which this could occur in the case of Doppler and pressure broadening, and was led to the conclusion that the redistribution assumption was valid in both cases. He showed, if there is no correlation between absorption and reemission, that the mean free path must necessarily be infinite. This occurs because in the computation of the mean free path, an average over photon energy must be taken, and those photons

emitted far from the center of the resonance line give an unbounded contribution to this average.

Recently, Payne[6] and others[7,8] have examined the conditions required to attain the redistribution in frequency. Payne found that in the situation where 1) the probability of a decorrelating collision between an excited argon atom and a ground state atom is substantially less than unity and 2) there is sufficient trapping so that the frequency dependence of the wings is dominant in determining the photon transport, the complete redistribution in frequency assumption should fail. Careful attention must then be given to the difference in the emission and absorption profiles, and these differences could lead to a different trapping time than predicted by Holstein. A wide pressure region exists for the decay of the $^1P_1$ state in argon in which this situation is realized. Observation of the time dependence of the escaping photons which result from the decay of this state (near 1048 Å) provides a test for the complete redistribution assumption.

1.3 Experimental Implications

The transport of resonance radiation, aside from its intrinsic interest and its value in understanding fundamental processes, plays an important role in many aspects of the interaction of radiation with matter. Resonance trapping is likely to enter into any experiment where 1) photons are emitted into a narrow frequency interval by atoms on de-excitation to to the ground state and 2) the gas is sufficiently dense that the emitted

photon has little chance of escaping to a wall of the container without reabsorption.

Several problems in astrophysics fall into this category. Radiation escaping from a star must undergo many emissions and reabsorptions. Light traveling through nebulae will be scattered many times before emerging.

In the laboratory the study of gas discharges, microwave excitation, and charged particle excitation must take into account the effect of radiation imprisonment. This is most dramatically exhibited in the self-reversal of a resonance line in which very little light is observed escaping from the center of the line, while the wings of the emitted frequency distribution are greatly enhanced. In gas lasers radiation trapping may aid in attaining the desired inverted population.

In the study of the pathways taken by the energy deposited when a charged particle passes through matter, it is found that resonance trapping plays an important role. In experiments to examine these pathways, at the University of Kentucky and Oak Ridge National Laboratory, the noble gases have been selected as targets. An energetic beam of protons or electrons deposits a small amount of its energy in the gas. In helium[9] and argon[10,11] models have been developed which describe the pathways taken by this energy. A similar model is being developed for neon by Leichner.[12] These models are being constructed from an extensive series of experiments, which

provide information such as 1) W values of the pure gases and Jesse effects due to the addition of impurities,[13-15] 2) intensity of the light emitted in the vacuum ultraviolet (vuv) region as a function of wavelength and pressure,[16-18] the distribution in time of this radiation[9-11] and quenching due to the addition of impurities,[19] and 3) the fraction of energy lost by the charged particle which appears as vuv radiation.[20] These experiments thus reveal many aspects of the atomic excitation and ionization processes which occur and provide valuable tests for the various energy pathway models.

1.4 Objectives of this Work

The objectives of this work are to provide experimental information on the transport of the 1048 Å resonance radiation in argon, and to critically test radiation transport theories.

In the experiment, argon is allowed to flow through a cylindrical cell while bursts of protons traverse the cell along its axis. The argon $^1P_1$ resonance level is populated along the path of each proton. (According to the optical approximation, fast charged particles will excite an atomic level in proportion to its oscillator strength which is large for the $^1P_1$ level.) This provides a source of resonance photons distributed along the axis of the cylinder, which in time will escape to the walls or be converted to some other form of energy. The intensity and time dependence of the escaping radiation are measured over a wide range of argon pressures.

At lower pressures, the case where collisions between excited atoms and ground state atoms are negligible is studied. Here the escape of resonance photons will be governed by the Voigt profile (the convolution of natural and Doppler broadened profiles) so that the effects of radiation imprisonment can be examined without other complicating factors. As the argon pressure is increased, the line profile changes as pressure broadening becomes important. Two- and three-body effects become evident, opening up other pathways for the destruction of the $^1P_1$ resonance level. With an understanding of the transport phenomenon, more insight should be obtained into these other effects.

Careful attention has been given to obtaining a simple geometrical arrangement. The application of resonance transport theory in the past has been hampered by either 1) the lack of information on the initial spatial distribution of excited atoms (gas discharge work) or 2) the difficulty involved in trying to realize experimental boundary conditions which are theoretically tractable. The transport problem in cylindrical geometry has been solved,[21] so by using proton beam excitation the present experiment should overcome both of these difficulties.

In summary, this experiment undertakes to satisfy two goals. One is to reveal the extent to which the transport theories of Holstein and Payne are applicable to the 1048 Å resonance radiation in argon and to examine the basic implications of any differences. The other goal is to

understand the role of the transport of resonance radiation in the energy pathways studies.

SECTION 2

EXPERIMENTAL METHOD

2.1 Introduction

The apparatus used in this experiment is shown in Figure 1. Argon gas flows continuously through the cylindrical reaction cell. Bursts of protons from the ORNL 3-MeV Van de Graaff accelerator pass through an entrance foil, traverse the cell along its axis, then stop on striking the back plate of the cell. The interaction between the protons and the gas ionizes many argon atoms and excites the atomic levels in many others. Occasionally a photon escapes from the gas, passes through a lithium fluoride window, is dispersed by a monochromator and detected by a single photon detector. The proton pulse passes through a timing pick-off unit before entering the cell. To measure the time behavior of the emitted photons, the signal from this unit and the signal from the photon detector are fed to a time-to-pulse-height converter (TPHC) which provides a signal whose amplitude is proportional to the time between input signals. The output signal from the TPHC is analyzed and stored in a multichannel analyzer. This mini-experiment is repeated until many thousands of counts have been

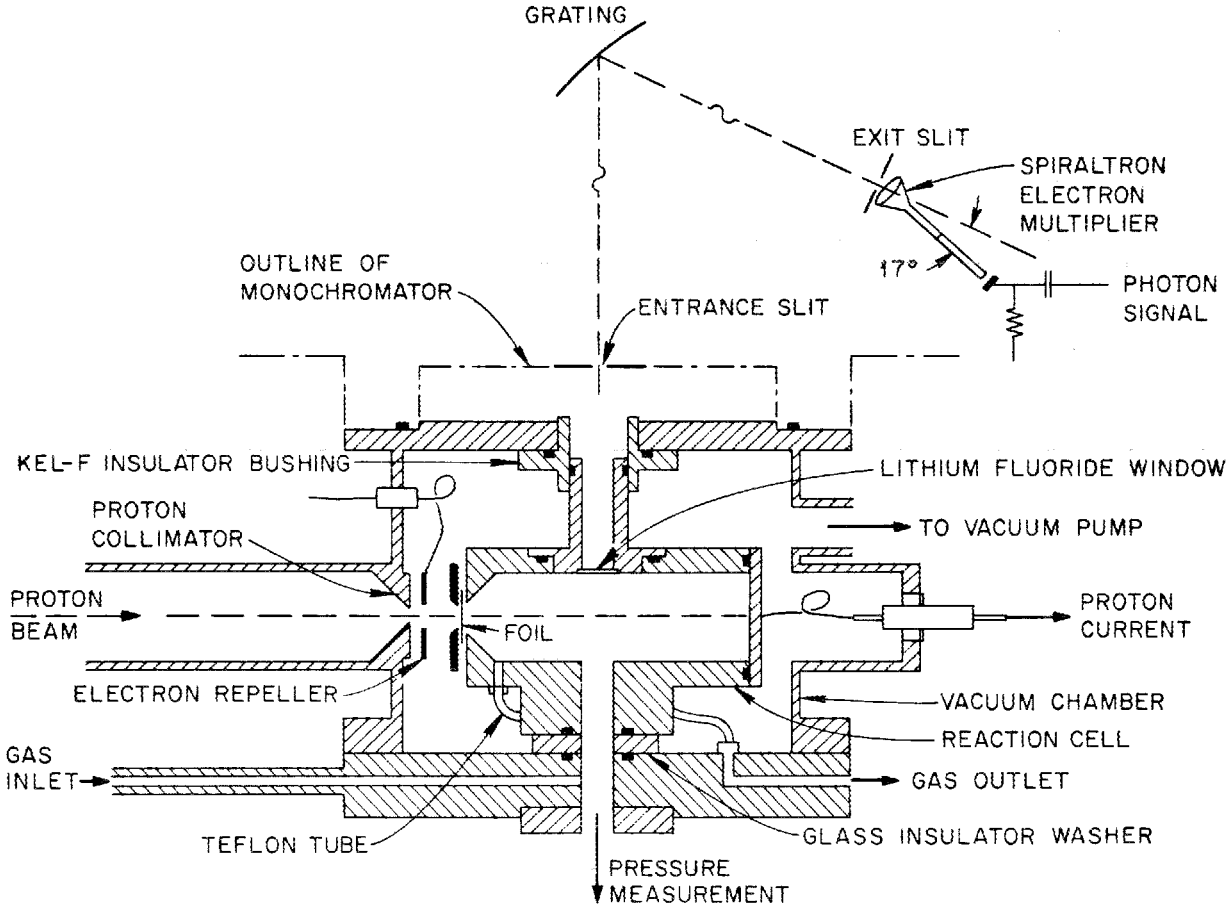

Figure 1. The Reaction Cell and Environs.

stored in the analyzer. The number of counts per unit time plotted against channel number gives the time distribution of the emitted photons.

Vacuum ultraviolet emissions from the noble gases have been examined using various methods for the initial excitation of the gas atoms: electric discharges,[22-24] light absorption,[1,7] and microwave excitation.[25] Recently, G. S. Hurst and co-workers[15,16,18,26,27] examined the use of fast charged particles for this purpose and found several advantages over the other methods. 1) The emission spectra of the noble gases are quite reproducible, whereas with discharge techniques the spectra depend on the conditions in the discharge. When fast charged particles are used, the amount of ionization and the relative population of the various excited states are probably determined by the oscillator strengths of the states (optical approximation[28]). Excitation by gas discharge produces many low-energy electrons which excite the atomic levels in a complex way. Some simplification in interpretation of the emission spectra should then be possible when fast charged particles are used. 2) Fast charged particle excitation can produce a clearly defined initial spatial distribution of excited states. The use of intense light sources to populate the desired atomic levels suffers in this respect due to scattering of the incident beam.

In view of these favorable aspects, it is feasible to do experiments (using fast charged particle excitation) on the transport of resonance radiation which can be compared with transport theories. Collimated fast

protons, passing along the axis of a cylindrical container of argon, can be used to excite the $^1P_1$ level of this atom. The subsequent decay of the excited atoms then produces a nearly line source of 1048 Å resonance photons whose transport properties can be analyzed theoretically.[21]

2.2 The Experimental Apparatus

In the experiment, 2.02 MeV protons were used from the ORNL 3 MeV Van de Graaff accelerator. This energy was sufficiently high to satisfy the requirements of the experiment, yet low enough to insure stable operation of the accelerator.

The proton beam was pulsed before leaving the terminal by sweeping the beam across an aperture. This produced a pulse whose duration was less than 20 nsec FWHM and less than 50 nsec at the base. The repetition rate of the pulses could be varied in discrete steps from 3.91 kHz (1/256 μsec) to 250 kHz (1/4 μsec). In most of the experiments, a repetition period of 64 or 128 μsec was used. At 64 μsec, the time averaged current through the reaction cell was about 0.06 μamp. This implies about 2×10^7 protons per pulse. The proton pulses could be further bunched to a FWHM of 2 nsec.

Before entering the reaction cell, the pulses were focussed by magnetic quadrupole coils, and 75% to 90% of the beam passed through a 3 mm diameter collimator. The protons entered the cell through a

0.0001 inch havar foil which covered an aperture of 6 mm diameter (see Figure 1). The protons were stopped by the back plate of the cylinder. Inspection of foil and back plate discoloration produced by the proton beam indicated the beam was well collimated along the cylindrical axis.

The reaction cell was a stainless steel cylinder, 7.0 cm in length and 1.11 cm in radius. Resonance radiation, escaping to the walls of the container, entered the dispersing monochromator via a 0.714 cm diameter cylindrical aperture halfway down the length of the cell. The axis of this aperture was perpendicular to the axis of the cell. To prevent argon from flowing into the monochromator chamber, a lithium fluoride disc was placed across the aperture flush with the wall of the reaction cell. The lithium fluoride window had to be replaced every few weeks due to the deterioration of its transmission efficiency at 1048 Å. This deterioration is probably due to formation of color centers when lithium fluoride is exposed to radiation in the vuv.[29] The thickness of the discs used varied from 1/2 to 1 mm; the diameters were 1/2 inch. Additional apertures were present in the cell to facilitate gas flow and pressure measurements (see Figure 1).

From stopping power data,[30] 2.02 MeV protons lose 0.20 MeV on the average in a nickel foil 0.0001 inch thick. The resulting 1.82 MeV protons have a range in argon at 684 torr of 7.0 cm (the cell length). Below argon

pressures of 100 torr, the total energy deposited by a proton in traversing the cell is given by $\Delta E = 1.66 \times 10^{-3}$ P (torr) in MeV.

The cell was isolated electrically from the surrounding hardware; the proton current was monitored by a contact from the back plate of the cell leading to a current digitizer or micro-microammeter. To insure accurate current measurements, electrons ejected from the havar foil after bombardment must be prevented from permanently escaping the cell. An electron repeller maintained at -100 V accomplished this.

Photons, on passing through the lithium fluoride window, were dispersed by a McPherson model 235 (1/2 meter) scanning monochromator which employs a Seya-Namioka geometrical arrangement.[31] The Bausch-Lomb diffraction grating had 600 grooves per millimeter and was blazed at 1500 Å. The reflecting area of the exposed region of the grating was 2.54 cm across by 2.8 cm high. In this geometry, the entrance and exit slits were located 50 cm from the grating. Each slit had a fixed height of 1.0 cm; the width could be varied. The entrance slit was set at 50 microns throughout the experiments. Exit slit widths from 40 to 350 microns were used in various parts of the experiment. With 10 torr argon pressure in the reaction cell, the width of the 1048 Å resonance line ranged from 4.5 to 16 Å as this exit slit was opened from 50 to 350 microns. The monochromator chamber was maintained at a pressure of less than 10^{-6} torr during all experiments in which the lithium fluoride window was used.

A Bendix Spiraltron Electron Multiplier (SEM Model 4219X),[32] mounted directly behind the exit slit, was used to detect the photons. The cone of the SEM had a base diameter of 1.0cm. To prevent "bore sighting," the SEM was mounted at an angle of 17° to the axis of the monochromator exit arm.

Pressure measurements in the reaction cell were made with an MKS Baratron capacitance manometer. Pressure heads of Type 77H-10 and Type 77H-1000 were used in their respective pressure ranges.

Grade 5 argon (purity 99.999%) was used; a typical impurity analysis gave (in parts per million) 1-H_2, 4-N_2, 1-O_2, 1-CO + CO_2, 1-THC, 1-H_2O. Gas from the argon tank was reduced in pressure by an ultra-high purity regulator, and flowed through a short stainless steel line to the reaction cell. The gas left the cell via a short teflon tube (needed for electrical insulation) and was removed by either a diffusion pump or roughing pump as required by the gas pressure. Valves before and after the reaction cell allowed one to control the pressure and flow rate.

To insure gas purity during an experiment, the gas lines and beam pipe plumbing were evacuated and maintained at low pressure for several days before experimental data were acquired. A pressure of 3×10^{-6} torr or less was obtained at the ion gauge on the beam pipe. Pressures would be somewhat higher in the distant recesses of the system. To further insure purity, the argon was allowed to flow at higher pressures for at least an

hour before attempting a low pressure experiment. A few experiments at the end of the series were performed without this latter precaution and gave slightly higher results for photon escape rates.

2.3 The Electronics

A schematic diagram of the electronic apparatus is shown in Figure 2.

The timing pick-off for the proton pulse, located above the analyzer magnet, was a hollow cylinder 12 inches long and 1 inch inside diameter. A pulse, on entering the cylinder induced a signal which was amplified and used as an input to the time-to-pulse-height converter (TPHC). A signal of the opposite polarity was induced as the pulse left the cylinder. A fast discriminator (Disc No. 1) in this circuit eliminated extraneous signals, in particular the signals generated by the slower singly ionized H_2 and H_3. (These ions were later eliminated at the analyzer magnet.) An alternate pick-off cylinder was available for use on the more sharply bunched pulses. It was 3 cm long and 1.2 cm in diameter. The proton current which passed through the reaction cell was monitored by either of two methods: directly by a Keithley 410 micro-microammeter or by an Ortec current digitizer plus Ortec timer-scaler (Scaler No. 1).

Photons, which escaped from the reaction cell into the proper solid angle and with the selected wavelength, could trigger the Spiraltron Electron Multiplier (SEM). As supplied by Bendix, the Model 4219X required some

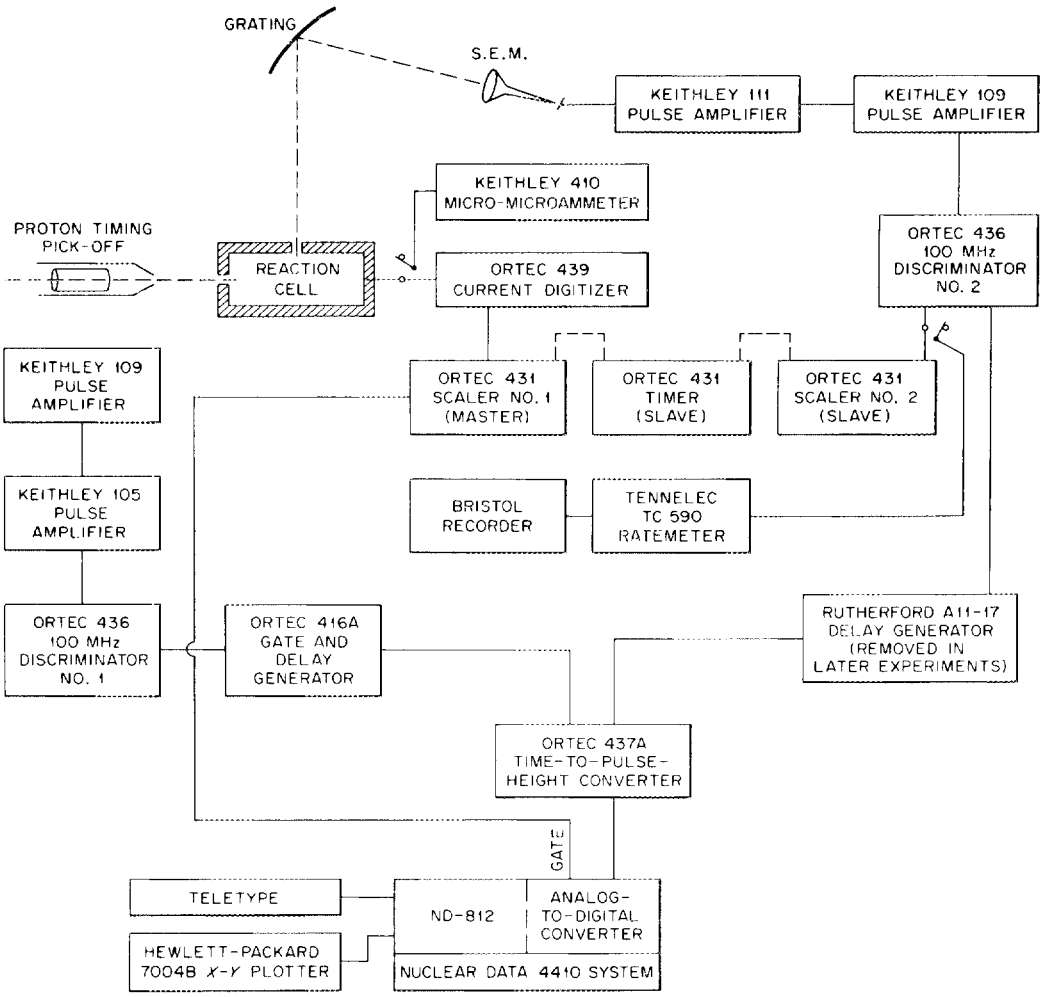

Figure 2. Electronics for the Time Dependent and Time Integrated Experiments.

circuitry to apply the necessary voltages and obtain an output signal. Figure 3 illustrates the SEM and circuitry.[33] To operate the SEM satisfactorily in the pulse saturation mode, applied potentials of 800 V (V_2) and 3700 V (V_1) were required. The potential drops along the preamplifier and spiraltron sections were then calculated to be 805 V and 2350 V, respectively. (Test data from Bendix on this particular SEM show a gain of 1.4×10^8 with these potentials at 800 V and 2200 V, respectively.) To collect the amplified electron pulses as they emerged from the high voltage end of the SEM, a brass button (collector plate) was placed 1 mm behind the last section. To insure collection of the electrons, the collector plate was maintained at about 210 V above the SEM terminal by a bleeder circuit. The signal from the SEM went to a Keithly 111 pulse amplifier for impedance matching (see Figure 2), then to another amplifier followed by a discriminator (Disc No. 2).

For direct intensity measurements, the positive output of Disc No. 2 was sent to either an Ortec timer-scaler (Scaler No. 2) or to a rate-meter which then drove a Bristol recorder. The latter mode was used together with the monochromator grating drive to obtain the intensity versus wavelength data.

To measure the time distribution of photons, the negative output of Disc No. 2 was fed through a delay generator to the TPHC. (In the later experiments, the delay generator was not used as it was the limiting factor for the time resolution.) The output signal from the TPHC was then

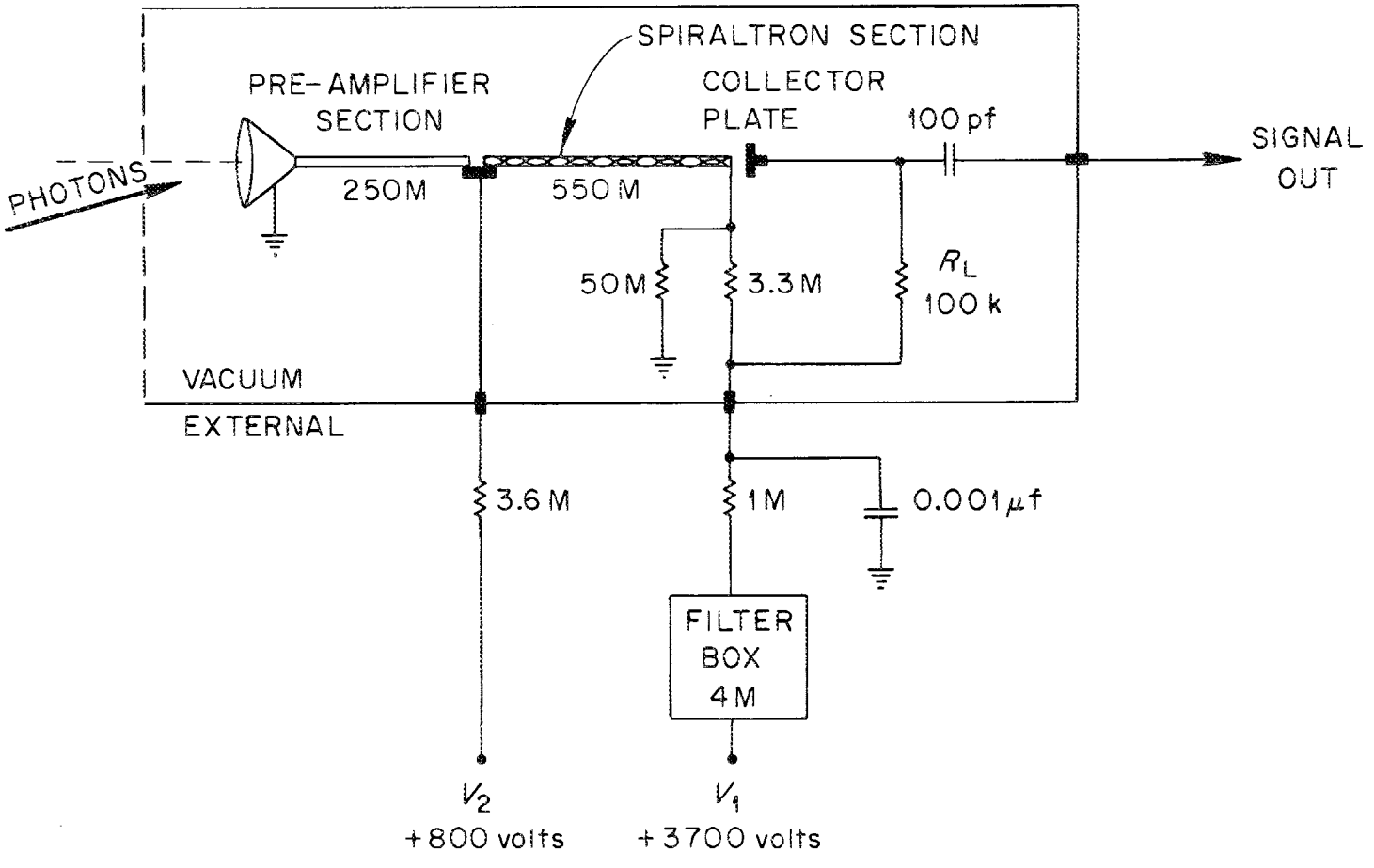

Figure 3. SEM Photon Detector and Circuitry.

analyzed and stored by a Nuclear Data 4410 single parameter data acquisition system. This system included an analog-to-digital (ADC) module, an ND-812 computer, a control module, and a Tektronix oscilloscope. The data were later recalled via a teletype and an X-Y plotter.

The digitized proton current (Scaler No. 1) served as master in controlling the accumulation of counts, both for the direct photon count (intensity) and the time-dependent intensity measurements. In this way, all data were normalized to the number of incident protons.

2.4 Experimental Techniques

To study the transport of resonance radiation, two entities were measured as a function of pressure: 1) the distribution in time of 1048 Å photons escaping to the walls of the container (time-dependent intensity), and 2) the net, time-integrated number of the escaping 1048 Å photons which are detected (relative intensity).

In the relative intensity measurements, the quantity obtained was the number of 1048 Å photons (per incident proton) which escaped from the reaction cell into the appropriate solid angle, were transmitted by the lithium fluoride window, dispersed by the grating, detected by the SEM, and finally counted by the electronics. Considerable care must be taken to insure that each one of these agents does not distort the data taken at different pressures and at different times. Some typical problems are discussed below.

1. The transmission coefficient of lithium fluoride at 1048 Å decreases over a period of weeks when exposed to vuv radiation and electron fluxes.[29,34] This problem is easily eliminated by only comparing data taken over short time spans, then normalizing the different data sets at overlapping pressures.
2. This transmission coefficient is temperature sensitive, decreasing as the window is warmed.[35] There is some experimental evidence that this effect is occurring at higher pressures for high beam currents. (A rough calculation shows that at a proton beam current of 0.6 μamp, the reaction cell temperature may rise 4°C if most of the proton energy is lost at the back plate of the cell.)
3. This transmission coefficient increases toward longer wavelengths. This becomes an important effect in the pressure region 10 to 300 torr as the argon 1048 Å line shifts to 1052 Å.[15] Correction is made for this.
4. The slit settings on the monochromator and the grating angle must be adjusted to insure that the shifting and broadening of the 1048 Å lines with pressure do not introduce error. The exit slit was opened wide enough to collect all light from the 1048 Å region at the higher pressures (it was possible to do this without admitting light from the 1067 Å region). The shift in the

peak was monitored and the grating then rotated to the mid-point of the peak.

5. The SEM exhibits a drop in gain at higher counting rates;[36] this causes an increased fraction of the counts to be blocked by the discriminator (Disc No. 2) even in the pulse saturated mode. This effect was more severe in the SEM used in this experiment than described in Reference 36; however, below 1000 counts per second, it was negligible.

In the time-dependent intensity measurements the above problems were not important. A change in photon counting efficiency over times which are long compared to microseconds (characteristic decay time of the resonance radiation) will not be reflected in the rate measurements.

Two modes of operation for the time-to-pulse-height converter (TPHC) were employed in determining the photon escape rates. In the "forward time" mode, the proton timing pick-off signal started the TPHC ramp; the first photon detected by the SEM terminated the ramp. The "reverse time" mode used the photon signal to start the TPHC. The signal from the proton pulse which occurred immediately before this photon was suitably delayed in time and used to stop the ramp. In an experiment when the "effect events" occur only infrequently in comparison to the "cause event," the reverse time mode eliminates dead time at the TPHC. In the present case, the ratio of photons detected to incident proton pulses ranged

from 1/20 to 1/2000 and the reverse time mode was generally used. To insure simple interpretation of the data, the number of photons detected must be much less than the number of proton pulses. The delay time selected for the proton pulse (on the Ortec 416A gate and delay generator) was roughly equal to the full scale time setting on the TPHC. Ideally this delay should be equal to this full scale setting, but fixed delays in the electrons plus the desire to avoid use of the highest several channels of the multichannel analyzer modified this.

In an experiment of this type, the precise moment ($t = 0$) when the proton beam enters the cell is not directly useful. The quantity to be determined is the conversion factor between a true time interval and the channel width in the multichannel analyzer (MCA). To determine this number for fixed TPHC and MCA settings, an ORNL mercury "Q" pulser supplied a simultaneous signal (suitably shaped) to both discriminator inputs (Disc No. 1 and Disc No. 2). Then fixed delays were introduced in increments by either the Ortec or the Rutherford delay generators and the size of the resulting TPHC pulse recorded in the MCA. A plot of induced delay versus resulting channel number checked the linearity of the electronic response and provided the desired conversion factor. There was no deviation from linearity over the range of channels actually used in the MCA. The conversion factor, checked several times a day, generally remained constant over days or even weeks. The Rutherford and Ortec delay generators

gave results which differed by less than 1%. The Rutherford generator was originally placed in the experiment to provide accurate digital settings for this calibration. The Ortec settings were made by a variable resistor. However, the Rutherford delay generator was found to be the limiting factor in the time resolution, and as the settings on the Ortec delay generator could be made in a repeatable way, the Rutherford generator was removed.

A rough attempt was made to determine the inherent time resolution of the experiment. Nitrogen gas was flowed through the reaction cell. On bombardment by protons, an atomic state was populated which then decays by photon emission at 1200 Å with a decay rate of about 2 nsec.[37] The observed time-dependent intensity is shown in Figure 4 with and without the Rutherford generator. The electronic arrangement shown in Figure 2 was used. In a particular experiment, the actual resolution depends on the TPHC and MCA settings.

For the single photon counting technique used in this experiment, the probability that two or more photons arrive at the detector during one beam repetition period must be negligibly small; otherwise, a bias would exist favoring early photons. From Poisson statistics, an average rate of 1 photon for every 6.7 proton pulses yields a probability of 0.01 that more than 1 photon is detected between proton pulses. As mentioned earlier, the photon rate never exceeded 1 photon in 20 proton pulses.

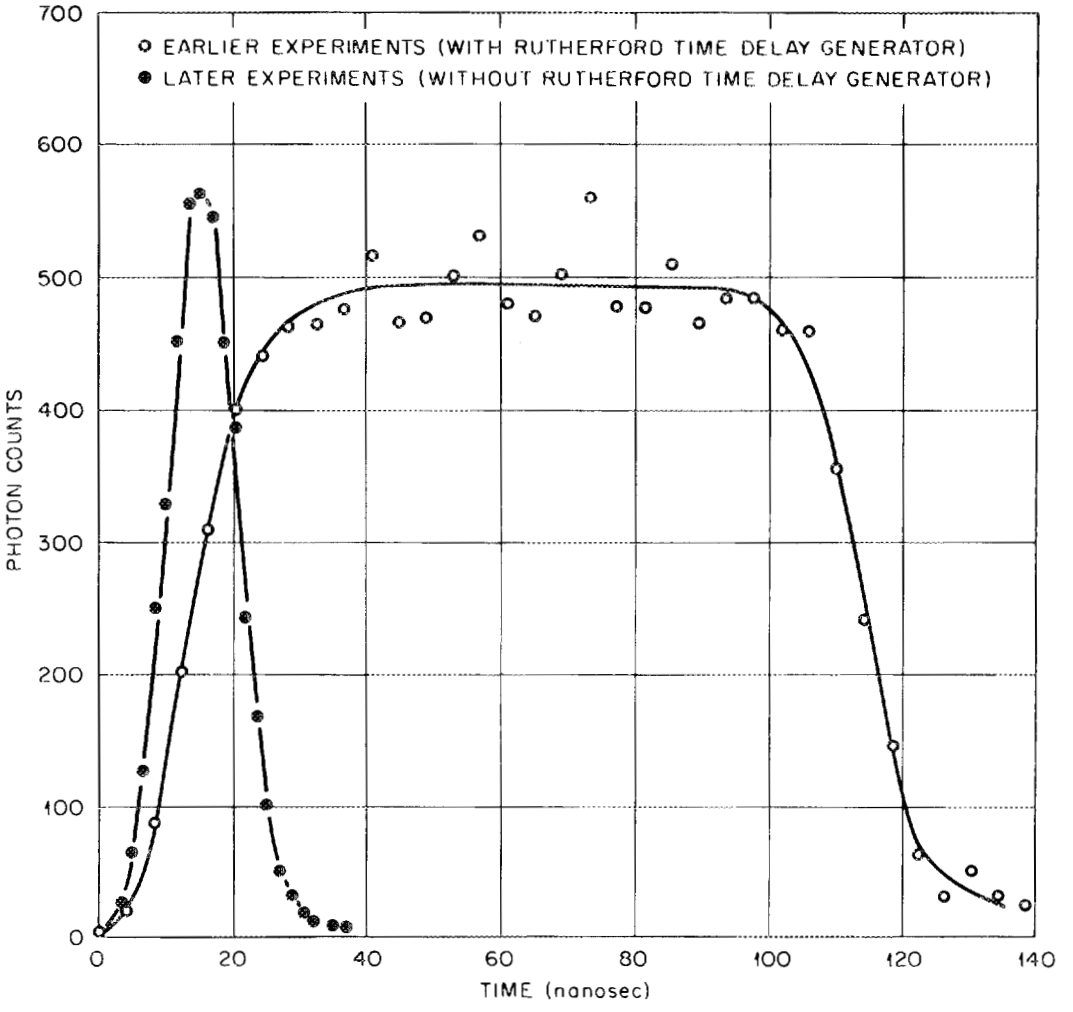

Figure 4. Time Resolution of the Lifetime Apparatus.

The time-dependent intensity data were analyzed by hand fitting and by using the ND-812 computer.[38] There were no detectable differences between the two methods.

SECTION 3

TRANSPORT OF RESONANCE RADIATION AT LOW PRESSURES

As mentioned in the Introduction, one primary objective of this thesis is the study of the resonance trapping phenomenon over as wide an argon pressure range as experimentally feasible. It is desirable to obtain information at low pressures where complicating effects do not obscure the transport process. For example, above 10 torr the recombination of electrons with argon ions produce a source of 1048 Å photons which extend over a long period of time. Also, above 10 torr, collisions (mainly 3-body) between $^1P_1$ excited argon states and ground state argon atoms channel the energy along additional pathways.[10] Further, a substantial shift is observed in the wavelength of escaping photons as one increases the pressure above 10 torr.[16] These effects are less important below 10 torr. It is thus convenient to separate this study into two pressure regions: 1) 0.0015 torr $\leq$ P $\leq$ 10 torr which will be examined in this section and allowing some overlap, 2) 1 torr $\leq$ P $\leq$ 600 torr to be examined in Section 4.

The 1048 Å emission line of argon is an excellent resonance line for this study for the following reasons: 1) the associated $^1P_1$ atomic level is easily excited by fast charged particles due to its large oscillator strength

(optical approximation); 2) the level has no complicating fine structure; 3) the level is isolated from other excited states; and 4) the emitted 1048 Å photons are transmitted by a lithium fluoride window so that differential pumping is not required and one has a well-defined geometry.

3.1 The Low Pressure Data

Typical data curves for the pressure region 0.0015 torr $\leq P \leq$ 10 torr are shown in Figure 5. The relative photon count detected by the SEM is plotted on a log scale versus time (measured from the proton pulse) as resolved by a multichannel analyzer (MCA). The SEM background count has been subtracted. The slope on the semi-log plot was observed to be nearly linear at the lower pressures. At higher pressures (see 5.25 torr data in Figure 5), a single exponential would not accurately describe the data as at late times the photon escape was somewhat slower. This effect will be discussed in more detail shortly. The early time slope was extracted by observing a computer fit obtained by adding one later channel at a time until the slope began to change. Figure 6 and Table 1 give the values of the early time escape rate obtained in this way. The late time escape rate is only measurably distinct from the early time rate above 0.5 torr. Extracting this slope from the data, it is found to be nearly constant ($\beta_L = 0.32 \times 10^6$ sec^{-1}) over the pressure range 0.58 to 5.25 torr.

The proton current was monitored, enabling one to obtain the relative time-integrated count (referred to as intensity in the following) as

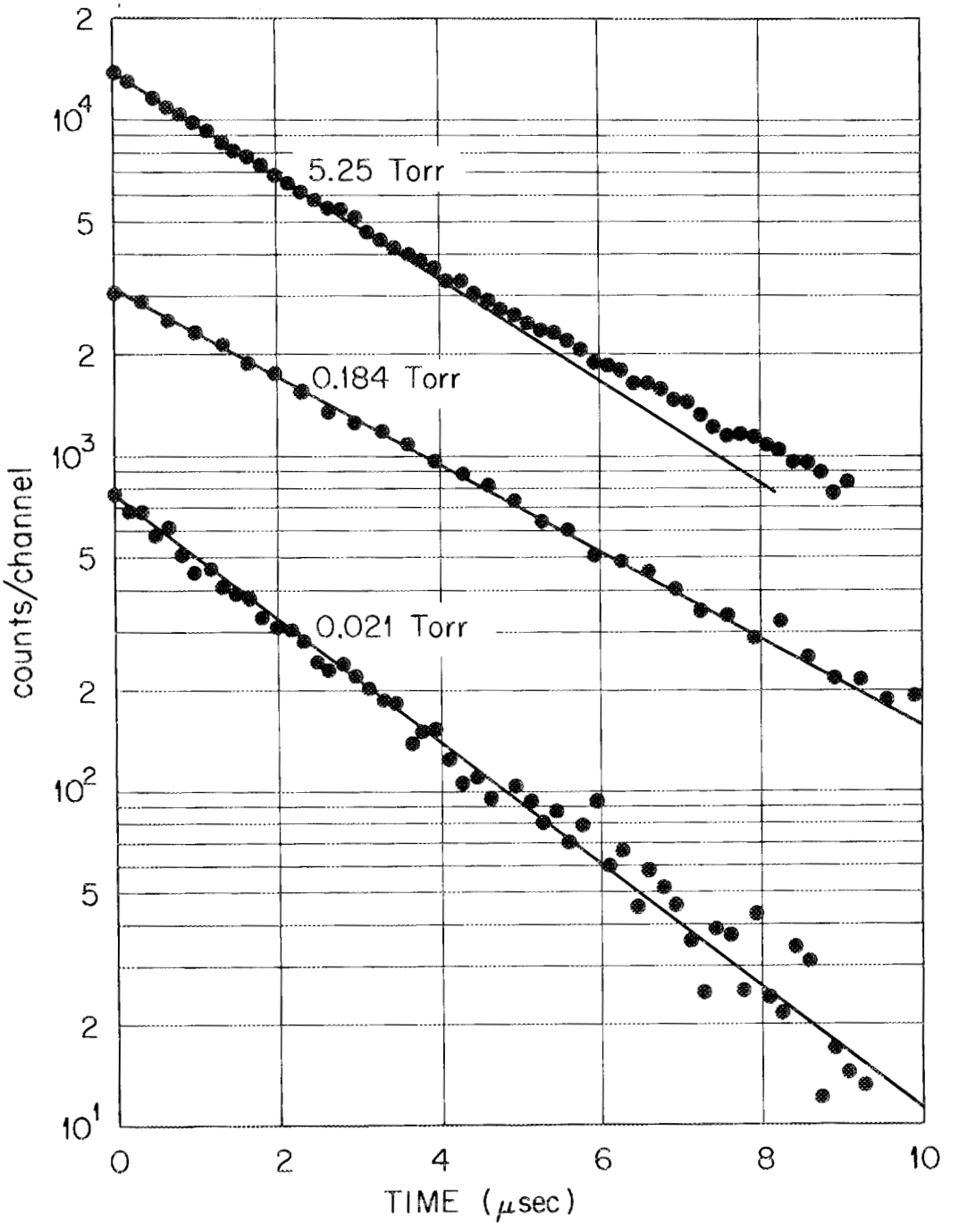

Figure 5. Decay Curves for Argon 1048 Å Resonance Radiation at Several Low Pressures.

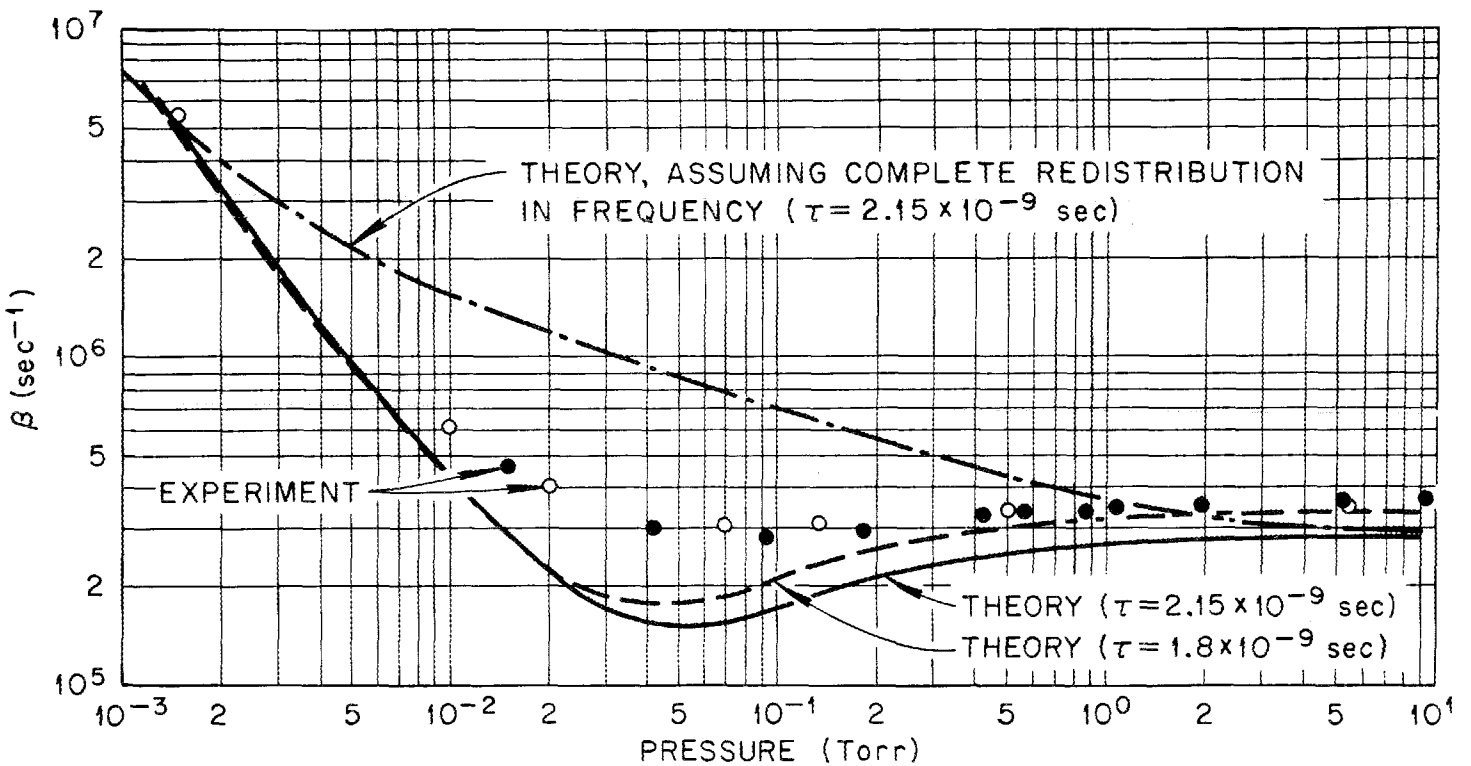

Figure 6. Experimental and Theoretical Early Time Escape Rates for the Argon 1048 Å Resonance Radiation at Low Pressures.

TABLE 1

EXPERIMENTAL EARLY TIME ESCAPE RATES FOR THE ARGON 1048 Å ($^1P_1$) RESONANCE EMISSION AT LOW PRESSURES

Run No.	Pressure (torr)	Escape Rate (μsec^{-1})
103	9.35	0.377
217	5.25	0.358[a]
208	5.19	0.358
207	5.17	0.368
176	1.94	0.361
173	1.07	0.354
125	0.86	0.339
175	0.57	0.345
129	0.56	0.337
244	0.50	0.344[a]
182	0.41	0.330
180	0.184	0.293
220	0.135	0.319[a]
194	0.093	0.283
224	0.069	0.316[a]
197	0.042	0.310
238	0.0206	0.382[a]
151	0.0147	0.468
242	0.0100	0.620[a]
249	0.0015	5.4[a]

[a] See text for comment on this later experiment.

a function of argon pressure. This intensity was obtained simultaneously in two ways: 1) a scaler monitored the photon count directly, and 2) the MCA channels were summed. At these pressures, the count rate was low enough that no correction was needed for MCA dead time. The SEM background was significant (exceeding the true count rate at the lowest pressures), but one could easily subtract it from the time-resolved data. The scaler photon count rate (photons/sec) was monitored carefully during the relatively long time periods required to accumulate the data as a check on the stability of operating conditions; it remained remarkably constant in the experiments reported here.

Figure 7 shows, on a log-log scale, the intensity versus argon pressure for the 1048 Å line. As pointed out in Section 2, intensity measurements made at different times cannot be compared directly due to changes in the lithium fluoride window transmission efficiency. However, the various experiments below 10 torr were quite consistent with the least square fit to obtain

$$I = \text{constant} \times P^{1.31} , \tag{3.1}$$

where the constant depends on the geometry of observation and on the efficiencies of the window, grating, and SEM. The data shown in Figure 7 have been normalized by choosing the constant so that the intensities are equal at 5.0 torr. This non-linear variation of the intensity with pressure is examined immediately following Equation (3.19).

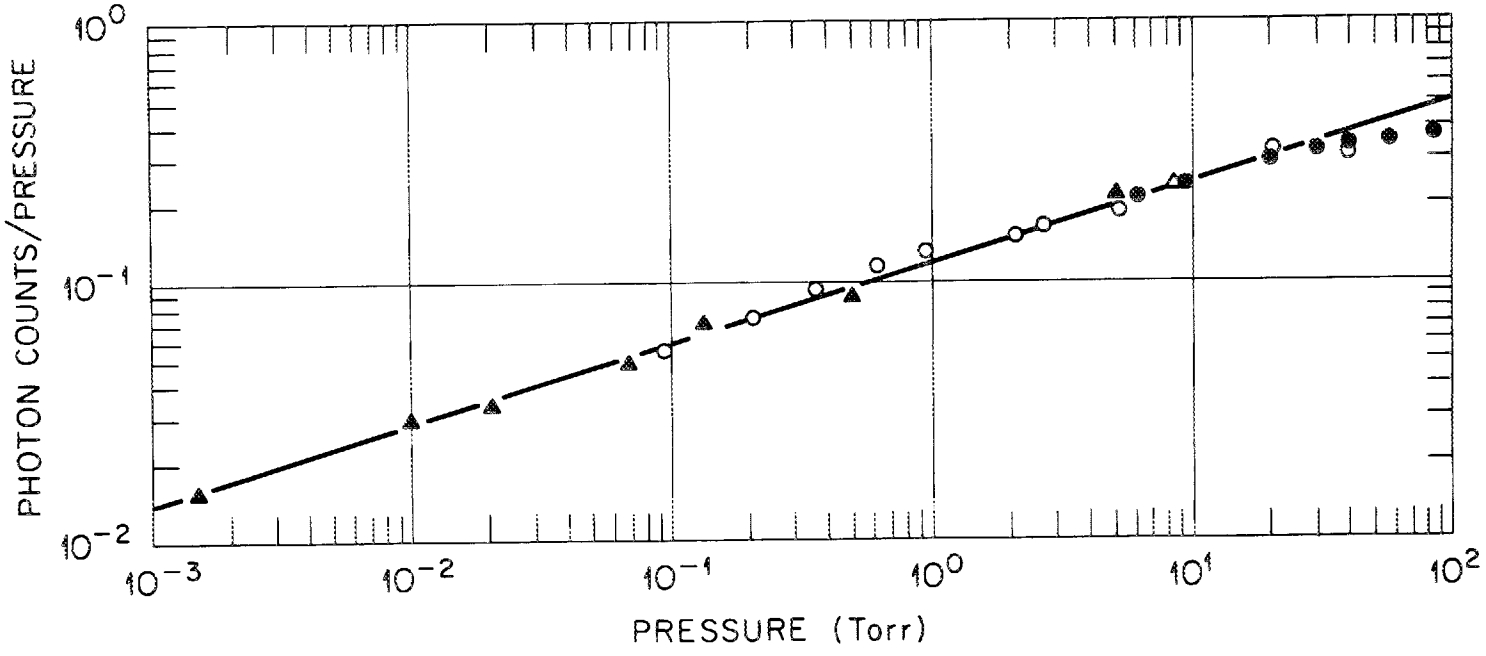

Figure 7. I(P)/P versus Pressure for the Argon 1048 Å Resonance Radiation at Low Pressures.

3.2 Theory of the Transport of Resonance Radiation

Holstein[2,3] has examined the transport of resonance radiation based on the assumption of complete redistribution in frequency for each photon absorption and re-emission. He demonstrated that at sufficiently high pressures (so that a collision between an excited atom and a ground state atom was very probable during the natural lifetime of the excited state) a correct description of the transport process results if one assumes that

$$P(\nu) \propto k(\nu) , \tag{3.2}$$

where $P(\nu)$ is the emission profile and $k(\nu)$ is the absorption coefficient. Holstein also demonstrated that at sufficiently low pressures so that escape of resonance photons was determined by the Doppler profile alone, the same assumption was quite reasonable. Walsh[39] then attempted to interpolate between these pressure regions by choosing an expression for the escape rate which approached the Holstein values in the high and low pressure limits.

Recently, Payne[6] has attacked the transport problem by allowing for a correlation between absorbed and then emitted photon frequencies in the situation where there is no perturbation by another atom of the excited state during its natural lifetime. As this approach is in better agreement with the data than the Holstein formulation and since it is felt that the interpretation of the data in terms of this picture leads to a fundamental

understanding of the transport process, a brief discussion of Payne's work is now given. The discussion will be limited to the situation where pure argon is in a small container at a pressure less than 10 torr. The number of excited $^1P_1$ atoms at any time is only a small fraction of the total number of argon atoms.

Define a distribution function $N(\vec{r}, x, t)$ such that

$N(\vec{r}, x, t)\,dV\,dx$ = the number of excited atoms in volume dV at $\vec{r}$ at time t which will emit (in the future) into the frequency range x to $x + dx$.

In this definition, $x = (\nu - \nu_o)\, c/V_o \nu_o$ where c = speed of light, $\nu_o = c/\lambda_o$ = frequency at the center of the resonance line, and $V_o = \sqrt{2RT/M}$.

Define the angle averaged redistribution function $R(x', x)$ such that

$R(x', x)dx\sqrt{\pi}\, k_o\, ds$ = the probability that a photon of frequency x' will be absorbed while traversing the distance ds and re-emitted between x and $x + dx$,

where $k_o = \dfrac{\lambda_o^3}{8\pi^{3/2}} \dfrac{g_2}{g_1} \dfrac{N}{\tau V_o}$; $\dfrac{g_2}{g_1}$ = relative statistical weights of the excited and ground state, respectively; N = density of argon atoms; and $\tau = 1/\gamma$ = natural lifetime of the excited state.

The absorption coefficient can be written

$$k(x) = \frac{k_o a}{\pi} \int_{-\infty}^{\infty} \frac{e^{-y^2} dy}{(x - y)^2 + a^2} \sim k_o \left(e^{-x^2} + \frac{a}{\sqrt{\pi}\, x^2} \right), \qquad (3.3)$$

where $a = \frac{\lambda_o}{4\pi V_o}(\gamma + \gamma_c)$; $\gamma_c = 0.904\,\gamma \frac{g_2}{g_1}\frac{N\lambda_o}{6\pi^2}$ is a measure[40] of the collision rate between an excited argon atom and a ground state atom. For the 1048 Å line in argon at 293°K, assuming a natural lifetime $\tau = 2.15 \times 10^{-9}\ \text{sec}^{-1}$,[41] one obtains the following values: $g_2/g_1 = 3$, $V_o = 3.49 \times 10^4$ cm/sec, $a_o = \lambda\gamma/4\pi V_o = 0.0111$, $\gamma_c/\gamma = 1.737P$, $k_o = 34.0 \times 10^3\,P$, $a = a_o(1 + \gamma_c/\gamma)$ where P = pressure in torr.

One can then develop an equation in terms of $R(x',x)$ which describes the time behavior of $N(\vec{r},x,t)$. Assuming a source function of the form $F(\vec{r},x)\delta(t)$, one obtains

$$\frac{\partial N(\vec{r},x,t)}{\partial t} = -\gamma N(\vec{r},x,t) + \gamma\sqrt{\pi}\,k_o \int_{-\infty}^{\infty} dx' \int_V \frac{N(\vec{r}',x',t)\,R(x',x)\,e^{-k(x')\,|\vec{r}-\vec{r}'|}}{4\pi\,|\vec{r}-\vec{r}'|^2} dV' \tag{3.4}$$

where V is the volume of the gas container.

In studying this equation, Payne has confined himself to the experimental situation where resonance photons are escaping from the region between two infinite parallel planes separated by the distance y_o (slab geometry) when a distribution of excited states initially (t = 0) is located in the plane at the center of the slab. The present geometry is appreciably different from this, but it will be shown presently that at sufficiently early times after the proton pulse, the slab geometry is appropriate.

Also, the theory requires that the pressure be sufficiently high that there is strong trapping at the center of the resonance line.

The redistribution function can be written in the following way:

$$R(x',x) = P_c\ \varphi(x')\ \varphi(x) + (1 - P_c)\ R_{II}(x',x)\ , \tag{3.5}$$

when $\varphi(x) = k(x)/\int k(x)dx$ is the absorption profile [i.e., $k(x) = k_o\sqrt{\pi}\ \varphi(x)$] and $P_c = \gamma_c/(\gamma+\gamma_c)$ is the measure of the probability of a collision between an excited state atom and a ground state atom during one natural lifetime. A collision is defined as that interaction between the two atoms which causes the excited state to lose memory of the absorbed frequency and hence emit via the entire Voigt profile. $R_{II}(x',x)$ describes the situation where, in the rest frame of the atom, the photon is re-emitted with the same frequency at which it was absorbed. Accounting for the Doppler effect by averaging over the motion of the atoms, one obtains an expression for $R_{II}(x',x)$ which is valid in a laboratory coordinate system.

In the discussion of the escape of resonance radiation as determined by $R(x',x)$, it is useful to introduce two frequency parameters, x_c and x_E, as in the following paragraphs.

For a sufficiently small value of a in the Voigt profile, there is a frequency x_c such that for $|x| < x_c - \delta_1$, the gaussian associated with the Doppler core completely dominates the absorption and for $|x| > x_c + \delta_2$ the lorentzian tail is the only important contribution. δ_1 and δ_2 are

surprisingly small so there is a sharp change over from "core" to "wing" contribution to the absorption profile. Let x_c be the frequency at which the Doppler term in the asymptotic form of the profile is equal to the wing term, i.e., $e^{-x_c^2} = a/\sqrt{\pi}\, x_c^2$. The function $R_{II}(x',x)$ then has the following important property. If the absorbed frequency $|x'|$ is less than x_c, then, to good approximation, the subsequent emission profile lacks the characteristic wings of the emission profile. Photons are emitted with almost equal probability for any $|x| < |x'|$, but the probability of emission at $|x| > |x'|$ drops off very sharply. A good approximation when $|x'|$ is sufficiently less than x_c is

$$R_{II}(x',x) = \frac{1}{2}\,\mathrm{erfc}\left(\max(|x|,\ |x'|)\right). \tag{3.6}$$

On the other hand, if $|x'| > x_c$ absorption occurs almost independently of the motion of the atom. The excited states will have approximately a maxwellian velocity distribution, and emission (which is coherent in the rest frame of the atom) will be distributed about the absorbed frequency with a near gaussian profile.

Now, define x_E by the condition

$$k(x_E)\, y_o/2 = 1$$

This can be evaluated via the asymptotic form of the Voigt profile using

$$\frac{k_o y_o}{2}\left(e^{-x_E^2} + \frac{a}{\sqrt{\pi}\, x_E^2}\right) = 1.$$

x_E is the frequency at which the optical depth to the center of the slab is unity. Photons with $|x| < x_E$ will tend to be absorbed, photons with $|x| > x_E$ will tend to escape. The relative values of x_E and x_c then are a useful guide to the frequency region of the profile (and the form of the redistribution function) which governs escape of the resonance photons. x_c and x_E are plotted versus pressure in Figure 8; values apply to the argon 1048 Å line with $y_o = 0.714$ cm and $\tau = 2.15 \times 10^{-9}$ sec.

If $x_E \leq x_c - 0.5$, then light emitted from the Doppler core can escape from the slab region $|y| < y_o/2$. Further, the pressure is less than 0.007 torr (see Figure 8) so that the probability of a decorrelating collision, P_c, is negligible. In this situation, one can then write

$$R(x',x) = R_{II}(x',x) = \frac{1}{2}\ \mathrm{erfc}\left(\max(|x|, |x'|)\right), \tag{3.7}$$

and Payne shows that the lower pressure assumption of complete redistribution made by Holstein, while not correct in principle, leads to the correct prediction for the escape rate of resonance photons.

For $x_E > x_c - 0.5$, escape from the slab is no longer dominated by the Doppler core of the profile. Further, as the pressure increases, the collision probability becomes appreciably different from zero. The redistribution function is then written by Payne in the form

$$R(x',x) = P_c\,\varphi(x')\,\varphi(x) + (1-P_c)\left[\frac{e^{-(x^2+x'^2)}}{\pi} + \left(\varphi(x') - \frac{e^{-x'^2}}{\sqrt{\pi}}\right)\delta(x-x')\right]. \tag{3.8}$$

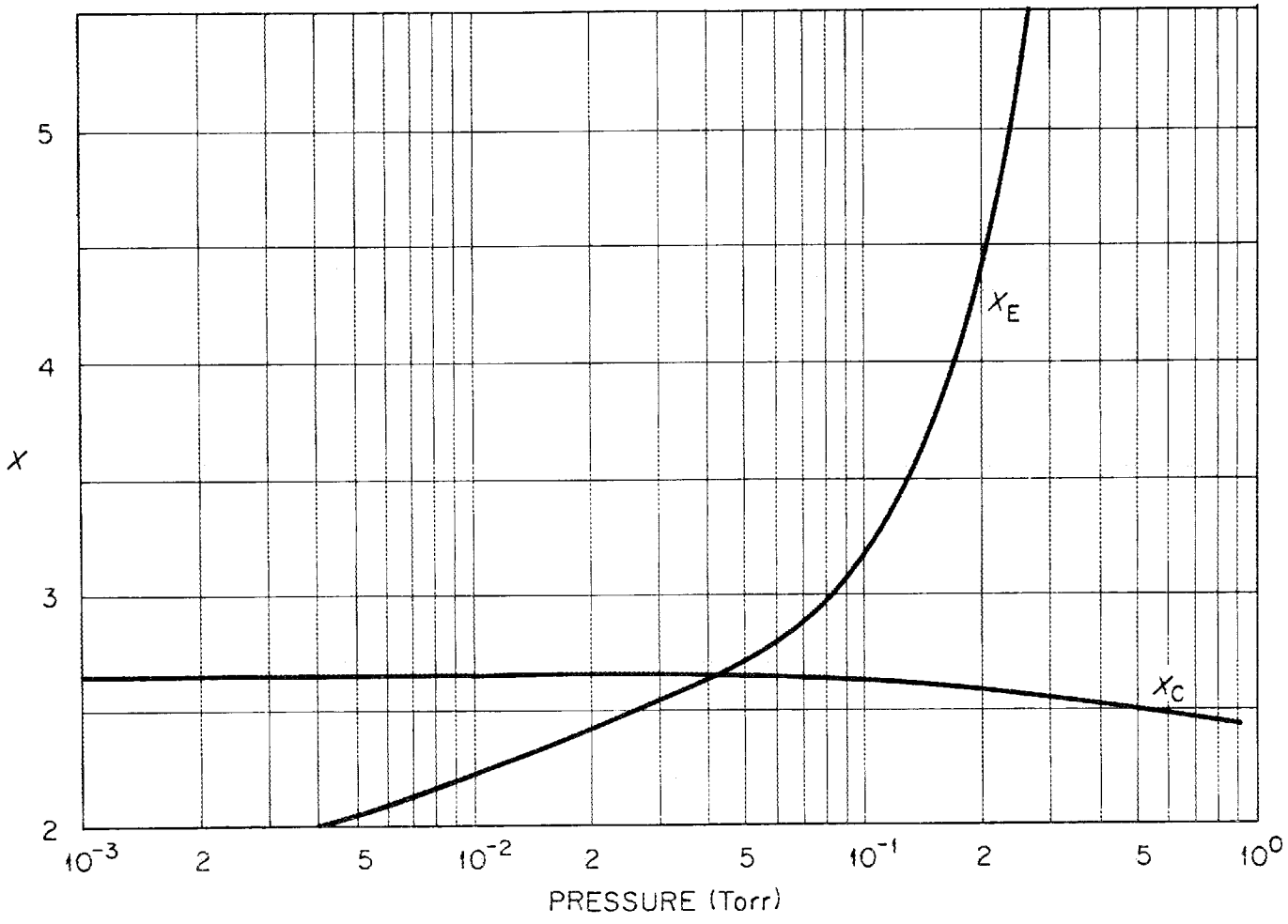

Figure 8. Reduced Frequency Parameters versus Pressure for the 1048 Å Resonance Line in the Geometry Used.

Note that $1-\pi^{-\frac{1}{2}}e^{-x'^2}/\varphi(x')$ rises sharply from near zero to unity near $|x'| = x_c$, and hence the second term, which is negligible for $|x'| < x_c$, dominates the expression in brackets for $|x'| > x_c$. To obtain good accuracy from this equation, two conditions should be met: $x_E > x_c + 3$ and $P_c > 0.3$. These are required so that the δ-function of the last term can be introduced. This δ-function assumes that a photon emitted on the far wings of the profile, even though it may undergo three or four absorptions and re-emissions before escaping or before a decorrelating collision sends it back to the core, does not "diffuse" much in frequency space. Both conditions are satisfied above 0.28 torr for the argon 1048 Å emission in the slab geometry.

At higher pressures, $P_c \approx 1$ and one obtains

$$R(x',x) \simeq \varphi(x')\varphi(x) \tag{3.9}$$

which is in accord with the complete redistribution treatment of Holstein where the pressure broadened profile governs the escape rate. Hence, in the low and high pressure limits, a theory based on the complete redistribution in frequency assumption should yield correct results for the transport process. However, at intermediate pressures, if the following conditions are not met, one expects deviations from the complete redistribution theory to occur.

1. $P_c < 0.7$; the probability of a decorrelating collision during the natural lifetime of the state should be small enough that an appreciable fraction of emissions can occur without such a collision.

2. $k_o y_o a \gtrsim 1$; the pressure should be sufficiently high that escape of resonance radiation based on the complete redistribution theory is governed by the presence of the wings on the emission profile. Recalling the definition of x_E, one can write this condition as

$$\int_{x_E}^{\infty} \left(\frac{e^{-x^2}}{\sqrt{\pi}} + \frac{a}{\pi x^2} \right) dx \gg \int_{x_E}^{\infty} \frac{e^{-x^2}}{\sqrt{\pi}}\, dx;$$

that is, x_E is large enough so that the number of photons which escape from the slab region if the wings are on the emission profile is larger than the number of photons escaping when the wings are absent. Neglecting the core term on the left of the inequality, condition 2 is obtained.

Applying these conditions to the 1048 Å line in argon with $y_o = 0.714$ cm, one obtains a pressure region 0.005 torr < P < 2 torr where the complete redistribution assumption should fail. This wide pressure region is a result of the short natural lifetime ($\sim 2 \times 10^{-9}$ sec) of the argon $^1P_1$ level. The much studied level in mercury which decays by emission at

2537 Å has an appreciably longer lifetime (1×10^{-7} sec), accounting for the lack of a similar pressure region.

Since Equation (3.8) is expected to give correct results at very low pressures ($x_E < x_c - 0.5$, so that only the first term in the brackets is important) and at pressures above 0.28 torr, it will be applied to the entire pressure range. In the intermediate pressure region, one expects to underestimate the escape rate (as will be discussed in the analysis of the data). After inserting Equation (3.8) into Equation (3.4), Payne uses several approximations in deriving an expression for $N(\vec{r},x,t)$, which becomes $N(y,x,t)$ in slab geometry. Photons whose emission is determined by the first two terms of Equation (3.8) (and hence emitted usually with $|x| < x_c$) are placed back at the center of the slab. This requires that there be strong imprisonment. Those photons emitted with $|x| > x_c$ are allowed to travel in space until they escape or are sent back to the core by a decorrelating collision. Photons at the core serve as a (relatively) slowly varying source function for wing photons; i.e., once a photon is emitted on the wings, it will not remain there for very many absorption and re-emissions, so that a "steady state" situation develops for "wing" excited states, and their time behavior follows closely the time behavior of the "core" excited states. Restricting $|x|$ to large values, one then obtains

$$N(y,x,t) = h(x)\,\delta(y)\,N(t) + \lambda \int_{-y_1}^{y_1} K(y,y',x)\,N(y',x,t)\,dy', \qquad (3.10)$$

where

$$h(x) = P_c\,\varphi(x) + \pi^{-\frac{1}{2}}(1 - P_c)e^{-x^2}$$

$$\lambda = (1 - P_c)\left(1 - \pi^{-\frac{1}{2}}\, e^{-x^2}/\varphi(x)\right)$$

$$K(y,y',x) = \frac{E_1\left(k(x)\,|y - y'|\right)}{2}\, k(x)$$

$$E_1(u) = \int_1^\infty \frac{e^{-tu}\,dt}{t}$$

$$N(t) = \int_{-y_o/2}^{y_o/2} dy \int_{-\infty}^{\infty} N(y,x,t)\,dx\,.$$

In the above, $N(t)$ is the total number of excited states in the slab region (which will emit mainly with $|x| < x_c$), and y_1 is an arbitrary value of $y \geq y_o/2$ which allows for the gas outside the slab region (i.e., $|y| > y_o/2$). Defining β by

$$\frac{dN(t)}{dt} = -\beta N(t)\,, \tag{3.11}$$

the following expression is derived by Payne (in the limit $y_1 \to \infty$):

$$\beta = \gamma \int_{-\infty}^{\infty} dx\, h(x)\left[\lambda + (1 - \lambda)\,E_2\,(\tau_o/2) + \frac{(1-\lambda)\lambda}{\pi} \int_{-\infty}^{\infty} \frac{[R(P)]^2}{1 - \lambda R(P)}\, \frac{\sin(P\tau_o/2)}{P}\, dP\right], \tag{3.12}$$

where

$$R(P) = \frac{\tan^{-1}(P)}{P}$$

and

$$\tau_o = k(x)\, y_o \, .$$

All theoretical values in this work (for pressures greater than 0.007 torr) were computed from Equation (3.12). Appendix 1 lists the computer code which was used. The program is fairly general and can be applied to other resonance lines, in other gases, and with different values of y_o.

3.3 Interpretation of the Experiment

As discussed in Section 2, a time-to-pulse-height converter together with a multichannel analyzer were used to determine the time distribution of photons escaping to the SEM detector. After many proton pulses, the number of counts stored in the j^{th} channel of the analyzer (corresponding to photons which escaped during the time $t_j - \Delta t/2 \leq t < t_j + \Delta t/2$ measured from the proton pulse, emitted into the appropriate solid angle, transmitted by the lithium fluoride window, reflected by the grating, and detected by the SEM) is given, quite generally, by

$$I(t_j)\Delta t = N_p \epsilon \Delta t \int dx \int_{V_F} dV \, \frac{d\Omega}{4\pi} \, \gamma \, N(\vec{r}, x, t_j)\, T(\vec{r}, x) \, , \qquad (3.13)$$

where

$\gamma N(\vec{r},x,t_j)dxdV$ = rate of time t_j at which photons with frequencies between x and x + dx are emitted from the volume element dV at $\vec{r}$.

$T(\vec{r},x)$ = transmission factor: the probability that a photon of frequency x will traverse the distance from dV to the window (measured in the direction toward the detector) without being absorbed.

$\Delta\Omega/4\pi$ = probability of this photon being emitted into the proper solid angle to reach the detector. Isotropic emission is assumed from each volume element. The SEM detector (1 cm high, 1 meter away) subtends a very small solid angle at any volume element dV in the cell. The entire detector (as seen through the monochromator exit slit) is visible to each dV in V_F, enabling one to use the same solid angle for each.

N_p = a number proportional to the number of excited atoms produced per cm of track length during a given experiment.

ϵ = combination of transmission efficiency of window, reflection efficiency of grating, and detection efficiency of the SEM detector, evaluated at the line center.

V_F = the volume of the reaction cell "visible" to the SEM detector. The spatial integral in Eq. (3.13) is always carried out over V_F; the frequency integration is performed over the entire profile of the

1048 Å line. The volume of the reaction cell V_F viewed by the SEM detector is determined in the horizontal plane by the monochromator entrance slit width z_o and in the vertical plane by the diameter y_o of the cylindrical aperture to the reaction cell (see Figure 9a).

The fairly small value of y_o (0.714 cm) compared to the reaction cell diameter ($2R = 2.22$ cm) is important at early times (measured from the proton pulse) for several reasons: 1) With $y_o/2R \ll 1$, the escape of resonance photons from V_F is determined almost entirely by those photons which escape across the boundary of a region between two infinite parallel planes separated by the distance y_o. 2) Escape from this "slab" region is consistent with the assumptions used in the analysis to obtain Equations (3.10) and (3.12). We now consider these points in more detail.

For a limited time after the proton pulse has traveled through the cylinder, a dominant fraction of the $^1P_1$ states is confined to a small region near the axis. Most of the photons are emitted with a frequency near the core of the resonance line and in the strong trapping limit ($k_o y_o/2 > 50$) are absorbed and re-emitted many times before traversing a distance comparable with $y_o/2$. Photons which escape from V_F generally, then, have been emitted from near the axis with frequency such that $|x| > x_E$. Escape from V_F in the z direction (see Figure 9b) is not important due to the cylindrical symmetry of $N(\vec{r}, x, t)$ about the proton beam. Further, there is a much larger probability for photons to escape across the sides of V_F

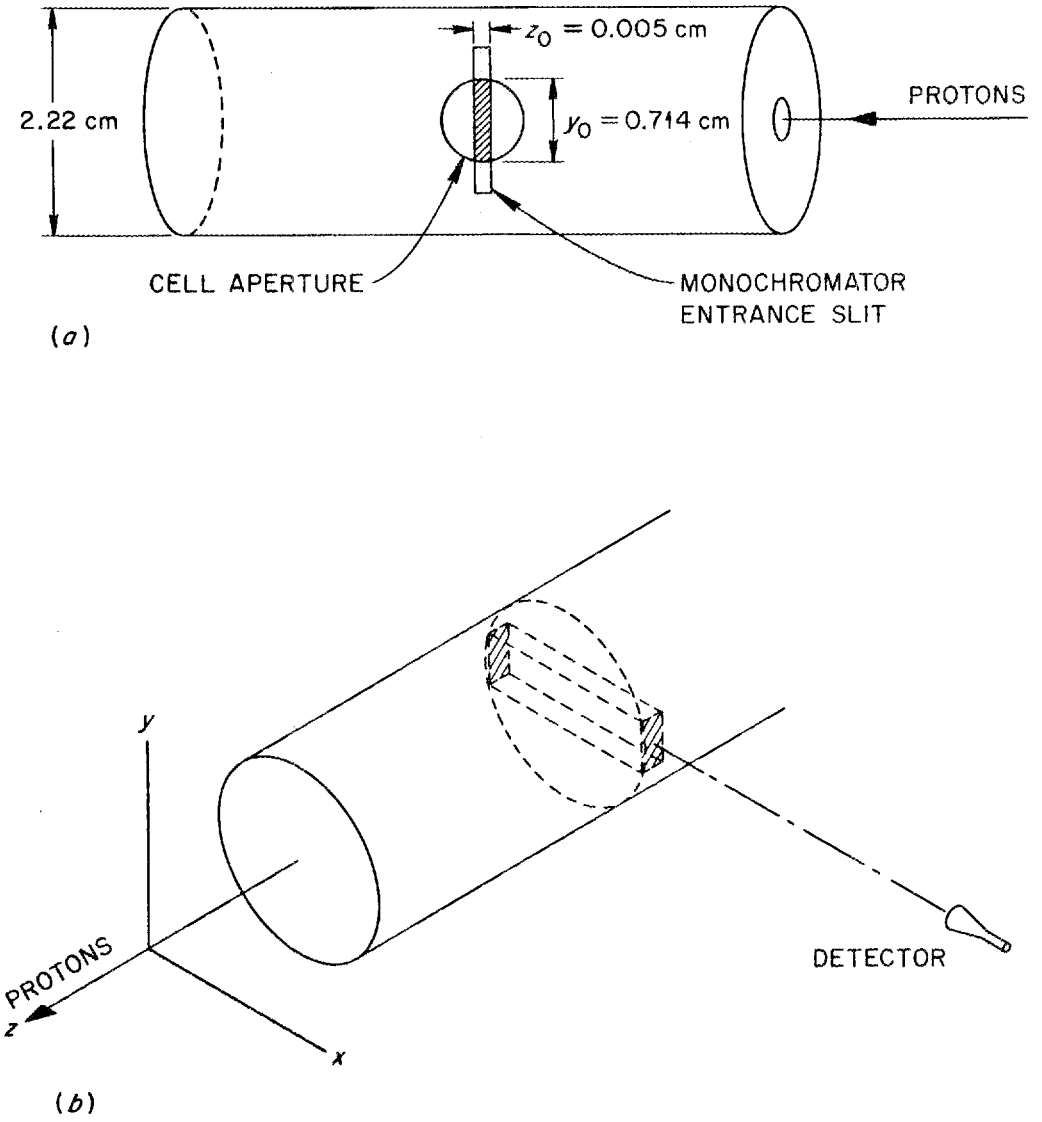

Figure 9. The Reaction Cell as Viewed by the Photon Detector. (a) Shaded area is in view at SEM detector. (b) Cross section of slab used in early time analysis.

parallel to the xz plane than through the ends (partially indicated by shaded area in Figure 9b). For purposes of calculating the number of excited atoms that can be seen, the volume of V_F can thus be extended to infinity in the positive and negative x and z directions with very little error introduced in evaluating Equation (3.13). This error is estimated to be about 2% in the high and low pressure limits.

In deriving Equations (3.10) and (3.12), photons emitted at frequencies less than x_c are treated as if they were emitted and reabsorbed at $y = 0$. In the analysis, it is assumed that the fraction of the number of excited states which will emit photons with $|x| > x_c$ is small compared to the fraction which will emit at $|x| < x_c$. Escape from the slab can occur only for those photons with $|x| > |x_c|$. Photons which are absorbed with $|x'| > x_c$ are allowed to move from $y = 0$, and, as there is (depending on the pressure) an appreciable probability of being re-emitted with $|x| > x_c$, the analysis treats escape by correlated jumps in a realistic way. However, if after absorption at $|x'| > x_c$ the excited atom undergoes a decorrelating collision so that emission will most probably occur with $|x| < x_c$, this latter emission will be treated as if it occurred at $y = 0$. Hence, a subsequent emission at $|x| > x_c$ will be assigned an improper spatial location. This error is minimized if one considers only short enough times after the proton pulse that non-successive emissions at $|x| > x_c$ are improbable (early times).

Thus, $N(y,x,t)$ from Equation (3.10) with time dependence described by Equation (3.12) can be used to approximate $N(\vec{r},x,t)$ in Equation (3.13). Within the early time restriction, this substitution into Equation (3.13) should give accurate values for the time dependence of $I(t)\Delta t$. To evaluate the actual magnitude of $I(t)\Delta t$, one needs to redefine the transmission factor $T(\vec{r},x)$ in terms of a function $T_1(R,x)$ which allows for escape to the window from the axis by successive emissions with $|x| > x_c$. The accuracy of the time dependence obtained under these conditions will be discussed further in the analysis of the data.

At early times, then, most of the light emitted from the cell comes from near the cylinder axis, and one can consider the transport problem in terms of resonance photons escaping from a slab geometry. At late times, however, the population of each volume element of the cylinder is such that the spatial profile remains constant (at least in the high and low pressure limits where a complete redistribution in frequency theory is appropriate); each volume element dV emits with the same frequency profile; the total number of excited states in each dV is decreasing nearly exponentially. In general, the early time and late time escape rates will differ measurably. However, the ratio of $-d(\ell n\, I)/dt$ at early and late times, with $I(t)$ defined by Equation (3.13), is dependent on the parameter $y_o/2R$ and one can, in principle, choose this parameter so that at one pressure the ratio is unity.

To obtain an estimate of the appropriate value of $y_o/2R$, consider the low pressure limits. We have shown that the assumption of complete redistribution in frequency gives nearly correct results. Only Doppler broadening is important, and the early time value of $-d(\ell n I)/dt$ can be equated to β_E given by

$$\beta_E = (2\gamma/\sqrt{\pi}) \int_o^\infty e^{-x^2} E_2(k_o y_o e^{-x^2}/2) dx . \tag{3.14}$$

The late time decay rate β_L is determined by the fundamental mode of the eigenfunction expansion developed by Holstein.[2,3] We use the cylindrical geometry results of Payne and Cook[21] and find at 0.004 torr,

$$\frac{\beta_E}{\beta_L} \approx \frac{\gamma/\pi^{\frac{1}{2}} x_E k_o y_o}{1.575\gamma/k_o R\sqrt{\pi \ell n(k_o R)}} = 0.34(2R/y_o) . \tag{3.15}$$

(low pressure)

In this experiment $y_o/2R = 0.322$, so the early time escape rate should be only about 5% faster than the late time rate. One expects by interpolation that the escape rate at intermediate times will join these two smoothly, and one should be able over an extended period of time to examine the escaping photons as an exponential decay with a single effective decay constant.

At pressures above 2 torr, Doppler broadening plays no part in the transport process, and one calculates the ratio of early to late time escape rates β_E/β_L, using only the wing term of the profile. At higher pressures, with β_E given by

$$\beta_E = 2\gamma \int_{x_o}^{\infty} (a/\pi x^2) E_2(k_o y_o \, a/2\sqrt{\pi}\, x^2) dx , \tag{3.16}$$

$$\frac{\beta_E}{\beta_L} \approx \frac{(2\gamma/3)\sqrt{2a/\pi^{\frac{1}{2}} k_o y_o}}{1.125\, \gamma/\sqrt{\pi k_P R}} = 0.624\sqrt{2R/y_o} = 1.1 , \tag{3.17}$$

(high pressure)

where $x_o = x_c + 3$ and $k_P = (\gamma \lambda_o^2 N g_2/g_1)/(2\pi\gamma_c)$. Thus, at high pressures the ratio is again near unity with the early time escape rate approximately 10% faster than the late time rate. This effect is observable experimentally (see Figure 5) at 5.25 torr, where $\beta_E = 0.358 \times 10^6$ sec^{-1} and $\beta_L = 0.32 \times 10^6$ sec^{-1}. (The late time escape rate is only measurably distinct from the early time rate above 0.5 torr. Extracting the late time slope from the data, it is found to be constant over the pressure range 0.58 to 5.25 torr.) One expects that β_E/β_L may not be greatly different from these limiting cases in the intermediate pressure region.

We now examine the computation of $I(t)\Delta t$. Above 0.007 torr, as discussed in Section 3.2, Equations (3.10) and (3.12) are used; below this pressure, an equation for β derived by Payne,[6] using the redistribution

function in Equation (3.7), is used. In either situation, after a few natural lifetimes from the proton pulse, the early time escape can be described by writing

$$N(\vec{r},x,t) = e^{-\beta t} f(\vec{r},x). \tag{3.18}$$

As discussed previously, $N(\vec{r},x,t)$ can be written in this way only for $|x| < x_c$ (a similar restriction holds for the low pressures: $P < 0.007$ torr); the assumption has been made that one can neglect the spatial spread of excited states for photons of these frequencies. Thus, Equation (3.13) becomes

$$\begin{aligned} I(t_j)\Delta t &= N_p \epsilon \Delta t \frac{\Delta\Omega}{4\pi} \gamma e^{-\beta t_j} \int_{-\infty}^{\infty} dx \int_{V_F} dV\, f(\vec{r},x)\, T_1(R,x) \\ &= C(P,y_o,R)\, e^{-\beta t_j} \Delta t . \end{aligned} \tag{3.19}$$

The evaluation of $C(P,y_o,R)$ and hence the computation of the time-integrated count (intensity) has not yet been carried out due to the theoretical difficulties of estimating the values at intermediate times. The theory has to account for the nonlinear rise in the observed intensity as a function of pressure as given by Equation (3.1). The energy lost by the protons in traversing the cell (as determined by stopping power data) is very nearly linear up to 40 torr, and there is no reason at present to believe that excitation of the $^1P_1$ state becomes more preferable as the pressure is increased. The additional increase in intensity over a linear increase is

believed to be due to a geometrical factor, inherent in the mode of observation. At the surface of the gas, photons are not emitted isotropically, but the directional distribution depends on the distribution of excited states in the gas. At lower pressures, where Doppler broadening is important, the spatial spreading of excited states before an appreciable number of photons escape to the walls is greater than at higher pressures, where pressure broadening dominates the transport process. That is, at higher pressures most of the escaping light comes from near the cylinder axis, whereas at lower pressures the light "source" is more diffuse. Then, from solid angle considerations, a larger fraction of the radiation will reach the detector at higher pressures. This effect should saturate when pressure broadening makes the only important contribution to the transport of resonance radiation. The high pressure data of Section 4 indicate that this may occur around 30 torr.

Typical data curves, plotting $I(t)\Delta t$ versus time on a logarithmic scale, are shown in Figure 5. To compare the data with the theoretical calculations, the early time slope was determined by a least squares fit as discussed earlier, giving additional weight to the counts in earlier time channels. Experimental and theoretical values of β are given in Table 1 and in Figure 6. The natural lifetime $\tau = 1/\gamma$ of the $^1P_1$ argon state is somewhat uncertain. Two reasonable values are 2.15×10^{-9} sec[41] and 1.8×10^{-9} sec.[40] Curves representing both values are shown in Figure 6.

A measurably different slope was observed at late times at pressures above 0.5 torr. This slope is found to have a constant value of 0.32×10^{6} sec^{-1}. Using the expression for β_L implied from Equation (3.17) (for the late time escape rate from cylindrical geometry[21]), this value is in good agreement with the 1.8×10^{-9} sec natural lifetime. In addition, the results obtained by applying the Holstein-Biberman equation at early times with the complete redistribution assumption is shown. [This is obtained from Equation (3.12) with P_c set equal to unity.] The errors on the slope measurements are estimated to be less than $\pm$ 3% except for the data point at 0.0015 torr which is $\pm$ 20%.

The data points marked with an o in Figure 6 and indicated by an small a in Table 1 were taken at a later time and under different vacuum pumping conditions than the rest of the data. In this later set of experiments, an impurity was present which would tend to increase the observed escape rate of the resonance photons from the container. These later data fall on a smooth curve which below 0.3 torr lie approximately 0.03 μsec^{-1} above the data determined in the earlier experiments where the impurity was not present. At pressures above 0.3 torr, the earlier and later experimental points are the same within experimental error, suggesting that in the process of flowing the argon gas, viscous flow is sweeping out this impurity. At lower pressures, Knudsen flow would not appreciably effect the partial pressure of the impurity.

As discussed earlier, one should expect good agreement between the calculated values and the experimental values in two situations:

1. $x_E < x_c - 0.5$

2. $x_E > x_c + 3$ and $P_c > 0.3$.

Condition 1 is satisfied below 0.007 torr. Wings on the absorption profile are not important at these pressures as most of the light is escaping with frequency in the Doppler core; the probability of a collision is very small so that photons are also never emitted on the wings. Only one data point has been obtained in this region due to experimental limitations on photon intensity and SEM background count. The early time escape rate of 5.4×10^6 sec^{-1}, accurate to $\pm$ 20%, is in agreement with both the Payne and Holstein calculations (see Figure 6). Note that the strong trapping requirement is only marginally satisfied at 0.0015 torr where $k_o y_o/2 = 18$.

In the high pressure region above 2 torr, the probability of a collision, P_c, during an excited state lifetime is greater than 0.7. There is no correlation between absorbed and re-emitted frequencies; the emission and absorption profiles are the same and are determined from pressure broadening theory; photons are escaping only from far on the wings of the profile. Theoretically, the escape rate becomes constant, independent of pressure (the absorption coefficient is proportional to pressure, but the additional trapping which occurs is just cancelled by the increase in collision

rate γ_c, which is also proportional to pressure). One expects the agreement between experiment and theory to be quite good in this pressure region; however, the data is 10% higher than theory using $\tau = 1.8 \times 10^{-9}$ sec and 20% higher using $\tau = 2.15 \times 10^{-9}$ sec (see Figure 6). Some possible contributions to this difference are discussed in Section 3.4. Note that in the 10 torr region other processes are beginning to be observed which compete with resonance radiation for the energy deposited by the proton beam; these are examined in Section 4.

In the intermediate pressure region (0.007 torr < P < 2 torr) neither simplifying assumption about the collision probability is appropriate. Starting at 0.007 torr, as the pressure is increased, $k(x)y_o/2$ increases and the photons must be emitted out farther from the core to have the same probability of escape. When $x_E \geq x_c$, most photons emitted in the core, $|x| < x_c$, are retrapped and "redistributed." Absorption on the wings of the Voigt profile prevents escape; however, in the absence of a collision, there is no corresponding emission on the wings. Thus, a longer containment time is obtained than that which is computed based on a complete redistribution in frequency assumption. In this pressure region, photons with $|x| < x_c$ will be emitted and absorbed many times and not travel appreciably in space. Eventually a rare collision occurs which enables emission with the entire Voigt profile to occur (then escape of a photon emitted with $|x| > x_c$ will be

more rapid than that from the complete redistribution theory, as there may not be another collision to send the photon back to the core).

Referring to Figure 6, the theory based on complete redistribution in frequency predicts more than a factor of 3 faster decay than the observed rate around 0.04 torr. The theory discussed in Section 3.2 predicts a slower decay at the pressure of about 30% to 50% (depending on the choice of the natural lifetime). In Section 3.4 it is argued that almost all differences between the theory and experiment should be in the direction of a faster observed escape rate. Hence, it is believed that this latter theory presents a fairly accurate picture of the escape of resonance radiation from 0.0015 to 10 torr.

3.4 Theoretical and Experimental Differences

Several experimental and theoretical factors can cause difference between calculated and observed escape rates. In general, all these factors tend to produce effects which cause the measured escape rate to be faster than that determined from the theory. Some of these effects (i.e., ones such as 5 and 6 which can be reduced by considering sufficiently early times after the proton pulse), however, are not as critical as they could be, due to the selected value of $y_o/2R$ which tends to extend in time the early time slope.

1. The initial source function is not confined rigorously to the cylinder axis as the diameter of the proton beam is about 0.3cm.

In addition, delta rays produced in the proton-argon collisions may cause further spreading. Delayed recombination of ionized argon atoms (during ambipolar diffusion) could possibly serve as a source function of $^1P_1$ excited atoms spread out in time and space, but experimental data taken indicate that this is an unimportant effect below 10 torr.

2. The initial $^1P_1$ excited states produced by the proton beam, either directly or by cascade, will have wings on the first emission even at lower pressures. The emission spectrum will not be quite a Voigt profile due to the impulse given the argon atoms by the protons. Those photons emitted on the far wings in this first emission should escape without further trapping. However, no large initial burst of photons is observed in the first few lifetimes (channel 1 of the analyzer), suggesting that if these photons are indeed escaping, the direction of observation in this experiment precludes detecting them, i.e., relatively few photons are initially emitted perpendicular to the proton beam. The analysis at low pressures[6] shows that small deviations initially present in the Doppler core of the profile will not be retained for more than a few natural lifetimes. The emission profile quickly approaches a guassian (falling off a

bit more quickly than a gaussian on the wings where the effects of finite boundaries become important).

3. The value given for y_o is obtained by measuring the aperture diameter of the reaction cell. Several factors may give a smaller effective y_o: a) the intrinsic lack of focus in the vertical plane of the Seya-Namioka geometry, b) the possibility of a slight misalignment of the SEM detector with respect to the exit slit, c) heating of the lithium fluoride window preferentially near its edge resulting in a decreasing transmission coefficient from the center out to the edge. With a smaller y_o, the measured escape rate at early times would appear faster.

4. At the low pressures, errors will be introduced due to the assumption of isotropic emission in deriving Equation (3.4).

5. In the slab geometry treatment, those photons emitted with $|x| < x_c$ are not allowed to contribute to the transport process, but are immediately reabsorbed at $y = 0$. Only those photons with $|x| > x_c$ can escape from the slab. Thus, one obtains an underestimate of escape rate from the slab at late enough times where spreading due to $|x| < x_c$ photons is on the order of $y_o/2$.

6. Putting the excited states back at the center has another effect. There is a tendency for quanta which have moved a bit toward the

window to escape faster due to the smaller distance in the transmission factor. This should be compensated for to first order by those photons escaping to the window more slowly from the opposite side. At lower pressures, where Doppler broadening dominates the transport process, estimates based on the work by Payne and Cook[21] indicate this cancellation is good to 10% for $t < 0.1\ (k_o R/\gamma)[\pi \ell n(k_o R)]^{\frac{1}{2}}$. In the pressure broadening region, this cancellation is even better. With the relatively small value of $y_o/2R$ used in this experiment, this effect is small compared to that induced by escape across the slab boundary.

7. An appreciable error at intermediate pressures arises when the conditions associated with the use of Equation (3.8) are not met. In particular, at pressures less than 0.3 torr, "diffusion in frequency space" can occur for photons emitted on the wing. This tendency of photons emitted and absorbed many successive times on the wings violates the strict coherence required by the δ-function in Equation (3.8). Due to the greater number of photons emitted with frequency near the core, this "diffusion" will carry the average photon frequency farther from the core with each successive emission, hence increasing the actual escape rate. At pressures below 0.01 torr, this effect is not important because the wings are not required for escape.

8. The extension of the gas volume to infinity in evaluating Equation (3.12) will introduce a small error, again causing one to underestimate the rate of escape.

SECTION 4

THE HIGH PRESSURE EXPERIMENT

4.1 Introduction

In this section the results of measurements made on argon in the pressure region 1 to 600 torr are presented. Figure 10 shows some sample scans of photon intensity versus wavelength. With the lithium fluoride window in place, the several argon emission lines below 1040 Å are not transmitted to the SEM detector. The main feature of these scans, at the lower pressures, is the resonance emission peaks at 1048 Å and 1067 Å. At higher pressures the spectrum is dominated by a continuum of light centered at 1275 Å (1250 Å continuum). In addition, a continuum (1100 Å continuum) seems to come off the 1067 Å line whose peak has nearly dissappeared. The 1048 Å peak shifts toward longer wavelength and at higher pressures its intensity decreases. These features are the same as those observed in other fast charged particle excitation experiments.[10,16,17]

Figure 11 shows an energy level diagram for the argon atom, indicating the excited states referred to in this work. The argon atom ground state configuration is $1s^2 2s^2 2p^6 3s^2 3p^6$ ($^1S_0$). The four lowest excited states result from a coupling between one excited electron and the five

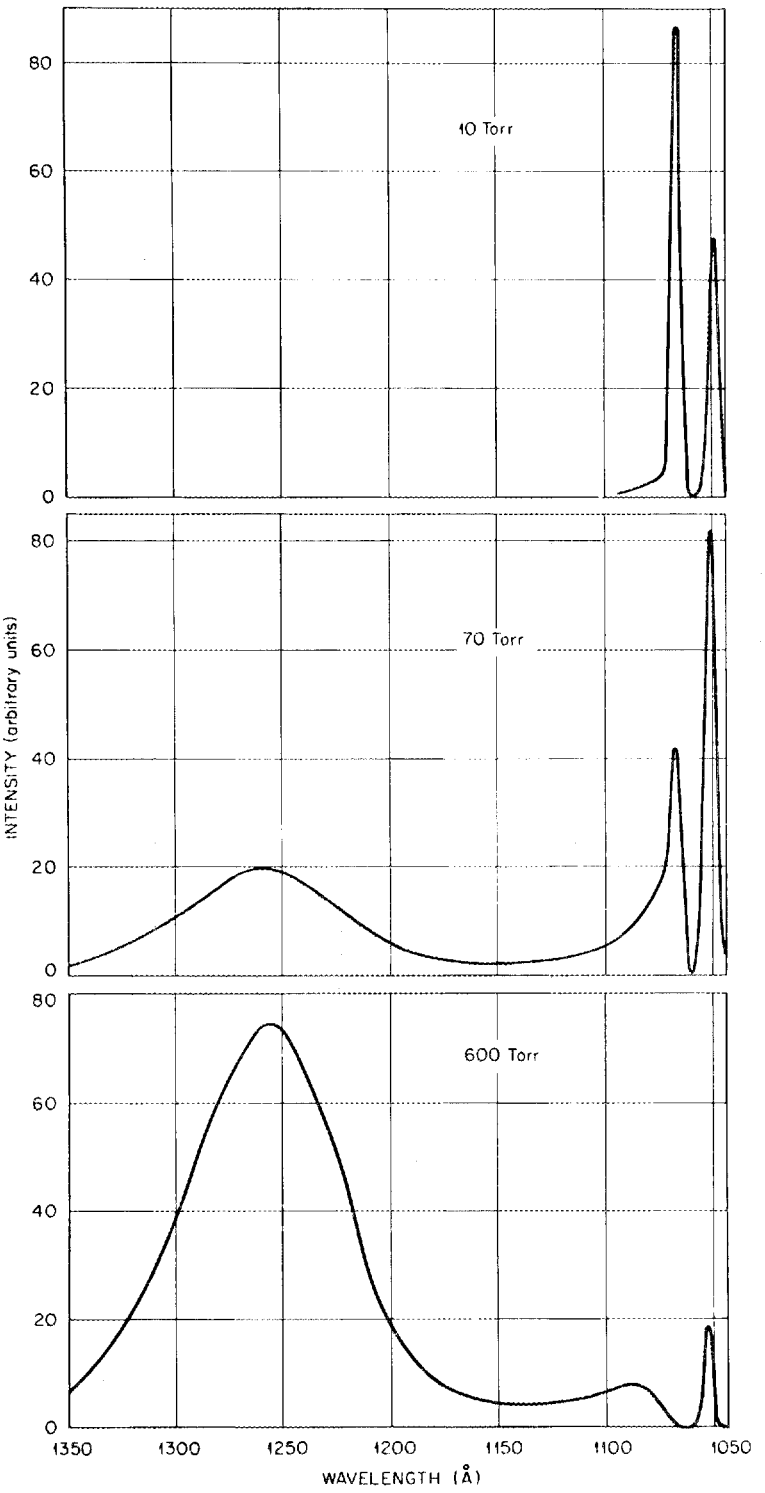

Figure 10. Argon Spectra at Several Pressures.

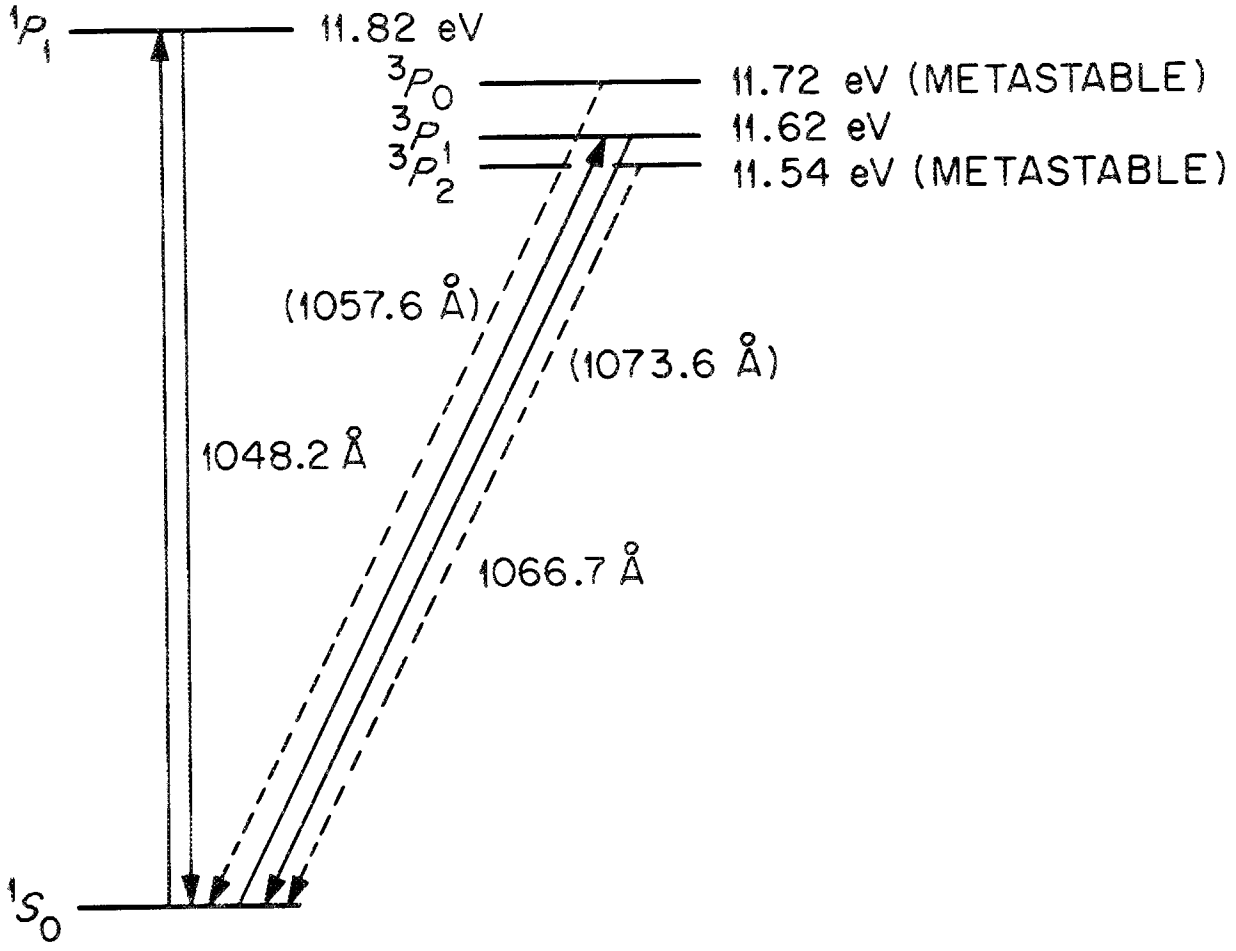

Figure 11. Energy Level Diagram of the Ground State and First Excited States of the Argon Atom.

remaining electrons in a $3p^5 4s^1$ configuration and are designated by $^1P_1$, $^3P_{0,1,2}$. (Russell-Saunders coupling is used which is only approximately valid here.)

As a burst of relatively fast protons (initially at 1.8 MeV) passes through the argon gas, it interacts with the atoms in many ways. Excited levels which are coupled to the ground state with large oscillator strengths will be excited directly (optical approximation); many atoms are ionized; the secondary electrons may then excite other low-lying levels (we expect, however, that excitation by secondary electrons is much less important here than with discharge techniques); cascading from higher levels provides a rapid relaxation to lower excited states such as the $^1P_1$ and $^3P_{0,1,2}$. Recombination of electron-ion pairs followed by cascading will provide an additional contribution to the low-lying states. Collisions between an excited atom and a ground state atom or atoms may enable metastable states to radiate or cause the formation of excited argon molecules. With the proton beam intensities used in this experiment, the interaction between the various excited states can be ignored (e.g., stimulated emission).

A model has been developed by Hurst and Thonnard[10,11,16] which accounts for the main features of the observed spectrum over this wavelength region of the vacuum ultraviolet (vuv). In this model, the 1250 Å continuum is produced by a dissociation transition by a radiating argon

molecule (Ar_2^{Rad}). A large portion of the energy for this molecule is supplied by the $^1P_1$ excited atom (its effective lifetime extended several orders of magnitude by resonance trapping) which undergoes a three-body collision with two ground state argon atoms to form a metastable molecule (Ar_2^{Met}), which then interacts with another ground state atom to convert (Ar_2^{Met}) to (Ar_2^{Rad}). It is also suggested that the $^3P_2$ metastable atomic state is converted by three-body collisions to a radiating molecule which serves as an additional source for the continuum. The 1100 Å continuum has as its precursor the $^3P_1$ (or possibly the $^3P_2$) state which radiates while undergoing a two-body collision. This model will be examined in Section 4.5.

Figure 12 shows typical time-dependent intensity curves for the 1048 Å emission in the high pressure region. These decay curves exhibit two components whose time behavior and dependence on pressure are quite different. There is an early fast component followed by a second component which is 15 to 30 times slower. This is in contrast to the low pressure data where the decay is similar to the fast component alone. At 150 torr and above, this slow component represents an appreciable fraction of the total light emitted near 1048 Å. It usually appears to have a plateau before decreasing in an exponential way (at very late times, the data fall off more slowly than exponential). Below 150 torr, this plateau is not usually resolved. It is assumed that the two components are produced by separate methods of populating the $^1P_1$ excited state. The fast component represents

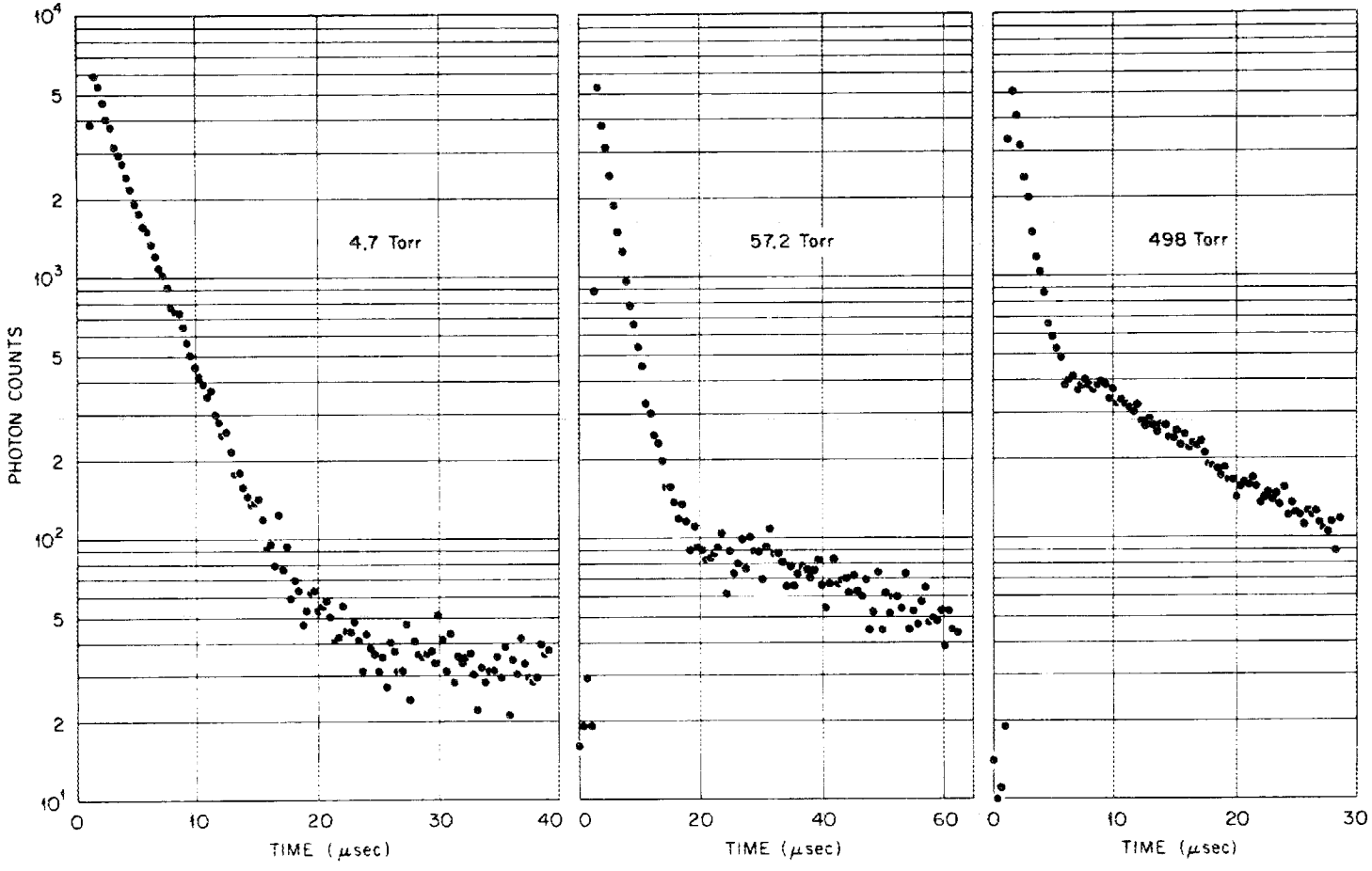

Figure 12. Decay Curves for Argon 1048 Å Resonance Radiation at Several High Pressures.

the escape of resonance radiation after direct population of the $^1P_1$ state by the proton beam, secondary electrons, and by cascade. The slow component indicates a delayed populating of the $^1P_1$ level, most probably by recombination of argon ions with electrons.

In this work, the two components will thus be treated as independent; the second component is subtracted from those channels it shares with the first. Without a specific model for the slow component, there is some uncertainty in extrapolating for its time behavior at early times. The plateau at higher pressures suggests a process which builds up for a few microseconds before decaying. However, for the experiments at and above 150 torr, the plateau (slightly reduced to account for residual of fast component) will be extended back to zero time for purposes of separating the two components. At 85 torr and below, the second component decays more slowly and is relatively insignificant so that negligible error is introduced by using a two-exponential fit directly to the data. The fast component decay rates are consistent with the trend of the low pressure data of Section 3 and will now be considered in detail.

4.2 The Fast Component Decay Rates

After removing the slow component by the methods discussed in the previous section, the fast component time dependence can be examined. The decay is not, in general, exponential; the very early time decay rate is somewhat faster than the average rate. Figure 13 and Table 2 give values

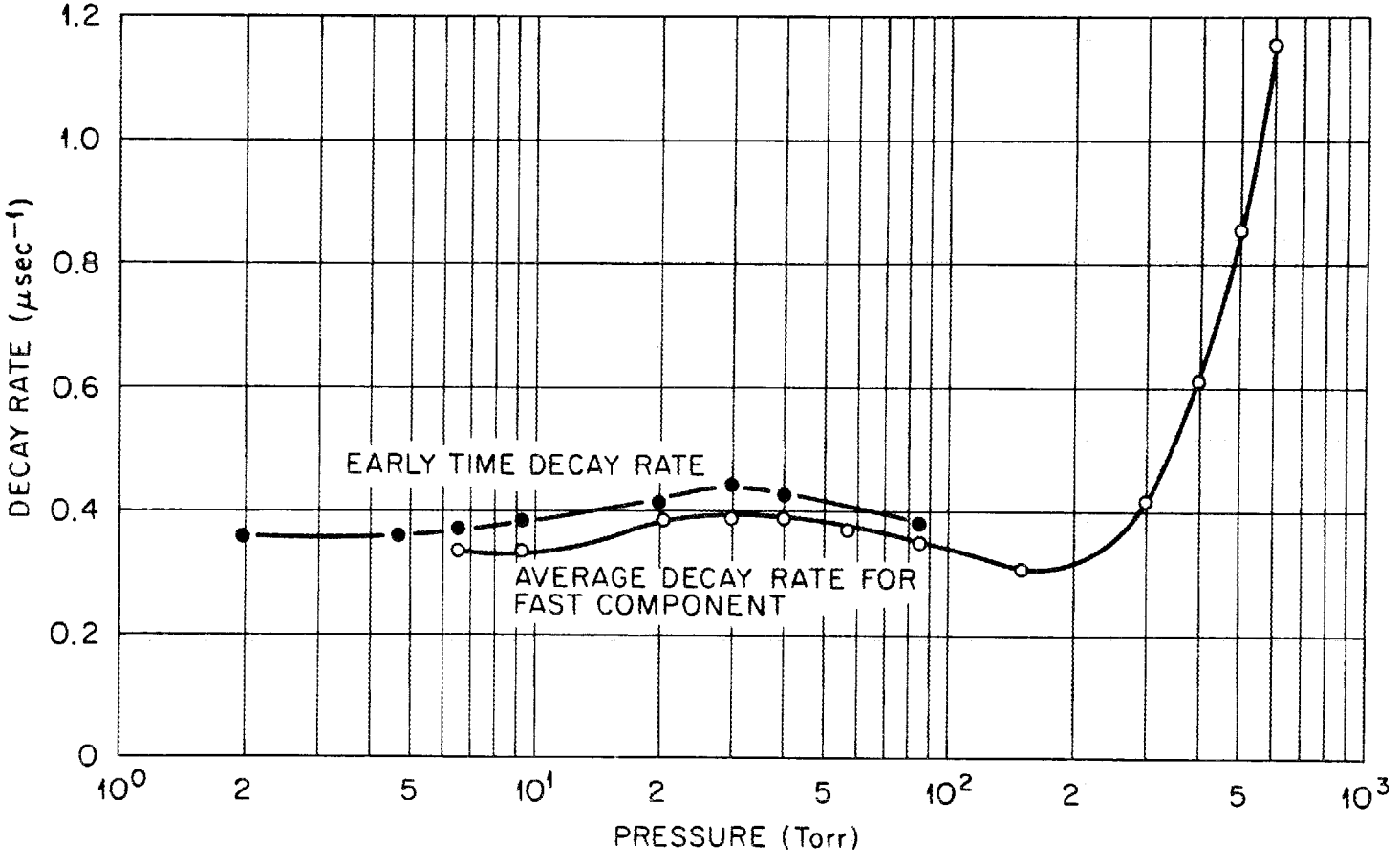

Figure 13. Escape Rate versus Pressure for Argon 1048 Å Resonance Radiation at High Pressures.

TABLE 2

EXPERIMENTAL FAST COMPONENT ESCAPE RATES FOR THE ARGON ($^1P_1$) RESONANCE EMISSION AT HIGH PRESSURES

Run No.	Pressure (torr)	Very Early Rate (μsec^{-1})	Average Rate (μsec^{-1})
176	1.94	0.361	-----
122	4.70	0.357	-----
104	6.25	0.368	0.335
103	9.35	0.382	0.334
99	20.4	0.415	0.384
98	29.7	0.442	0.389
97	40.0	0.427	0.390
96	57.2	0.403	0.372
95	84.9	0.378	0.350
94	147	-----	0.303
93	147	-----	0.306
105	152	-----	0.305
92	297	-----	0.418
91	297	-----	0.418
90	396	-----	0.607
89	498	-----	0.856
88	600	-----	1.15

for exponential fits to both. The very early decay rate joins smoothly with the values obtained for the fast component in Section 3. The "late time" slopes of Section 3 were not extracted here due to the uncertainty in the removal of the second component. It is felt that the average decay rate is more useful. The accuracy of each slope was determined individually and depends, at higher pressures, on the success of accurately removing the slow component. Error bars on the data in Figure 14 give my estimate on accuracy after the second component has been removed (by subtracting a constant amount). However, additional uncertainty is also present due to the possibility of a different time behavior at early times for this second component. For example, for an experiment at 147 torr, different extrapolation procedures were performed (see Figure 15). The resulting decay rate of the fast component is shown in Table 3.

An interesting effect is observed in the measured escape rates, both early and average, below 150 torr. This rate increases to a maximum around 30 or 40 torr, then drops off to a minimum near 150 torr. Furthermore, the average decay rate at 150 torr is the same as the "late time" rate found in the low pressure experiments of Section 3. This same effect was observed by Thonnard[10,11] (down to 25 torr), using a pulsed 250 keV electron beam to excite the argon atoms. At present, the cause of this effect is not known.

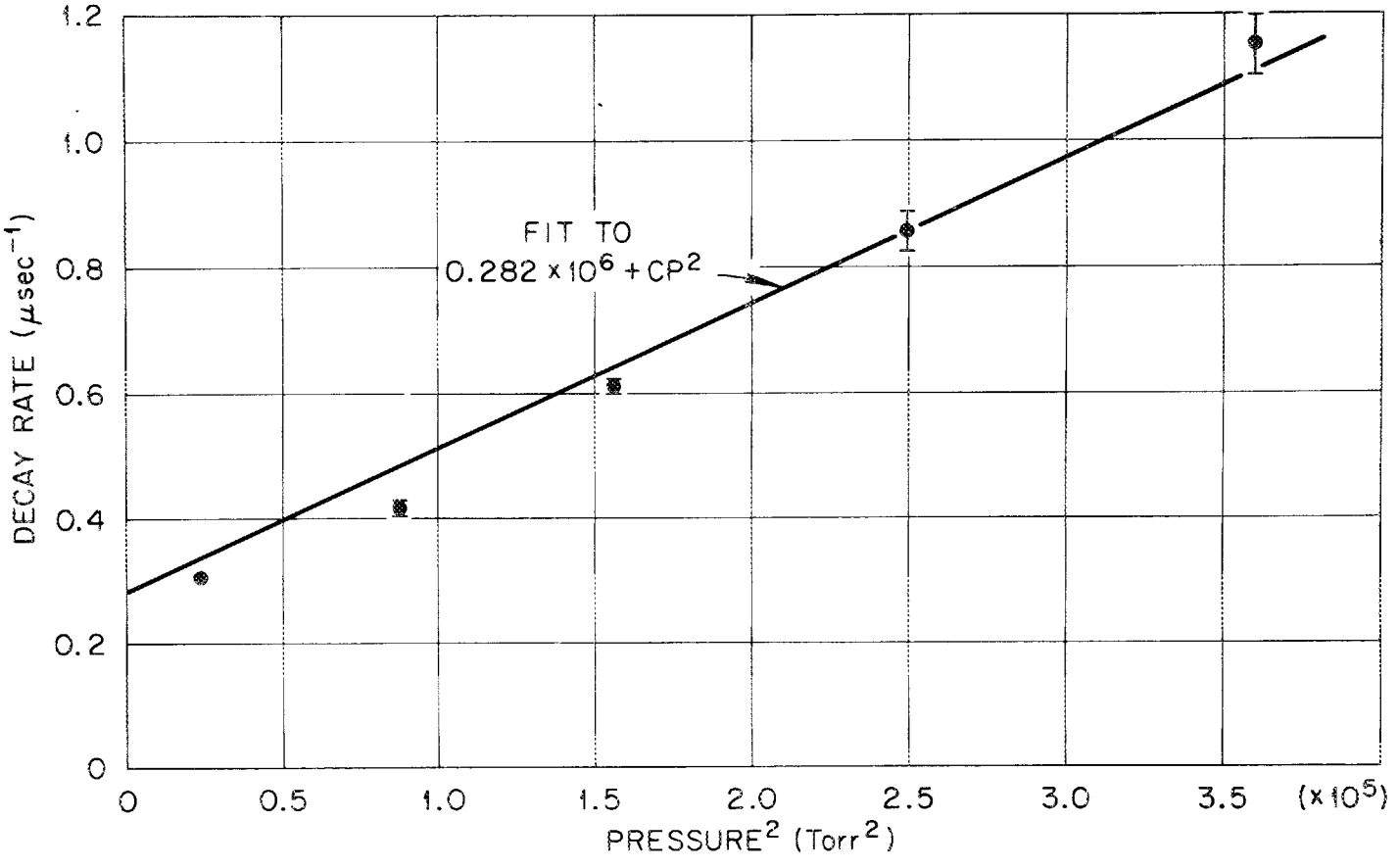

Figure 14. Average Escape Rate for Fast Component versus Pressure Squared.

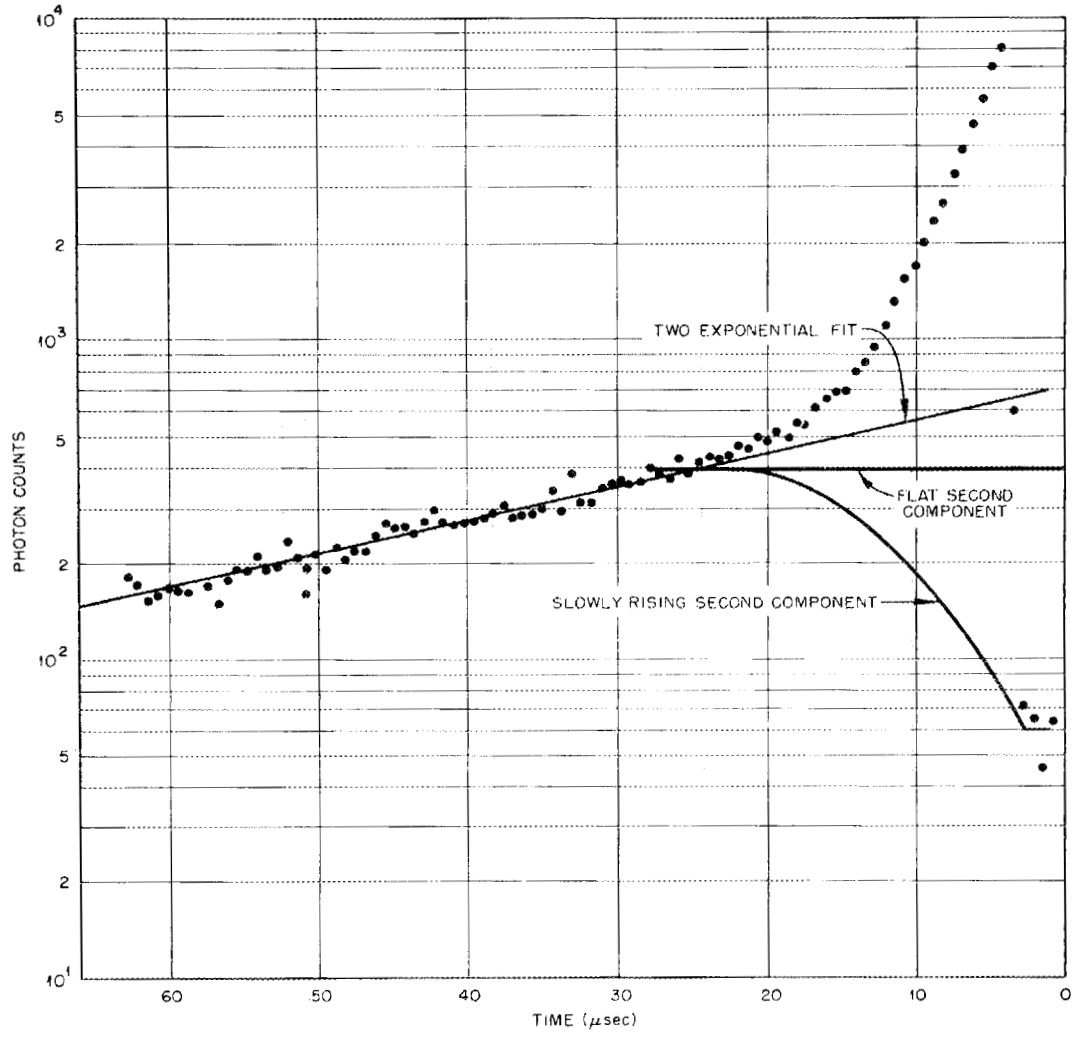

Figure 15. Various Extrapolations of Second Component to Early Times. Pressure = 147 torr; time evolves toward the left.

TABLE 3

POSSIBLE FIRST COMPONENT ESCAPE RATES AT 147 TORR

(Run No. 94)

Method of Extrapolation at Early Times	Escape Rate (μsec^{-1})
Two exponential fit	0.324
Flat second component	0.303
Slowly rising second component	0.280

Above 150 torr, the escape rate increases as the square of the pressures (Figure 14). It is instructive to compare the results of this experiment (radius of reaction cylinder, $R_1 = 1.11$ cm) to those of Thonnard[10,11] ($R_2 = 2.22$ cm). Thonnard used the average decay rate in the analysis of his data; Table 4 shows Thonnard's values, my values (or a linear interpolation of my data to obtain values at the same pressures), and the numerical differences between the two. The P^2 dependence on pressure of this escape rate above 150 torr is to be understood as due to a volume process, independent of the gas container dimensions, so that the actual escape rate β is

$$\beta = \beta_o + cP^2, \tag{4.1}$$

where β_o is the escape rate of resonance photons when no volume processes are present. Pressure broadening theory then predicts that the difference between data taken with the two cells (using the late time escape rate) is[21]

$$\beta_{o1} - \beta_{o2} = \frac{1.125}{\tau\sqrt{\pi k_p}}\left[\frac{1}{\sqrt{R_1}} - \frac{1}{\sqrt{R_2}}\right] = \frac{0.197\sqrt{\lambda_o}}{\tau}\left[\frac{1}{\sqrt{R_1}} - \frac{1}{\sqrt{R_2}}\right] \tag{4.2}$$

where $k_p = \frac{\lambda_o N}{2\pi}\frac{g_2}{g_1}\frac{\gamma}{\gamma_c}$ and[40] $\gamma_c = 0.904\ \frac{\gamma\lambda_o^3 N}{6\pi^2}\frac{g_2}{g_1}$. Using[41] $\tau = 2.15 \times 10^{-9}$ sec, $\lambda_o = 1.048 \times 10^{-5}$ cm, $R_1 = 1.11$ cm, and $R_2 = 2.22$ cm,

TABLE 4

COMPARISON OF ESCAPE RATES FOR CYLINDERS OF DIFFERENT RADII

(Rates in μsec^{-1})

Pressure (torr)	Thonnard[a]	This Work[b]	Linear Interpolation of this Work	Experimental Difference[c]
20.4		0.384		
25	0.3452		0.386	0.041
30		0.389		
40		0.390		
50	0.2994		0.380	0.081
57		0.372		
85		0.350		
100	0.2565		0.342	0.086
147		0.315		
200	0.2598		0.349	0.089
300		0.418		
400	0.5572	0.607		0.050
500		0.856		
600	1.015	1.15		0.135
800	1.624			
1000	2.368			

[a] $R_2 = 2.22$ cm.

[b] $R_1 = 1.11$ cm.

[c] The average value of these differences is 0.080 μsec^{-1}. This is in agreement with the value 0.083 μsec^{-1} obtained from transport theory.

one obtains

$$\beta_{o1} - \beta_{o2} = (0.282 - 0.199) \times 10^6 \text{ sec}^{-1} = 0.083 \times 10^6 \text{ sec}^{-1},$$

in good agreement with the average of the values (0.080×10^6 sec^{-1}) of Table 4.

Using Equation (4.1) with $\beta_o = 0.282 \times 10^6$ sec^{-1} and applying a least squares fit to the measured rates from 150 torr to 600 torr, one obtains

$$C = 2.31 \text{ torr}^{-2} \text{ sec}^{-1} \tag{4.3}$$

as the rate coefficient from the three-body collisions which deplete the $^1P_1$ state, in agreement with Thonnard.[11] It was noted in examining the data from 300 to 600 torr that β plotted versus P^2 falls on a straight line which yields $C = 2.69$ torr^{-2} sec^{-1} and $\beta_o = 0.185$ μsec^{-1}; but due to the uncertainty in the high pressure values, the previously mentioned value for C is probably more significant, particularly since the low value of β_o is difficult to interpret.

Above 10 torr there is some doubt that the pressure broadening theory based on two-body collisions is valid, and hence the long lorentzian tail on the Voigt profile is suspect. This tail determines the resonance photon escape rates in this pressure region ($P > 10$ torr), and thus there is some doubt in the computed values of these escape rates. However, within the limits of experimental accuracy of Thonnard's and this experiment, the

$R^{-\frac{1}{2}}$ dependence in the late time behavior appears to be correct. The failure of the measured escape rates to obtain the lowest value (0.282×10^6 sec^{-1} here, 0.20×10^6 sec^{-1} in Thonnard's geometry) given by the transport theory may be due in part to 1) the geometrical effects discussed in Section 3.4, 2) a shorter natural lifetime of the $^1P_1$ state than the value given in Reference 41, 3) some phenomenon associated with the hump in the β versus P curve around 30 torr. This last possibility seems quite reasonable in view of the low value of β at 150 torr.

It should be mentioned at this point, in connection with data discussed in the following sections, that the measured average escape rate for the fast component decay, when examined at 70 torr, did not show any measurable change in any of the following situations: 1) rate measured at different wavelengths across the 1048 Å line (up to $\pm$ 5 Å at the exit slit of the monochromator), 2) repetition period of the beam decreased so that there was considerable buildup of the second component (which does not die out completely between pulses), 3) application of an electric field transverse to the beam. However, the field (200 V/cm) was too weak to remove an appreciable fraction of the ion pairs produced by the proton beam. Increasing the field strength resulted in light amplification.

4.3 The Fast Component Intensity

As the argon pressure in the reaction cell is increased from 10 to 300 torr, the wavelength at which most of the $^1P_1$ resonance radiation

escapes to the detector shifts gradually from 1048 to 1052.5 Å, then remains at 1052.5 Å as the pressure is increased above 300 torr. This effect was also observed by Hurst, Bortner, and Strickler.[16] Figure 16 shows this peak wavelength value as a function of pressure taken with various monochromator slit settings. The cause of this shift is not known at present, but is probably related to the long wavelength half of the self-reversed resonance line (perhaps it indicates the formation of an unresolved red satellite). In this experiment, a lithium fluoride window prevented argon gas from entering the monochromator chamber; thus, absorption of the 1048 Å photons over this one meter pathlength can be ruled out.

This phenomenon is introduced here due to its effect in the measured intensity of the "1048 Å" resonance line as follows. The lithium fluoride window transmission efficiency is appreciably different at 1048 Å and 1052 Å so that, as a result of the peak shift, more photons appear to escape at higher pressures. Folding together the peak shift curve of Figure 16 and with the transmission factor for the older lithium fluoride window[42] shown in Figure 17, one obtains a correction factor $\eta(P)$ for this effect (Figure 18). One multiplies the observed intensity at pressure P by $\eta(P)$ to obtain the true relative intensity. The intensity measurements reported in Section 4 have been adjusted in this way.

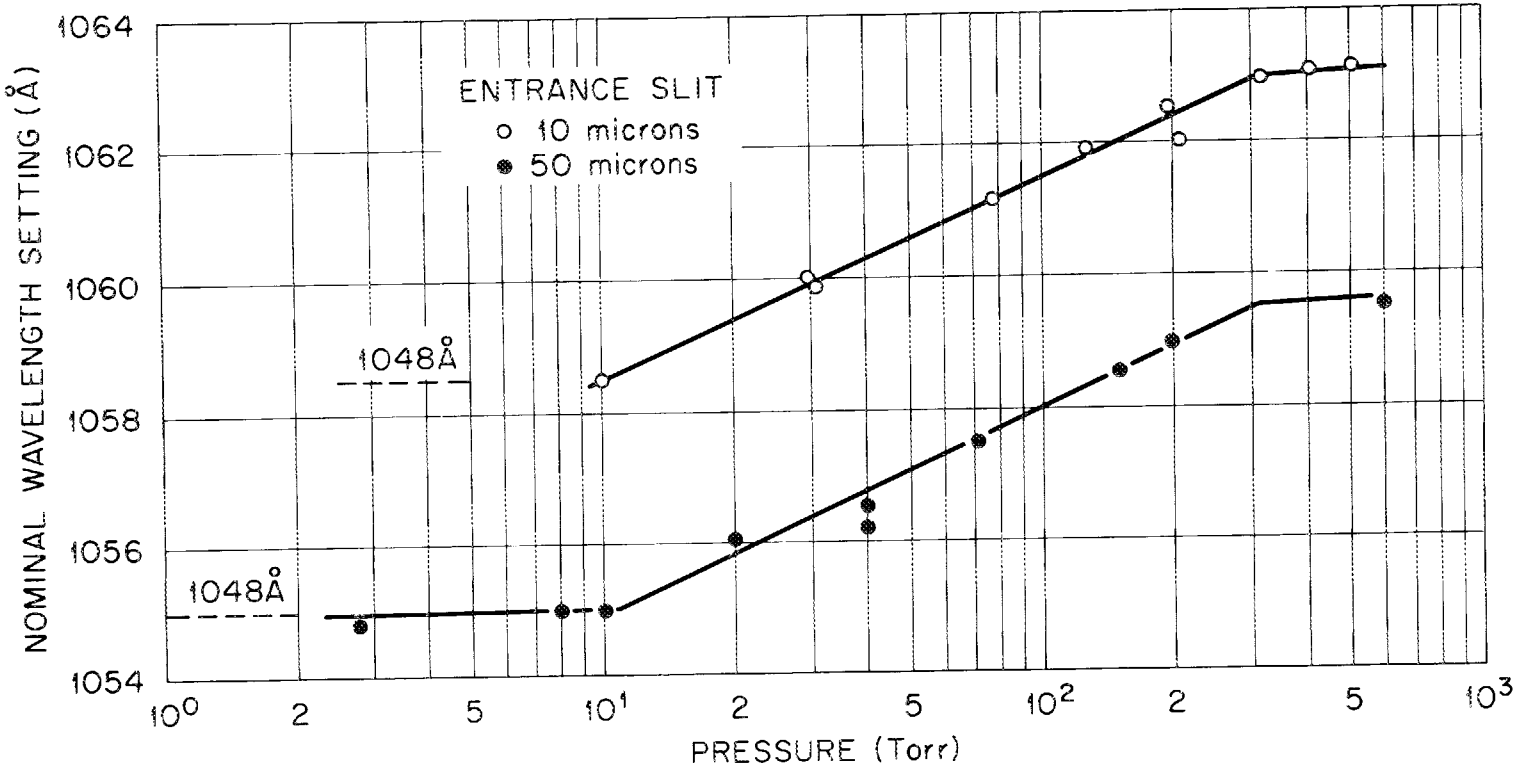

Figure 16. Argon $^1P_1$ Emission Peak Shift versus Pressure.

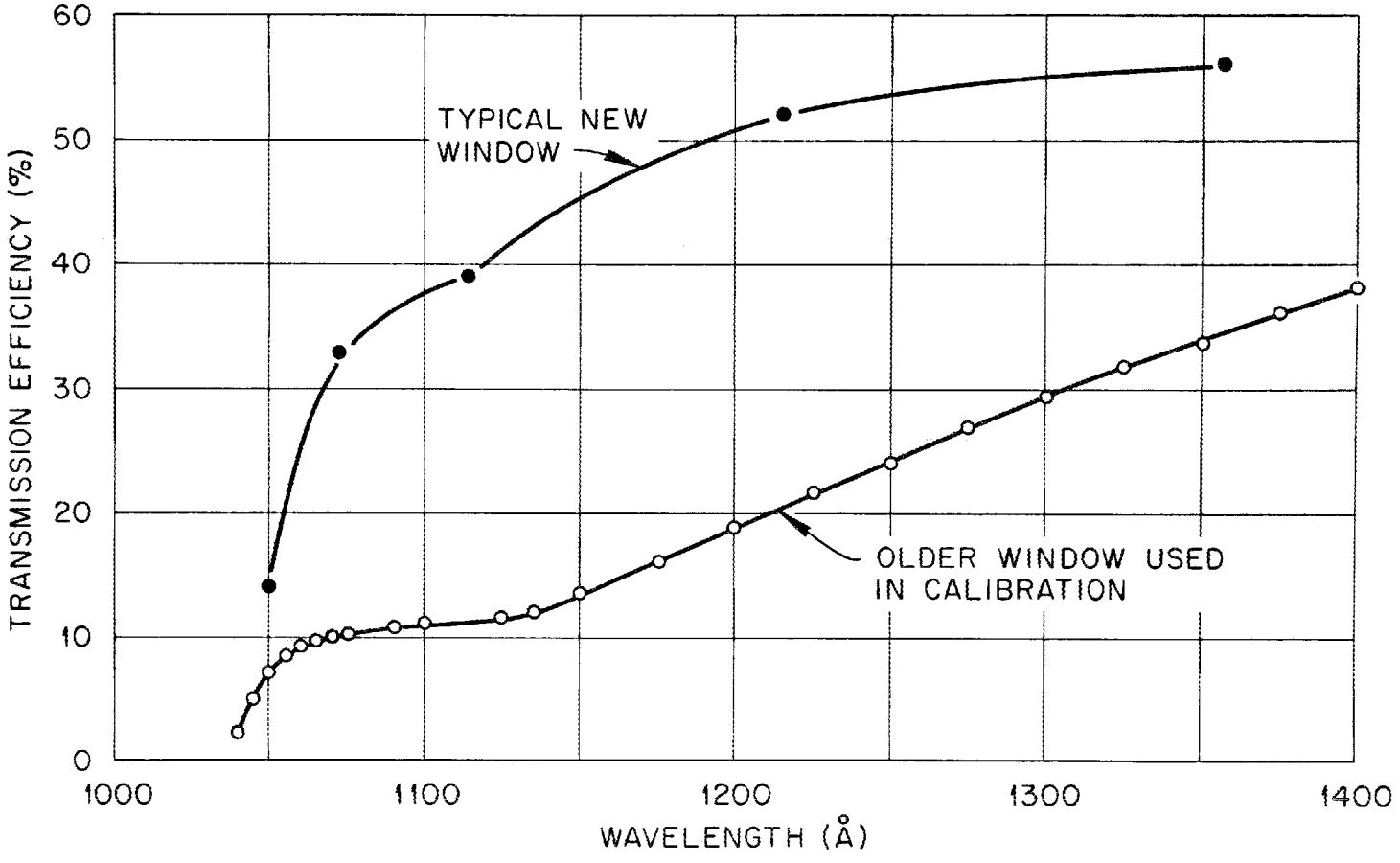

Figure 17. Lithium Fluoride Transmission Efficiency versus Wavelength.

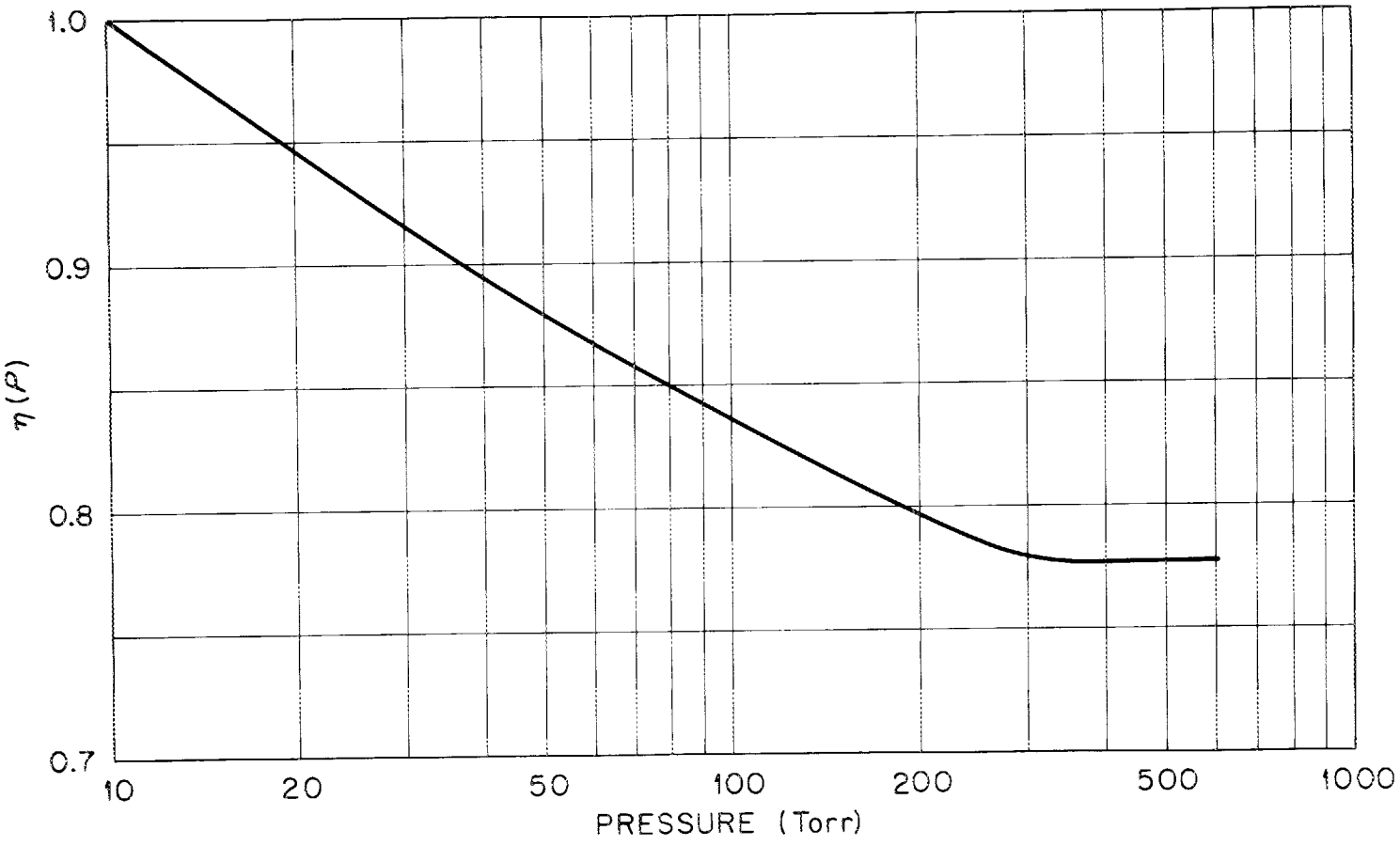

Figure 18. Correction to Observed Intensity due to 1048 Å Peak Shift and Lithium Fluoride Window Transmission. $I(P) = \text{constant} \times \eta(P) I_{obs}(P)$.

As the pressure is increased in the experiment, the grating is rotated to maintain the peak wavelength at the exit slit of the monochromator; the exit slit is open at 350 microns (entrance slit at 50 microns) which allows all the light from the 1048 Å line to pass to the detector, but negligible light from the 1067 Å emission.

The upper curve in Figure 19 shows the time integrated photon count (net intensity) at 1048 Å divided by pressure as a function of pressure. The values were obtained directly from a scaler (operating in parallel with the MCA) by correcting for the SEM background, divided by the proton current, adjusting for the window-peak shift effect and dividing by the pressure. In these experiments, the proton beam characteristics (average current, repetition period) were held constant to avoid a small nonlinear effect which will be discussed in Section 4.4. The repetition period of the beam was 128 μsec.

The lower curve in Figure 19 shows the time-integrated photon count for the fast component at 1048 Å divided by the pressure as a function of pressure. The values were obtained from the MCA in the following way. First, the number of counts in the fast component was computed from the formula

$$\sum N_F = N_F(1) + N_F(2) + \frac{N_F(3)}{1 - e^{-\lambda_F}}$$

where $N_F(I)$ is the number of counts in channel I after removing the second

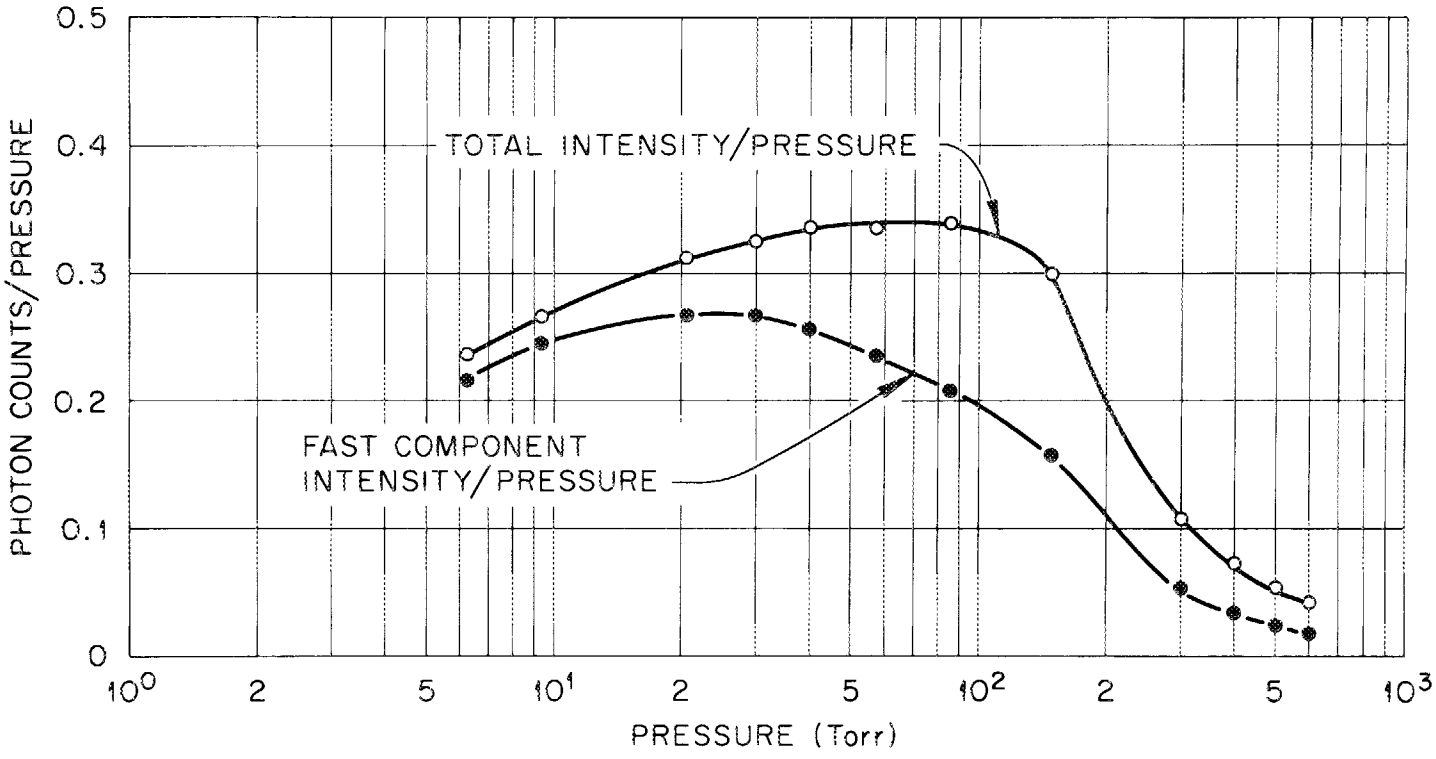

Figure 19. I(P)/P versus P for the Argon 1048 Å Resonance Radiation at High Pressures.

component (and hence the background), λ_F is the average fast-time slope in units of channel^{-1}. The first several channels were generally treated separately to avoid the fall-off effect often observed in the first channel. Then, the number ΣN_F was scaled up to account for deadtime in the MCA (as compared to the scaler). Finally, this value was divided by the proton current, corrected for the window-peak shift, and divided by the pressure. Note that in removing the second component, it was assumed to be nearly constant under the first component; if the second component is actually increasing during this time, the first component has been underestimated in comparison to the total count.

The slope of the fast component intensity at the low pressure end of these data is in agreement (i.e., well within experimental error associated with extracting the exponent from two data points) with

$$I = \text{constant} \times P^{1.31},$$

as found at lower pressures. As the pressure is increased, one approaches the region where the pressure-broadened profile alone governs photon escape; the distribution of excited $^1P_1$ states should become independent of pressure, and hence the geometrical effect discussed in Section 3 should no longer be important. One then expects the intensity of escaping resonance radiation to be directly proportional to pressure. From Figure 19 this is indeed true by 20 torr.

Above 30 torr, the intensity/pressure begins to decrease (the intensity itself decreases above approximately 120 torr), indicating that the energy associated with the $^1P_1$ level is being diverted along some other pathway than escape of resonance radiation.

4.4 The Second Component

The second or late component in the time-resolved intensity measurements is typically 15 to 30 times slower than the early component. The following characteristics are observed:

1. Above 150 torr, in the time region where both fast and slow components give equal contribution to the intensity, a plateau is observed suggesting a constant decay rate, at least over a short time period.
2. The decay of this component is then nearly exponential, but after several "half-lives" the decay becomes slower.
3. The decay rate increases with pressure. Figure 20 shows a plot of the second component decay rate as a function of pressure. The values plotted are obtained by assuming an exponential decay. Accuracy is estimated at $\pm$ 10% above 150 torr and somewhat worse at lower pressures due to the very slow decay rate, low intensity, and 80 μsec full scale limitation of the TPHC. Roughly fitting the data via a linear pressure dependence,

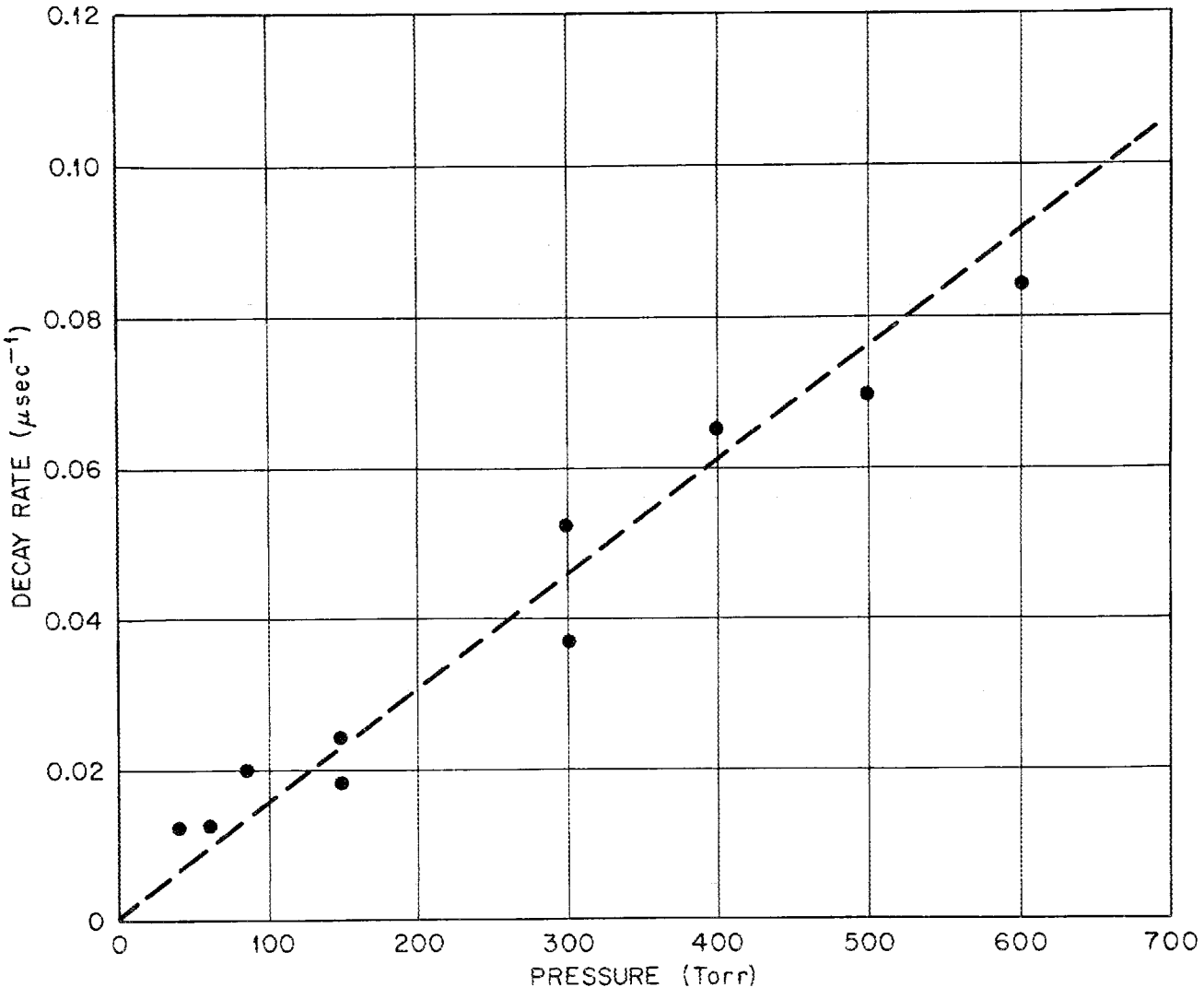

Figure 20. Second Component Escape Rate versus Pressure.

one obtains

$$\beta_s \approx 1.5 \times 10^{-4} P$$

where the pressure is in torr. However, this rate is very sensitive to impurities (see Reference 11 and Item 7 below).

4. The second component intensity is obtained by subtracting the MCA values for the fast component from the scaler values of the net photon count (correcting for background). This method insures that those photons which are emitted between the end of the TPHC time ramp and the next proton pulse are included (attempts to compute the number of these very late photons by extending the second component slope result in a small underestimate due to the slower decay rate at very late times). Figure 21 shows the ratio of fast-component intensity to the net intensity.
5. Using 2.0 MeV protons produces a much larger fraction for this second component than using 250 keV electrons. Thonnard's data[11] at 600 torr show that approximately 15% of the total light is coming from the second component when the electrons are used.
6. Early in the attempt to measure the relative photon count (as monitored by the SEM detector) as a function of pressure, it was discovered that this count depended in a non-linear way on the photon current. Figure 22 shows the typical photon count per

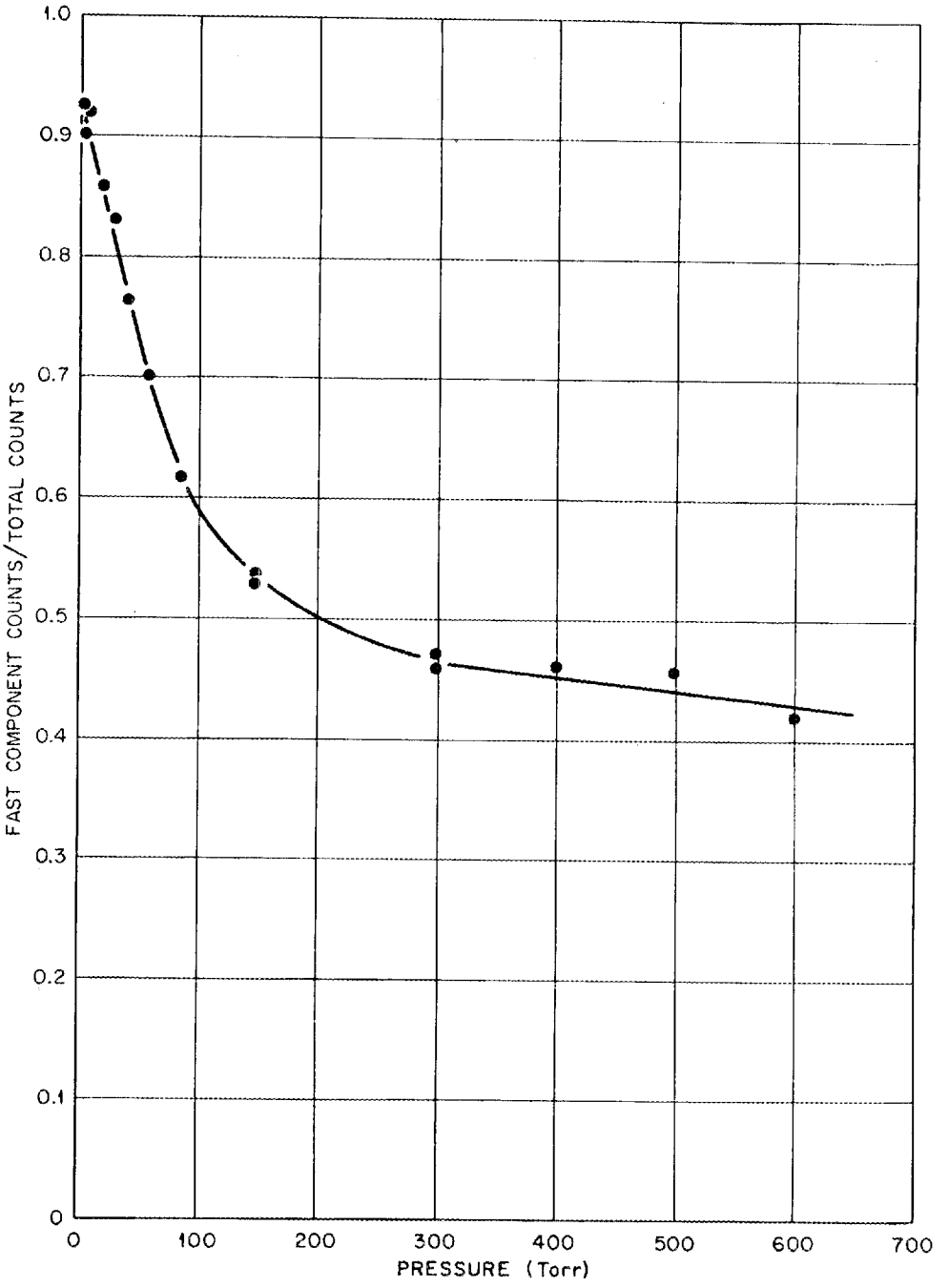

Figure 21. Fraction of Photons in Fast Component Peak versus Pressure.

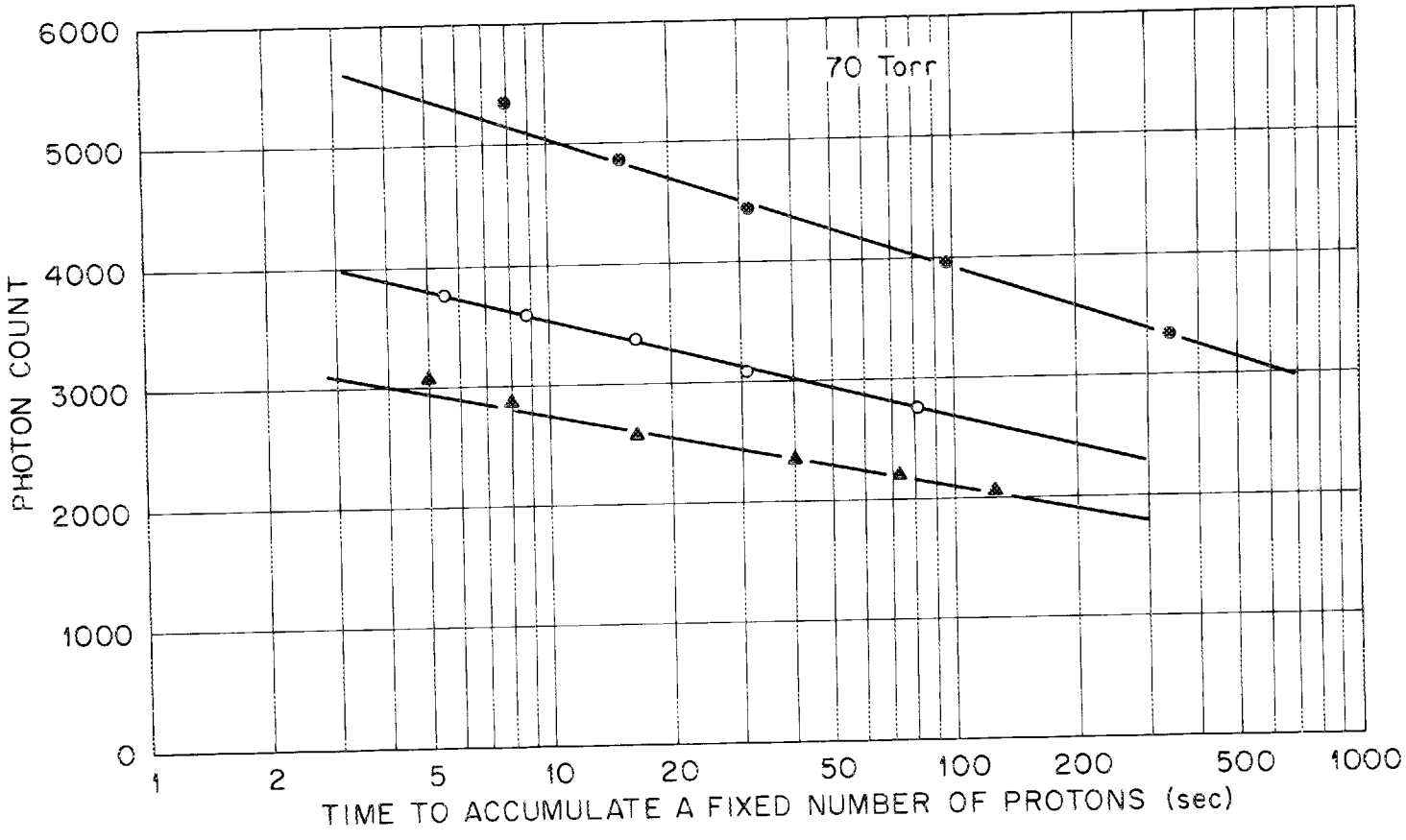

Figure 22. Non-linear Effect for Net Photon Count.

proton plotted versus the reciprocal of the time required to accumulate a fixed amount of charge from the proton beam (this is essentially the proton current) at 70 torr. The average beam current was varied by changing the repetition period of the beam without changing the number of protons in an individual pulse. Similar results were obtained by reducing the number of protons per pulse at a fixed repetition period, but this method was not pursued in detail. In effect, one finds that, as the average beam current is increased, more photons escape per proton introduced into the cylinder. Some additional time-resolved experiments indicate in a tentative way that the second component alone is responsible for this effect. The analysis is made quite difficult here by the problems of 1) separating the first and second components accurately and 2) the unfolding of the buildup in the second component due to be overlapping by consecutive beam pulses. A more recent time-resolved experiment by Hurst and Wagner,[43] performed by maintaining a fixed repetition period and varying the number of protons per pulse, shows quite clearly that the second component intensity depends on beam current.

7. Additional experiments by Hurst and Wagner,[43] performed by introducing small amounts of impurity to the argon gas, show that the second component intensity and decay rate depend

strongly on impurities, where (for these small amounts of impurity) the fast component is not appreciably effected.

8. The ratio of second component to first component intensity does not change when one examines the escaping photons at ± 5 Å from the peak (i.e., the grating is rotated so that the peak wavelength reaching the SEM detector is changed; lack of resolution permits some overlap). As mentioned earlier, escape rates for the two components are also independent of wavelength.

Associating this second component with the peak shift (since both become noticeable around 10 torr and saturate at 300 torr) appears to be ruled out by the last observation (Item 8). The presence of an impurity which radiates at 1048 Å also does not explain Item 7 or Item 8.

A good candidate for the source of these photons is the population of the $^1P_1$ state via recombination of argon ions with electrons (via ambipolar diffusion), followed by a cascade to the $^1P_1$ state. An attempt was made to examine this by placing a grid in the emission cell to collect the charge and prevent radiative recombination. A small effect was observed in the indicated direction (i.e., increased grid voltage, decreased ratio of second to first component), but difficulties associated with light amplification caused by the grid, coupled with problems in monitoring the proton current with the grid in operation, limit the interpretation of the experiment.

4.5 The Argon Model

One of the motivating reasons for studying the resonance trapping of the photons emitted from the $^1P_1$ state in argon is to understand the role played by these photons in the pathways taken by the energy deposited by the fast charged particles. Stewart[17,27] defines $d\epsilon/dx$ as the energy radiated in the vacuum ultraviolet emission spectra (from 1048 Å - 1400 Å in the case of argon) per unit length of proton path; if dE/dx is the stopping power, then

$$F_e = \frac{d\epsilon/dx}{dE/dx}$$

is a measure of the fraction of the deposited proton energy which appears as ultraviolet radiation. Stewart finds this fraction to be .23 to .29 in the 100 to 400 torr pressure region in argon. Hence, an understanding of the processes involved which lead to photon emission in this region of the spectrum gives an important part of the story of the interaction of protons with argon.

Figure 23 shows a schematic representation of a model developed by Thonnard and Hurst.[10,11] The $^1P_1$ and $^3P_1$ levels have appreciable oscillator strength (0.228 and 0.050, respectively[41]) and are populated directly by the fast charged particles. Secondary electron excitation and cascading from higher excited states will increase the population of these levels and also the $^3P_0$ and $^3P_2$ metastable states. Work by Lassettre[44] shows that cascading from a set of states between 13 and 13.5 eV will populate the $^1P_1$, $^3P_1$,

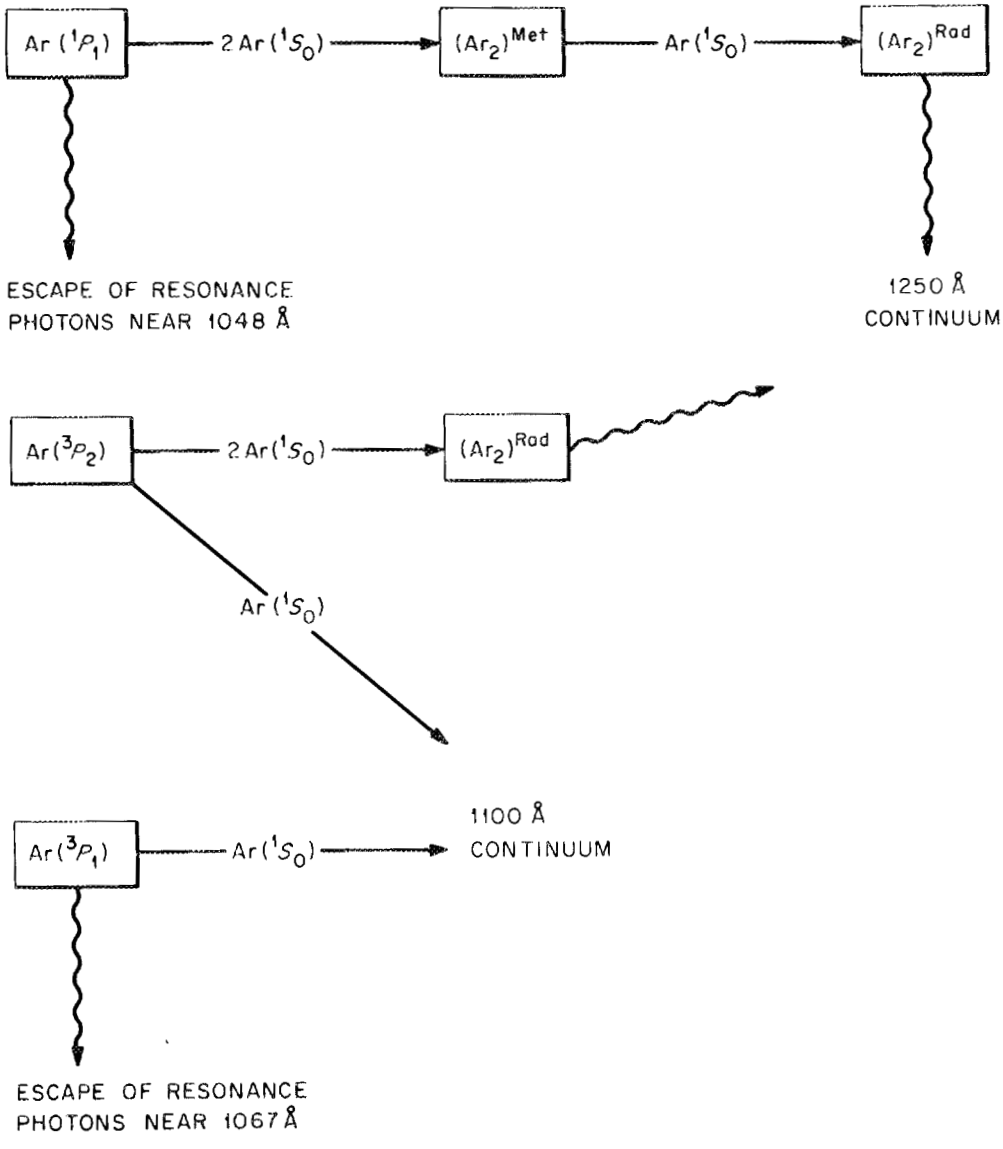

Figure 23. Argon Energy Pathways Model for the $^1P_1$, $^3P_1$, and $^3P_2$ States.

and $^3P_2$ levels. (The $^3P_0$ metastable state does not appear to contribute appreciably to the emission spectrum in this wavelength region. There is no evidence, at present, that this state is populated to the extent of the other three.)

Recombination of electrons with ion pairs will provide an additional source for these levels which may continue to contribute over an extended time period. Due to the repetitive nature of the pulsed electron or proton beam, a positive space charge should build up in the reaction cell which supplies the appropriate electric field to allow for equal escape rates to the walls for both electrons and ions (ambipolar diffusion). These positive charges then recombine with the diffusing electrons.

In examining the time dependent intensity at 1048 Å, 1067 Å, and in the 1250 Å continuum taken by Thonnard and in this work, a fast component and a distinctly different slow component are observed in each wavelength region. The fast component is interpreted as being derived from excitation of the atomic states by those processes which populate the levels within the first few nanosecond (i.e., $t < 50$ nsec) from the proton pulse. This includes direct excitation by the charged particle pulse, secondary electrons, cascading, gemini pair recombination along the fast charged particle track. The slow component is tentatively identified here as being derived from the recombination due to ambipolar diffusion.

The argon emission spectra shown in Figure 10 can be described in terms of processes which begin with the excited states $^1P_1$, $^3P_1$, and $^3P_2$. The peaks at 1048 Å and 1067 Å are atomic emissions from the $^1P_1$ and $^3P_1$ states.

Based on an examination of the time dependent intensities of the 1048 Å peak and 1250 Å continuum, Thonnard and Hurst have concluded that the model shown in Figure 23 describes the atomic processes leading to this continuum. The $^1P_1$ state, which has a natural lifetime of approximately 2×10^{-9} sec, has its effective lifetime extended several orders of magnitude by resonance trapping. Collisions occur between a $^1P_1$ state and two ground state atoms which result in a metastable argon molecule

$$Ar^*(^1P_1) + 2Ar(^1S_0) \rightarrow (Ar_2)^{met} + Ar(^1S_0) + KE.$$

This metastable molecule is converted to a radiating molecule $(Ar_2)^{rad}$ by a two-body collision with another ground state atom. Experiments by other researchers[45-48] indicate that the $^3P_2$ state is also being depleted by a three-body collision process; Hurst and Thonnard found that the time dependent intensity of the 1250 Å continuum can be described accurately over a wide pressure range if the states $^1P_1$ and $^3P_2$ contribute about equally to the formation of the molecules which radiate into this continuum. They point out that there is no strong evidence for two distinct radiating

molecules, but that the processes starting with the $^1P_1$ and $^3P_2$ levels could both lead to the same molecule.

Thonnard and Hurst find that the 1100 Å continuum has a more complex time dependence. The depletion rate of the $^3P_1$ state increases linearly with pressure above 25 torr, suggesting that a portion of the 1100 Å continuum is produced during a collision between an atom in the $^3P_1$ state and a ground state atom (i.e., a Franck-Condon process). The complicated decay rate suggests that the $^3P_2$ state also contributes to this continuum.

The present work has examined the depletion rate of the $^1P_1$ state in detail, but provides no new data on other states involved in the model. From Section 4.2, one obtains $2.3\ P^2\ sec^{-1}$ (P in torr) for the three-body conversion rate from the $^1P_1$ state to the metastable molecule, in agreement with Thonnard. Also, in that section, it is pointed out that the difference in decay rate between Thonnard's and these data up through several hundred torr can be explained in terms of the resonance transport theory.

An estimate has been obtained on the relative energy escaping from the resonance peak at 1048 Å plus the 1250 Å continuum at two different pressures to see if this is consistent with the Thonnard-Hurst model. This estimate was made in the following way.

1. Scans of the vuv spectrum were obtained at 2.9 torr and 203 torr via the Bristol recorder (peak values were verified with a scaler).

2. The total areas in the "1048" resonance peak (actually at 1052 Å at 203 torr) and the 1250 Å continuum were obtained from the spectrum scans. (The 1250 Å continuum intensity is almost negligible at 2.9 torr; an estimate was obtained for this value from a scaler measurement at the peak). These values were then normalized to the proton current.
3. The transmission efficiency of the lithium fluoride window[42] from the lower curve of Figure 17 was folded together with estimates of the grating and SEM detector efficiencies taken from Reference 17. The normalized areas in Step 2 were then corrected for this difference in detection efficiency at the different wavelengths (see Figure 24).
4. The fraction of the intensity due to direct excitation (i.e., area under the fast component in time dependent data) was obtained from Figure 21 for the 1048 Å emission. This fraction was 0.95 at 2.9 torr and 0.48 at 203 torr. An estimate of this fraction for the continuum made from a time dependent experiment at 1260 Å is 0.4. The values obtained in Step 3 are multiplied by these factors to eliminate intensity due to the second component. Denote these values by $I(\lambda, P)$. This is an important step as the second component is interpreted as an additional source for the $^1P_1$ state so that the net intensity in both the 1048 Å peak and the

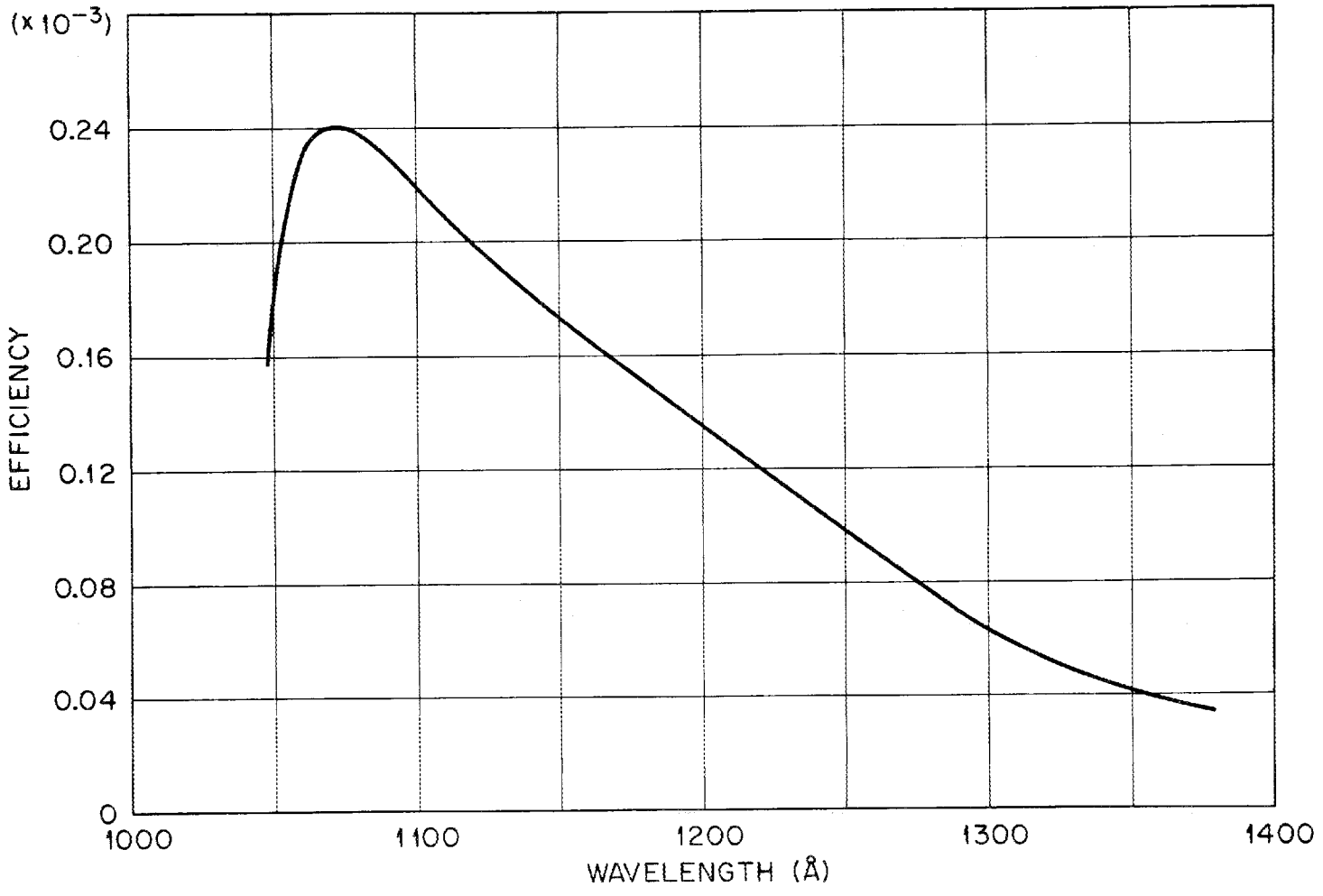

Figure 24. Estimated Net Detection Efficiency of Photons versus Wavelength.

1250 Å continuum will increase faster with pressure than the stopping power.

5. The expression $\frac{I(1048\,\text{Å}, P) + I(1250\,\text{Å}, P)}{(dE/dx)_p}$ is evaluated, where $(dE/dx)_p$ is the energy deposited by the proton beam per unit length of the proton path, evaluated at the mean energy of the protons at the entrance slit to the monochromator and at pressure P. Stopping power data were obtained from Janni.[30]

One obtains, at 2.9 torr, in relative numbers (the order in the above expression is maintained)

$$\frac{3.4 + 0.1}{101 \times 2.9} = 0.012$$

and at 203 torr,

$$\frac{66 + 1030}{108 \times 209} = 0.049 .$$

Then, define

$$F_B = \frac{0.049}{0.012} = 4.1 .$$

One thus finds that the energy appearing in the 1048 Å peak plus 1250 Å continuum, after normalizing to the energy deposited by the proton beam, increases by roughly a factor of 4 as the pressure is increased from 2.9 torr to 203 torr. If one takes into account various errors which may enter, F_B

is in reasonable agreement with the model of Thonnard and Hurst. This experiment is intended as only a rough estimate of the factor F_B.

From the analysis of the data and procedures used to obtain the factor F_B, the value is probably an upper bound. A detailed examination of the energy balance should perhaps be carried out in the following way.

1. An accurate calibration of the transmission efficiency of the lithium fluoride window, the reflection efficiency of the grating, and detection efficiency of the SEM should be obtained as a function of wavelength.
2. Careful thought should be given to the angular distribution of escaping photons which may change as a function of pressure (geometrical effect). Also, at lower pressures, the metastable argon molecule $(Ar_2)^{met}$ of Figure 23 exists for an appreciable time before being converted to the radiating molecule.[11] This allows time for diffusion of the excited molecules so that the escaping 1048 Å and 1250 Å radiation may not have the same angular distribution. A similar effect exists for the metastable $^3P_2$ atomic state.
3. The shape of the 1250 Å continuum is independent of pressure. (This was observed by Hurst, Bortner, and Strickler.[16]) The FWHM is approximately 90 Å. One can examine this shape carefully (it is nearly gaussian with the intensity falling off more

slowly than gaussian at longer wavelength), correlate the area to the peak value, then measure the intensity at the peak via a scaler. Thus, one can accumulate enough counts for good statistics and accurately normalize to the proton current.

4. The fraction of the 1250 Å continuum which arises from the slow component needs to be examined in more detail as a function of pressure.

5. The work of Thonnard and Hurst[10] shows that it is reasonable to assume that roughly equal contributions are made to the 1250 Å continuum by the $^1P_1$ and $^3P_2$ states, but that this rate perhaps changes with pressure. This should be included in the energy balance study. Making this correction alone would reduce F_B by about a factor of 2.

6. It would be instructive to examine the energy balance in this way over a wide pressure range, beginning as low as 1 torr where the continuum is negligible and few other complicating factors are present.

SECTION 5

SUMMARY

The transport of resonance radiation in argon has been studied in detail over a wide pressure range (0.002 to 600 torr). A collimated, pulsed beam of protons, traveling down the axis of an argon filled cylinder, produced an almost line source of argon $^1P_1$ excited states. The time dependence of escaping resonance photons was determined. The simple geometrical arrangement in this experiment made possible an accurate comparison between theory and experiment.

In examining the basic assumptions of resonance transport theory in terms of the photon escape rates obtained in this experiment, it is found that the assumption of complete redistribution in frequency for the trapped photons in each re-emission cannot be made at lower pressures (0.02 to 0.5 torr). When the collision rate between excited argon atoms and ground state atoms approaches the reciprocal of the natural lifetime, a correct theory must allow for coherent emission (in the rest frame of the atom) in the absence of a decorrelating collision. The results of this experiment show that the trapping time of resonance photons can be extended by as much as a factor of three due to this effect. At higher

pressures (1 to 10 torr), where at least one collision almost always occurs before emission from the $^1P_1$ state, the theory based on complete redistribution is in good agreement (within 10%) with this experiment.

Additional experiments to test the resonance transport theory should be undertaken using various values of experimental parameters such as the argon temperature, the cylinder radius, and the exit aperture value y_o. The argon emission from the $^3P_1$ level provides a different natural lifetime; the use of other noble gases should yield additional information. Further experiments with the argon $^1P_1$ level below 10 microns would test the low pressure transport theory where collisions can be neglected.

It was found in this experiment that many complicated effects become important at argon pressures above 10 torr. The resonance photon escape rate increases, then drops to a minimum near 150 torr, whereas the transport theory predicts a constant rate in this pressure region. At the higher pressures, a transport theory based on two-body interactions is in doubt as there is compelling evidence for interactions between an excited atom with two other atoms; however, comparison of the decay rates between this experiment and a similar experiment with a cylinder of different radius indicates that the transport theory correctly describes the effect of the boundary. As the pressure is increased from 10 to 300 torr, there is a $4\frac{1}{2}$ Å shift in the wavelength at which the photons

emitted from the $^1P_1$ level escape from the reaction cell. This is not understood. A delayed emission from the $^1P_1$ state produces a second component in the exponential decay curve which contributes as much as 55% of the escaping photons at 600 torr. Although it is believed at present that this second component is due to recombination of electrons with argon atomic or molecular ions followed by cascade to the $^1P_1$ state, further experiments are needed to clarify the time behavior. It is also important to observe the effect of an electric field on this component in an experiment where the ion pair density is very low.

The energy pathways model of Hurst and Thonnard[10] for the interaction of fast charged particles with argon has been found in this experiment to be consistent with the relative energy escaping from the gas near 1048 Å and around 1250 Å. Further experiments, similar to the absolute intensity measurements of Stewart,[17] need to be performed over a wide pressure range in argon which includes both the region where escape of 1048 Å radiation is the only important process and the region where the 1250 Å continuum dominates.

Current studies in the ongoing program at ORNL are examining the effects of quenching and changes in escape rate by an impurity gas of the $^1P_1$ and $^3P_1$ states. A detailed examination of the time dependence of the photon energy escaping at 1067 Å is underway. These are important steps in understanding the interaction of fast charged particles with argon.

For example, it is found that the second component which is observed in the $^1P_1$ emission is eliminated by the addition of small amounts of impurity. This effect may enable a more detailed study of the transport of resonance radiation at higher pressures.

APPENDIX 1

A COMPUTER CODE

In this appendix, a brief description and listing of the computer program BETAF are given. BETAF computes the value of β using Equation (3.12) for an arbitrary resonance line in our geometry.

All units are cgs except for the pressure which is in torr.

The asymptotic form of the Voigt profile

$$\varphi(X) = \exp(-X^2) + a/\pi^{\frac{1}{2}} X^2$$

is used for $X \geq 1$. Except at very low pressures ($k_o y_o/2 < 25$), most of the contribution from the integral for β comes from $X > 2$.

The following may help in the notation:

CNP: $N = P(\text{cgs})/kT = 1.013 \times 10^6 P(\text{torr})/(760\ kT) = \text{CNP} \times \text{PRESS}$.

XC: frequency at which $\exp(-X_C^2) = a/\pi^{\frac{1}{2}} X_C^2$, obtained by iteration of $X_C(n+1) = \left[\ln\left\{ \frac{\pi^{\frac{1}{2}}}{a} \ln\left(\frac{\pi^{\frac{1}{2}}}{a} X_C(n)^2 \right) \right\} \right]^{\frac{1}{2}}$.

XE: frequency at which $k_o y_o \varphi(X_E)/2 = TE$, obtained from FUNCTION XTEST which will not give a value of X less than unity.

The integration is carried out in the following way:

$$\beta/\gamma = 2\int_{o}^{X_I} f(x)dx + 2\int_{X_I}^{X_F} f(x)dx + 2\int_{X_F}^{\infty} f(x)dx.$$

The first integral is always neglected; X_I = max(1.0, XMIN) where XMIN is computed from XTEST using $k_o y_o \varphi(XMIN)/2$ = TMIN. The second integral is done by two point Gauss-Legendre quadrature using FUNCTION SUM(NI, NF, DX); XF ≡ QX = max(XC + 2, XMAX) + DX, where XMAX is computed from $k_o y_o a/2\pi^{\frac{1}{2}}(XMAX)^2$ = TMAX. This integration is carried out with intervals of 0.1 from XMIN to XC + 2 + δ, then, if needed, in intervals of 0.5 from XC + 2 + δ to XMAX + DX (δ is determined in each case by the integer arithmetic). The third integral is computed from an approximate analytic function valid for X > XMAX using FUNCTION REMAIN (XF).

```
**FTN,L,G,E,A.
      PROGRAM BETAF
      REAL KO
      COMMON TN,A,PC,XC
C ATOMIC TRANSITION DATA
      GAMMA=1.E+09/1.8
      WAVEL=1.048E-05
      GRATIO=3.
C GAS AND CONTAINER DATA
      YO=0.714
      TEMP=293.
      WT=39.94
      PRINT 103,GAMMA,YO,TEMP
C CONSTANTS
      PI=3.14159265
      SPI=1.77245385
      R=8.3143E+07
      BK=1.38054E-16
C SOME USEFUL INTERMEDIATE PARAMETERS
      VO=SQRT(2.*R*TEMP/WT)
      AO=WAVEL*GAMMA/(4.*PI*VO)
      CNP=1.013E+06/(760.*BK*TEMP)
      XINT=WAVEL**3*GRATIO*CNP
      ALPHA=0.904*XINT/(6.*PI**2)
      B=XINT/(8.*PI*VO)*GAMMA
      PRINT 100,VO,AO,CNP,ALPHA,B
C PRESSURE IN TORR
      INDEX=0
      DO 90 MX=1,14
      PRESS=.001*2.**MX/2.
C PRESSURE DEPENDENT PARAMETERS
      RGAM=ALPHA*PRESS
      GAMC=GAMMA*RGAM
      PC=1.
      A=AO*(1.+RGAM)
      KO=B*PRESS/SPI
      TN=KO*YO/2.
      SPIA=SPI/A
      PRINT 101,PRESS,RGAM,GAMC,KO,TN,PC,A
C EVALUATION OF XC,XE
      IF(INDEX)20,20,21
   20 XC=2.5
      INDEX=1
   21 XCT=SQRT(ALOG(SPIA*ALOG(SPIA*XC**2)))
      U=ABS(XCT-XC)
      XC=XCT
      IF(U-.001)22,22,21
   22 XC2=XC+2.0
      TE=1.0
      XE=XTEST(TE/TN,XC,A)
      PRINT 23,XC,XE
C SELECTION OF INTERVALS AND INTEGRATION
      IF(XE-XC+.5)30,30,40
   30 DX=.1
      NI=1./DX
      NF=XC2/DX
      QX=DX*FLOAT(NF+1)
```

```
      BOG=2.*SUM(NI,NF,DX)+REMAIN(QX)
      GO TO 70
   40 TMIN=10.
      TMAX=.05
      XMAX=SQRT(TN/(TMAX*SPIA))
      XMIN=XTEST(TMIN/TN,XC,A)
      PRINT 41,XMIN,XMAX
      IF(XMIN-XC2)50,43,43
   43 DX=.5
      NI=XMIN/DX
      NF=XMAX/DX
      QX=DX*FLOAT(NF+1)
      BOG=2.*SUM(NI,NF,DX)+REMAIN(QX)
      GO TO 70
   50 DX1=.1
      IF(XMAX.GT.XC2) GO TO 62
      NI=XMIN/DX1
      NF=XC2/DX1
      QX1=DX1*FLOAT(NF+1)
      BOG=2.*SUM(NI,NF,DX1)+REMAIN(QX1)
      GO TO 70
   62 DX2=.5
      NI1=XMIN/DX1
      NF1=(DX2*FLOAT(IFIX(XC2/DX2))+DX2-DX1)/DX1
      NI2=(NF1+1)*DX1/DX2
      NF2=XMAX/DX2
      QX2=DX2*FLOAT(NF2+1)
      BOG=2.*SUM(NI1,NF1,DX1)+2.*SUM(NI2,NF2,DX2)+REMAIN(QX2)
   70 BETA=BOG*GAMMA
      PRINT 102,BOG,BETA
   90 CONTINUE
   23 FORMAT(1X,3HXC=,F6.3,3X,3HXE=,F6.3)
   41 FORMAT(1X,5HXMIN=,F7.2,3X,5HXMAX=,F7.2)
  100 FORMAT(1X,3HVO=,E11.4,5H, AO=,F6.4,6H, CNP=,E11.4,8H, ALPHA=,F6.3,
     C4H, B=,E11.4)
  101 FORMAT(//,1X,9HPRESSURE=,F8.4,15H, GAMMAC/GAMMA=,F7.4,9H, GAMMAC=,
     CE11.4,5H, KO=,E11.4,5H, TN=,F6.0,5H, PC=,F6.4,4H, A=,F6.4)
  102 FORMAT(1X,11HBETA/GAMMA=,E11.4,4X,5HBETA=,E11.4)
  103 FORMAT(1H1,1X,6HGAMMA=,E11.4,5H, YO=,F5.3,14H, TEMPERATURE=,F5.1)
      STOP
      END


      FUNCTION ERFC(X)
      SUM=X
      T=X
      DO 1 N=1,1000
      U=2.*FLOAT(N)+1.
      T=(2.*T/U)*X**2
      SUM=SUM+T
      IF(T.LT.1.E-08) GO TO 3
    1 CONTINUE
      PRINT 33
   33 FORMAT(1X,3HOUT)
    3 ERFC=1.-(2./1.77245385)*EXP(-X**2)*SUM
      RETURN
      END
```

```
      FUNCTION XTEST(C,XC,A)
      IF(C.GT.0.4)GO TO 7
      ASPI=A/1.77245385
      U=2.*ASPI/XC**2
      IF(C-U)1,6,2
    1 P=.05
      GO TO 3
    2 P=-.05
    3 XT=XC
      DO 4 I=1,20
      XT=XT+P
      V=EXP(-XT**2)+ASPI/(XT**2)-C
      IF(P*V)5,8,4
    4 CONTINUE
      IF(P)7,7,9
    5 XTEST=XT-P/2.
      IF(XTEST.LT.1.) GO TO 7
      RETURN
    6 XTEST=XC
      RETURN
    7 XTEST=1.0
      RETURN
    8 XTEST=XT
      RETURN
    9 XTEST=SQRT(ASPI/C)
      RETURN
      END



      FUNCTION REMAIN(X)
      COMMON TN,A,PC
      PI=3.14159265
      SPI=1.77245385
      WPC=1.-PC
      ETA=SQRT(TN*A/SPI)
      V=ETA/X
      TPR=.01
      REMAIN=2.*A*PC/(PI*ETA)*(WPC*V+PC*SPI/3.*(1.-ERFC(V))+PC*V/3.*E2(V
     C**2)-V**3*PC*G(TPR,WPC)/(3.0*TPR))
      PRINT 49,REMAIN
   49 FORMAT(1X,10HREMAINDER=,E12.5)
      RETURN
      END



      FUNCTION SUM(NI,NF,DX)
      PX=DX*.57735027/2.
      SUM=0.0
      DO 1 I=NI,NF
      X=(FLOAT(I)+.5)*DX
    1 SUM=SUM+F(X+PX)+F(X-PX)
      SUM=SUM*DX/2.
      PRINT 2,NI,NF,SUM
    2 FORMAT(1X,3HNI=,I4,3X,3HNF=,I4,3X,4HSUM=,E11.4)
      RETURN
      END
```

```
      FUNCTION G(T,AL)
      IF(AL-1.E-7)1,1,4
    1 G=0.0
      RETURN
    4 IF(T.LE.10.)GO TO 3
      G=AL/(1.-AL)
      RETURN
    3 PI=3.14159265
      Z=0.57735027
      PMIN=0.
      PMAX=25.
      DP=.1
      NI=1.+PMIN/DP
      NF=PMAX/DP
      A=(1.-Z)*DP/2.
      B=(1.+Z)*DP/2.
      SUM=0.
      DO 2 I=NI,NF
      PX=FLOAT(I-1)*DP
      PA=PX+A
      PB=PX+B
      RA=ATAN(PA)/PA
      RB=ATAN(PB)/PB
    2 SUM=SUM+RA**2/(1.-AL*RA)*SIN(PA*T)/PA+RB**2/(1.-AL*RB)*SIN(PB*T)/P
     CB
      G=AL/PI*DP*SUM
      RETURN
      END


      FUNCTION E2(X)
      SUM=-.577215665-ALOG(X)
      IF(X.GT.5.) GO TO 2
      U=-1.
      DO 1 I=1,50
      AI=I
      U=-X*U/AI
      V=U/AI
      SUM=SUM+V
      Y=ABS(V)
      IF(Y.LT.1.E-08)GO TO 3
    1 CONTINUE
      GO TO 3
    2 E2   =EXP(-X)*(1./(X+2.)+2./(X+2.)**3-4./(X+2.)**4)
      RETURN
    3 E2   =EXP(-X)-X*SUM
      RETURN
      END
```

```
      FUNCTION F(X)
      COMMON TN,A,PC,XC
      XCM=XC-1.
      PI=3.14159265
      SPI=1.77245385
      XS=X**2
      IF(X.GT.XCM)GO TO 1
      PHI=EXP(-XS)/SPI
      AL=0.
      GO TO 2
    1 BX=1.+(SPI/A)*XS*EXP(-XS)
      PHI=A*BX/(PI*XS)
      AL=(1.-PC)/BX
    2 T=TN*SPI*PHI
      WAL=1.-AL
      F=WAL*PHI*(AL+WAL*E2(T)-WAL*G(T,AL))
      RETURN
      END
```

APPENDIX 2

DATA LISTING

The unreduced data used in the final analysis are listed in this appendix. All runs were at 1048 Å or adjusted to follow the $^1P_1$ peak above 10 torr. The SEM background in counts per channel can be estimated from the channel width and repetition period of the proton pulse (recalling that the TPHC ramp terminates before the next proton pulse). The first column lists the channel number of values in the second column.

Run No. 88. Pressure: 600 torr. Channel Width: 0.3295 μsec. Pulse Period: 128 μsec. Proton Count: 2×10^{-7} coul. Time: 102.0 sec. Photon Background: 1.7 counts/sec.

1	1	0	84	44	54	53	43	54
9	47	50	36	54	33	46	68	43
17	63	59	50	65	57	56	60	58
25	82	66	81	76	87	85	85	79
33	75	89	79	109	81	95	103	85
41	98	104	101	114	99	122	125	121
49	124	124	144	163	129	148	159	172
57	145	174	181	176	189	190	177	230
65	187	216	218	226	210	211	218	216
73	208	213	220	215	269	253	343	416
81	599	769	999	1390	1963	2654	2519	10
89	7	2	5	4	4	5	4	6
97	3	3	5	0				

Run No. 89. Pressure: 498 torr. Channel Width: 0.3295 μsec. Pulse Period: 128 μsec. Proton Count: 4×10^{-7} coul. Time: 219.7 sec. Photon Background: 1.7 counts/sec.

1	1	0	200	117	88	113	104	107
9	112	126	120	127	111	120	124	133
17	121	153	132	147	139	149	140	135
25	156	169	159	161	157	141	164	164
33	184	171	182	184	187	208	230	223
41	229	219	245	225	253	239	239	268
49	269	251	265	279	265	276	319	299
57	312	320	332	323	368	335	363	393
65	380	366	380	399	378	367	412	400
73	382	482	526	584	656	861	1024	1185
81	1477	1976	2359	3149	4075	5069	3283	19
89	11	7	14	7	13	9	8	14
97	10	18	10	0				

Run No. 90. Pressure: 396 torr. Channel Width: 0.3295 μsec. Pulse Period: 128 μsec. Proton Count: 4×10^{-7} coul. Time: 223.2 sec. Photon Background: 1.4 counts/sec.

1	0	0	223	145	126	110	141	139
9	125	147	122	135	146	169	138	148
17	123	161	152	137	171	180	163	150
25	193	161	176	173	172	195	204	188
33	193	201	196	201	211	223	195	225
41	251	244	238	255	259	275	267	265
49	282	267	301	263	283	274	296	291
57	286	319	327	296	330	309	334	338
65	341	387	324	350	401	437	489	505
73	536	636	670	804	983	1085	1258	1498
81	1716	2137	2469	3095	3587	4351	2831	14
89	18	7	12	11	12	13	6	13
97	15	16	11	0				

Run No. 91. Pressure: 297 torr. Channel Width: 0.3295 μsec. Pulse Period: 128 μsec. Proton Count: 2×10^{-7} coul. Time: 121.4 sec. Photon Background: 1.4 counts/sec.

1	2	0	144	69	72	67	65	73
9	77	83	87	90	62	87	87	70
17	75	88	85	69	97	83	101	83
25	91	79	113	84	122	104	112	110
33	120	130	125	105	110	120	106	112
41	110	103	103	124	129	117	175	154
49	165	126	144	162	142	168	147	159
57	148	172	165	183	146	209	198	247
65	211	224	256	271	290	275	346	377
73	409	459	503	591	615	714	752	862
81	992	1131	1307	1403	1684	1850	1120	11
89	7	10	9	7	4	11	6	9
97	14	6	10	0				

Run No. 92. Pressure: 297 torr. Channel Width: 0.3295 μsec. Pulse Period: 128 μsec. Proton Count: 4×10^{-7} coul. Time: 214.3 sec. Photon Background: 1.4 counts/sec.

1	1	0	269	210	161	171	157	148
9	157	184	172	167	154	149	191	171
17	175	182	190	189	177	187	161	173
25	206	192	202	235	225	182	224	235
33	233	243	231	244	239	246	246	229
41	243	231	256	263	262	284	278	270
49	311	303	310	325	331	339	351	344
57	334	362	356	366	357	393	452	421
65	430	513	512	502	559	667	676	719
73	829	915	973	1138	1194	1392	1632	1775
81	2008	2260	2485	2892	3250	3819	2225	24
89	13	25	14	16	13	18	10	14
97	21	15	12	0				

Run No. 93. Pressure: 147 torr. Channel Width: 0.3295 μsec. Pulse Period: 128 μsec. Proton Count: 4×10^{-7} coul. Time: 230.3 sec. Photon Background: 1.4 counts/sec.

1	1	0	320	192	164	191	182	180
9	166	199	158	171	170	179	178	198
17	205	189	191	182	185	175	212	208
25	188	199	203	194	210	214	231	207
33	202	225	249	225	233	246	227	268
41	257	264	256	291	273	264	296	316
49	294	312	291	335	335	375	375	442
57	416	439	458	447	528	560	571	607
65	634	680	787	841	967	963	1073	1185
73	1295	1376	1506	1591	1836	1885	2115	2254
81	2533	2808	3129	3444	3852	4262	2610	31
89	37	27	33	28	36	29	38	23
97	32	41	25	0				

Run No. 94. Pressure: 147 torr. Channel Width: 0.6596 μsec. Pulse Period: 128 μsec. Proton Count: 4×10^{-7} coul. Time: 215.1 sec. Photon Background: 1.4 counts/sec.

1	0	0	320	206	182	172	155	159
9	168	166	163	179	171	149	179	193
17	192	213	192	192	234	207	192	213
25	190	226	206	218	219	244	267	259
33	259	249	271	298	270	261	270	271
41	276	285	306	267	282	284	295	335
49	289	380	309	306	344	356	365	355
57	354	395	378	363	426	380	418	434
65	422	438	465	460	495	484	518	487
73	552	545	615	652	685	689	796	852
81	958	1110	1303	1543	1685	2030	2345	2634
89	3253	3888	4641	5562	7058	8015	584	70
97	64	45	63	0				

Run No. 95. Pressure: 84.9 torr. Channel Width: 0.6596 μsec. Pulse Period: 128 μsec. Proton Count: 4×10^{-7} coul. Time: 205.5 sec. Photon Background: 1.4 counts/sec.

1	1	0	151	90	81	69	91	96
9	81	104	86	98	85	106	81	91
17	106	117	92	103	101	86	101	119
25	125	95	126	125	122	135	116	101
33	125	117	148	150	137	160	112	150
41	143	145	147	148	143	166	165	151
49	137	160	164	153	165	177	141	193
57	164	197	170	191	188	174	178	210
65	187	200	181	228	194	215	188	211
73	245	221	268	290	348	351	406	441
81	579	668	748	892	1034	1216	1553	1844
89	2254	2651	3320	4097	5270	6776	1144	41
97	30	30	35	0				

Run No. 96. Pressure: 57.2 torr. Channel Width 0.6596 μsec. Pulse Period: 128 μsec. Proton Count: 4×10^{-7} coul. Time: 210.6 sec. Photon Background: 1.4 counts/sec.

1	1	0	86	43	44	53	38	53
9	48	49	46	64	56	46	52	44
17	72	53	59	59	51	61	44	73
25	51	44	68	59	62	71	61	69
33	68	66	82	66	53	65	81	74
41	70	75	77	72	65	77	65	80
49	86	86	108	92	69	88	88	100
57	75	98	79	73	89	61	104	91
65	86	83	82	89	91	110	89	115
73	132	117	134	156	155	195	228	244
81	299	323	451	536	646	769	953	1237
89	1484	1856	2409	3081	3857	5206	872	19
97	29	19	16	0				

Run No. 97. Pressure: 40.0 torr. Channel Width: 0.6596 μsec. Pulse Period: 128 μsec. Proton Count: 4×10^{-7} coul. Time: 205.4 sec. Photon Background: 1.4 counts/sec.

1	2	0	62	36	24	23	28	33
9	30	24	27	30	35	29	23	29
17	30	48	31	33	36	27	25	38
25	26	33	37	41	28	29	38	36
33	34	46	43	35	39	42	29	29
41	38	29	38	32	37	34	43	52
49	42	49	44	40	54	35	49	29
57	51	52	40	57	36	44	65	62
65	53	49	51	45	68	63	51	66
73	66	57	72	83	92	94	144	165
81	163	198	297	362	422	538	702	778
89	1074	1319	1736	2262	2984	3931	741	14
97	8	16	12	0				

Run No. 98. Pressure: 29.7 torr. Channel Width: 0.6596 μsec. Pulse Period: 128 μsec. Proton Count: 4×10^{-7} coul. Time: 202.4 sec. Photon Background: 1.4 counts/sec.

1	1	0	27	19	25	17	24	27
9	18	18	13	13	21	16	14	20
17	18	23	21	26	14	24	20	20
25	21	21	15	20	17	21	17	14
33	12	17	26	18	13	17	18	20
41	20	25	22	25	26	26	25	28
49	25	25	27	13	22	26	32	26
57	23	22	34	23	42	33	22	30
65	30	36	28	31	31	37	29	39
73	33	38	55	57	63	63	84	82
81	114	142	216	228	335	389	484	627
89	793	1034	1184	1621	2228	3011	538	5
97	13	10	6	0				

Run No. 99. Pressure: 20.4 torr. Channel Width: 0.6596 μsec. Pulse Period: 128 μsec. Proton Count: 8×10^{-7} coul. Time: 472.2 sec. Photon Background: 1.1 counts/sec.

1	0	0	34	18	16	18	16	17
9	19	19	23	22	15	15	19	19
17	12	14	27	23	25	21	24	18
25	16	22	19	30	22	16	17	15
33	16	24	28	17	27	12	24	21
41	21	14	26	27	19	26	26	29
49	24	23	21	23	22	23	21	23
57	42	24	23	24	22	21	22	30
65	38	24	28	34	38	32	41	42
73	59	55	58	63	68	76	113	149
81	176	211	250	344	425	538	622	834
89	998	1300	1710	2255	2951	3912	601	20
97	11	15	22	0				

Run No. 103. Pressure: 9.35 torr. Channel Width: 0.6596 μsec. Pulse Period: 128 μsec. Proton Count: 2.4×10^{-6} coul. Time: 1710.8 sec. Photon Background: 1.0 counts/sec.

1	6	0	37	20	14	22	19	21
9	24	23	19	20	25	19	25	27
17	24	17	23	23	28	19	28	16
25	25	18	23	24	30	17	24	22
33	13	24	28	26	21	33	19	19
41	22	14	21	20	23	22	20	13
49	20	23	19	25	20	28	23	22
57	26	27	26	28	25	23	18	26
65	30	32	45	48	30	46	43	58
73	71	67	96	93	109	140	167	221
81	256	308	380	417	503	685	826	1012
89	1291	1516	2053	2478	3200	4121	534	23
97	15	15	17	0				

Run No. 104. Pressure: 6.25 torr. Channel Width: 0.6596 μsec. Pulse Period: 128 μsec. Proton Count: 2×10^{-6} coul. Time: 1927.7 sec. Photon Background: 1.0 counts/sec.

1	2	0	35	22	20	9	11	18
9	15	19	11	16	11	12	18	14
17	19	20	14	12	13	21	16	21
25	17	15	7	12	10	13	15	21
33	19	15	22	10	16	21	15	14
41	11	14	17	16	21	15	17	13
49	15	14	14	13	13	21	14	16
57	16	13	16	17	26	19	32	23
65	24	25	23	20	26	44	40	33
73	38	40	64	55	58	75	104	102
81	132	176	175	245	276	339	435	515
89	606	761	981	1217	1537	2043	373	21
97	17	13	18	0				

Run No. 105. Pressure: 152 torr. Channel Width: 0.6596 μsec. Pulse Period: 128 μsec. Proton Count: 2.15×10^{-7} coul. Time: 143.2 sec. Photon Background: 1.0 counts/sec.

1	2	0	168	83	89	92	94	104
9	101	96	95	110	94	97	114	105
17	96	102	110	110	110	96	109	111
25	110	121	122	141	129	116	121	132
33	122	128	116	122	120	154	121	137
41	139	151	130	135	164	160	146	170
49	144	150	174	141	154	170	196	171
57	160	178	178	183	211	199	200	206
65	190	207	253	235	218	259	233	264
73	264	249	296	334	321	360	394	466
81	488	532	643	750	846	1086	1132	1347
89	1635	1867	2162	2679	3241	3943	928	43
97	27	30	26	0				

Run No. 122. Pressure: 4.7 torr. Channel Width: 0.3279 μsec. Pulse Period: 64 μsec. Proton Count: 1×10^{-5} coul. Time: 253.7 sec. Photon Background: 2.5 counts/sec.

1	0	0	59	37	36	38	29	28
9	29	33	41	30	34	21	38	29
17	35	31	31	28	32	22	30	36
25	35	33	35	28	43	31	41	51
33	33	37	36	35	36	40	24	47
41	31	31	37	40	27	35	31	36
49	38	43	31	41	48	44	44	55
57	42	41	50	58	55	53	63	62
65	53	47	63	69	59	93	76	123
73	79	95	92	118	141	137	135	145
81	157	179	176	215	258	253	279	298
89	371	350	389	420	455	502	562	643
97	738	741	770	920	1012	1089	1205	1328
105	1503	1583	1769	1913	2189	2430	2718	2994
113	3197	3779	4045	4670	5386	5897	3584	22
121	17	26	20	22	16	22	25	0

Run No. 125. Pressure: 0.86 torr. Channel Width: 0.3279 μsec. Pulse Period: 64 μsec. Proton Count: 7×10^{-5} coul. Time: 1724.5 sec. Photon Background: 1.2 counts/sec.

1	3	0	38	36	25	24	17	29
9	24	29	27	19	23	25	25	22
17	14	31	24	20	27	16	22	31
25	27	20	26	23	21	18	27	29
33	26	19	20	24	18	19	28	17
41	35	27	20	28	34	26	31	25
49	29	32	22	27	18	21	34	35
57	40	35	35	37	42	39	33	29
65	48	49	52	46	49	57	56	63
73	55	82	80	95	90	106	113	126
81	116	129	173	151	182	179	191	260
89	257	292	323	349	363	441	463	543
97	575	658	702	770	863	908	1144	1201
105	1313	1498	1636	1842	2017	2377	2617	2881
113	3286	3528	4055	4556	5021	5587	3041	27
121	17	26	20	24	18	20	30	0

Run No. 129. Pressure: 0.56 torr. Channel Width: 0.3289 μsec. Pulse Period: 64 μsec. Proton Count: 1.3×10^{-4} coul. Time: 3419.7 sec. Photon Background: 0.83 counts/sec.

1	5	0	33	16	13	18	22	20
9	18	23	21	22	14	22	20	30
17	28	16	22	22	16	18	21	33
25	16	18	14	11	15	17	27	23
33	13	18	19	18	19	33	22	27
41	18	20	17	20	28	17	21	36
49	25	23	28	21	24	29	23	32
57	22	35	30	34	31	36	40	35
65	42	39	56	46	40	56	55	75
73	71	58	83	111	88	96	107	107
81	107	140	168	138	152	182	194	240
89	252	286	291	349	369	418	443	550
97	571	649	761	734	813	946	1053	1189
105	1261	1431	1657	1892	1996	2243	2435	2685
113	3095	3402	3925	4415	4847	5405	3063	15
121	16	15	18	20	18	15	13	0

Run No. 151. Pressure: 0.0147 torr. Channel Width: 0.3289 μsec. Pulse Period: 32 μsec. Proton Count: 7.2×10^{-4} coul. Time: 1.08×10^{4} sec. Photon Background: 0.53 counts/sec.

1	10	0	115	83	77	57	59	73
9	48	56	78	55	72	60	59	69
17	53	73	58	50	75	63	54	60
25	66	63	54	59	60	61	56	76
33	61	63	58	44	63	69	63	65
41	66	56	67	50	63	47	62	55
49	51	51	60	68	72	73	69	65
57	64	70	83	70	72	71	82	75
65	80	104	80	112	99	[124	141	154
73	180	186	193	230	245	296	313	376
81	452}	192	74	61	52	55	63	67
89	67	57	49	39	75	73	44	73
97	70	47	0	0				

Run No. 173. Pressure: 1.07 torr. Channel Width: 0.3313 μsec. Pulse Period: 32 μsec. Proton Count: 8×10^{-5} coul. Time: 1151.2 sec. Photon Background: 0.55 counts/sec.

1	2	0	12	14	8	15	11	15
9	6	12	10	21	11	14	10	10
17	16	21	18	17	12	17	13	14
25	14	14	12	25	18	22	21	18
33	24	28	29	25	40	40	33	40
41	49	50	55	50	58	70	79	76
49	75	96	114	106	113	127	161	186
57	196	169	222	227	290	281	319	361
65	413	455	500	523	607	653	768	803
73	936	1024	1097	1248	1452	1579	1807	2096
81	2301	2544	2864	3072	613	7	8	11
89	14	13	8	10	11	4	15	5
97	8	13	0	0	0	0	0	0
105	0	0	0	0	0	0	0	0
113	0	0	0	0	0	0	0	0
121	0	0	0	0	0	0	0	0

Run No. 175. Pressure: 0.57 torr. Channel Width: 0.3313 μsec. Pulse Period: 32 μsec. Proton Count: 2.4×10^{-4} coul. Time: 3545 sec. Photon Background: 0.60 counts/sec.

1	2	0	57	32	38	31	37	34
9	22	44	31	32	36	24	41	24
17	29	44	31	42	39	44	54	48
25	46	40	46	49	49	68	76	79
33	75	74	81	95	96	103	153	116
41	127	164	152	180	184	214	216	262
49	239	303	304	362	412	456	490	561
57	527	699	701	774	874	910	1029	1110
65	1303	1463	1644	1789	1999	2198	2473	2769
73	3124	3474	3877	4238	3452	33	41	26
81	29	22	25	27	19	26	21	32
89	40	23	25	28	23	28	18	34
97	18	21	0	0	0	0	0	0
105	0	0	0	0	0	0	0	0
113	0	0	0	0	0	0	0	0
121	0	0	0	0	0	0	0	0

Run No. 176. Pressure: 1.94 torr. Channel Width: 0.3313 μsec. Pulse Period: 32 μsec. Proton Count: 4×10^{-5} coul. Time: 584.2 sec. Photon Background: 0.60 counts/sec.

1	2	0	14	13	12	7	22	18
9	8	15	16	6	10	18	9	10
17	15	19	11	16	18	20	23	15
25	20	24	26	29	33	44	38	44
33	43	63	38	53	67	58	77	78
41	100	81	120	127	147	133	130	192
49	206	172	214	249	264	309	334	368
57	407	493	496	618	636	669	717	839
65	964	1056	1193	1287	1396	1754	1798	2074
73	2292	2649	2974	3241	2603	10	12	5
81	11	4	6	12	10	8	10	7
89	8	5	3	5	9	9	12	11
97	9	8	0	0	0	0	0	0
105	0	0	0	0	0	0	0	0
113	0	0	0	0	0	0	0	0
121	0	0	0	0	0	0	0	0

Run No. 180. Pressure: 0.184 torr. Channel Width: 0.3306 μsec. Pulse Period: 32 μsec. Proton Count: 9.6×10^{-4} coul. Time: 1.477×10^{4} sec. Photon Background: 0.60 counts/sec.

1	14	0	211	110	86	102	85	114
9	100	107	101	114	106	101	107	111
17	105	101	117	91	104	130	98	126
25	127	126	125	126	144	134	126	122
33	127	137	139	136	173	168	162	188
41	216	208	201	243	266	288	288	314
49	317	346	423	386	437	438	504	550
57	573	596	698	739	838	904	982	1063
65	1191	1288	1372	1446	1627	1824	2006	2238
73	2425	2644	2991	3145	2538	98	85	98
81	70	80	86	82	97	92	86	93
89	89	90	84	111	101	88	98	80
97	100	76	0	0	0	0	0	0
105	0	0	0	0	0	0	0	0
113	0	0	0	0	0	0	0	0
121	0	0	0	0	0	0	0	0

Run No. 182. Pressure: 0.406 torr. Channel Width: 0.3306 μsec. Pulse Period: 32 μsec. Proton Count: 2.4×10^{-4} coul. Time: 3.91×10^{3} sec. Photon Background: 0.60 counts/sec.

1	1	0	45	24	34	36	33	25
9	34	24	17	35	28	36	29	34
17	36	35	34	42	36	49	40	30
25	27	44	39	58	48	42	55	51
33	53	61	50	60	86	67	86	97
41	76	87	94	95	109	129	138	170
49	186	173	206	233	251	297	298	323
57	371	401	453	508	522	621	675	705
65	806	842	978	1097	1216	1328	1560	1688
73	1859	2119	2321	2537	2012	29	23	24
81	15	38	29	26	26	33	37	24
89	26	32	33	22	28	34	25	27
97	23	27	0	0	0	0	0	0
105	0	0	0	0	0	0	0	0
113	0	0	0	0	0	0	0	0
121	0	0	0	0	0	0	0	0

Run No. 194. Pressure: 0.093 torr. Channel Width: 0.3289 μsec. Pulse Period: 32 μsec. Proton Count: 2.64×10^{-3} coul. Time: 2.97×10^{4} sec. Photon Background: 0.50 counts/sec.

1	16	0	292	169	150	139	148	125
9	158	160	154	135	151	151	154	160
17	140	156	155	168	150	179	183	162
25	137	154	144	207	179	165	164	180
33	168	172	188	195	185	205	213	243
41	198	222	200	248	251	238	303	277
49	289	333	329	338	367	392	448	480
57	438	509	494	541	550	636	722	770
65	800	841	919	974	1114	1207	1328	1408
73	1529	1709	1823	1995	2055	213	161	131
81	141	165	167	144	135	152	144	150
89	151	136	147	152	170	165	140	145
97	151	139	0	0	0			

Run No. 197. Pressure: 0.042 torr. Channel Width: 0.3289 μsec. Pulse Period: 32 μsec. Proton Count: 3.2×10^{-3} coul. Time: 3.56×10^{4} sec. Photon Background: 0.50 counts/sec.

1	14	0	345	192	196	188	188	202
9	166	202	195	184	155	171	198	160
17	191	176	184	190	165	203	178	180
25	179	166	197	179	188	187	180	195
33	185	195	181	172	190	200	192	187
41	181	216	204	215	203	203	230	220
49	222	242	231	257	243	245	286	273
57	274	314	338	333	337	372	381	375
65	390	445	463	519	570	592	600	715
73	759	831	907	948	1002	195	188	178
81	173	192	169	173	179	175	165	145
89	155	186	181	171	160	181	184	159
97	161	163	0	0	0	0	0	0
105	0	0	0	0	0	0	0	0
113	0	0	0	0	0	0	0	0
121	0	0	0	0	0	0	0	0

Run No. 207. Pressure: 5.17 torr. Channel Width: 0.3317 μsec. Pulse Period: 32 μsec. Proton Count: 4×10^{-5} coul. Time: --- sec.
Photon Background: 0.50 counts/sec.

1	1	0	184	116	91	112	99	101
9	101	88	108	105	111	101	97	81
17	115	99	102	107	118	113	102	110
25	107	102	94	92	99	105	105	126
33	122	135	139	153	156	185	170	192
41	182	201	236	224	264	255	267	327
49	323	379	379	486	470	504	519	572
57	607	727	775	776	922	981	1109	1197
65	1310	1426	1691	1843	1966	2154	2404	2768
73	3019	3487	4016	4309	4926	3868	104	87
81	93	93	97	76	96	104	117	96
89	98	88	111	90	98	97	87	114
97	86	43	0	0	0	0	0	0
105	0	0	0	0	0	0	0	0
113	0	0	0	0	0	0	0	0
121	0	0	0	0	0	0	0	0

Run No. 208. Pressure: 5.19 torr. Channel Width: 0.3293 μsec. Pulse Period: 32 μsec. Proton Count: 4×10^{-5} coul. Time: 382.2 sec.
Photon Background: 0.5 counts/sec.

1	0	0	65	49	43	41	50	56
9	53	1553	2432	2211	1922	1731	1525	1410
17	1195	1131	1022	857	819	692	622	600
25	564	490	440	440	372	365	337	312
33	255	278	218	197	189	181	164	170
41	159	155	115	121	112	114	101	91
49	83	68	79	67	65	73	77	55
57	61	59	60	56	56	36	40	52
65	48	58	63	56	55	54	49	37
73	55	62	51	59	50	48	57	48
81	51	58	55	42	43	52	52	53
89	43	48	38	57	46	59	52	50
97	59	43	50	38	57	57	54	60
105	55	39	1369	2405	2134	1918	1750	1603
113	1422	1312	1118	1090	902	809	790	691
121	589	575	493	450	414	376	382	0

Run No. 217. Pressure: 5.25 torr. Channel Width: 0.1650 μsec. Pulse Period: 32 μsec. Proton Count: 3×10^{-5} coul. Time: 360.0 sec. Photon Background: 0.4 counts/sec.

1	98	86	115	110	117	92	91	113
9	131	115	113	130	122	136	136	143
17	155	162	133	168	163	181	189	190
25	191	201	204	205	239	229	270	259
33	268	280	265	286	309	310	325	350
41	355	395	402	403	432	415	469	499
49	509	541	538	583	591	659	632	631
57	680	683	794	831	770	879	954	959
65	1017	1079	1133	1167	1141	1226	1328	1430
73	1427	1577	1659	1659	1806	1840	1920	2097
81	2220	2331	2370	2508	2641	2727	2943	3093
89	3336	3369	3616	3787	4056	4208	4433	4737
97	5012	5396	5557	5798	6166	6519	6923	7329
105	7805	8201	8707	9398	9890	10396	11018	11883
113	12452	13237	14059	11489	53	42	38	46
121	39	46	48	32	62	44	41	0

Run No. 220. Pressure: 0.135 torr. Channel Width: 0.1650 μsec. Pulse Period: 64 μsec. Proton Count: 2.8×10^{-4} coul. Time: 4.32×10^{3} sec. Photon Background: 0.4 counts/sec.

1	11	10	16	8	17	11	19	16
9	11	17	18	19	9	16	14	18
17	21	13	20	16	19	17	23	9
25	20	13	20	18	25	15	28	20
33	24	19	28	23	27	29	36	30
41	35	28	32	43	44	37	44	51
49	52	54	42	57	49	47	49	63
57	55	76	82	88	86	63	79	76
65	104	109	83	101	124	119	122	117
73	153	128	133	149	176	182	193	195
81	203	223	194	222	231	236	262	282
89	300	290	310	382	394	381	416	421
97	427	452	499	501	543	592	644	616
105	646	711	803	746	846	912	921	979
113	1056	1088	1080	337	10	2	3	6
121	4	10	5	7	6	7	4	0

Run No. 224. Pressure: 0.069 torr. Channel Width: 0.1650 μsec. Pulse Period: 64 μsec. Proton Count: 6.4×10^{-4} coul. Time: 1.12×10^{4} sec. Photon Background: 0.43 counts/sec.

1	38	20	11	17	27	26	25	23
9	21	23	19	14	26	27	26	24
17	30	26	22	28	23	26	30	31
25	22	34	33	28	38	37	30	33
33	36	37	34	26	31	40	44	53
41	49	49	49	52	59	64	74	69
49	65	68	68	81	71	85	94	86
57	82	97	94	80	120	103	132	133
65	136	156	120	153	152	152	167	175
73	201	184	214	188	206	253	234	241
81	270	277	284	290	351	343	372	341
89	385	412	411	400	511	483	547	612
97	593	648	647	670	738	788	797	836
105	937	823	30	12	24	18	13	6
113	13	14	11	21	13	10	11	18
121	10	7	13	18	17	18	14	0

Run No. 238. Pressure: 0.206 torr. Channel Width: 0.1650 μsec. Pulse Period: 64 μsec. Proton Count: 1.92×10^{-3} coul. Time: 3.11×10^{4} sec. Photon Background: 0.5 counts/sec.

1	61	32	49	43	37	41	35	33
9	43	34	50	48	42	46	51	37
17	36	34	34	45	53	39	41	28
25	30	35	47	38	34	46	33	44
33	51	47	48	45	54	40	36	60
41	56	50	37	54	37	52	48	52
49	58	59	62	57	76	74	66	69
57	89	70	82	84	70	81	91	96
65	104	91	112	106	139	124	116	133
73	127	138	148	129	140	156	150	168
81	196	197	185	228	232	250	272	286
89	275	288	329	354	354	377	422	426
97	461	509	498	564	664	632	719	731
105	810	651	38	41	39	25	28	44
113	35	30	41	44	42	40	40	42
121	36	40	29	25	42	37	35	0

Run No. 242. Pressure: 0.0100 torr. Channel Width: 0.1650 μsec. Pulse Period: 64 μsec. Proton Count: 1.04×10^{-3} coul. Time: 1.85×10^{4} sec. Photon Background: 0.48 counts/sec.

1	33	7	22	25	26	28	24	28
9	24	25	15	27	19	22	27	21
17	24	26	26	21	20	29	22	30
25	12	23	28	13	28	18	27	25
33	20	28	18	16	20	27	20	26
41	35	24	20	29	14	25	16	28
49	23	23	22	22	22	24	22	22
57	26	25	20	32	27	25	31	27
65	24	35	24	15	27	31	30	47
73	28	42	32	29	33	22	36	37
81	52	56	46	56	60	56	66	62
89	77	79	84	96	101	119	135	117
97	132	146	166	198	201	223	239	266
105	285	259	27	16	25	26	21	18
113	29	22	19	20	24	19	13	26
121	33	22	22	24	25	18	25	0

Run No. 244. Pressure: 0.50 torr. Channel Width: 0.1650 μsec. Pulse Period: 64 μsec. Proton Count: 1.2×10^{-4} coul. Time: 2.01×10^{3} sec. Photon Background: 0.48 counts/sec.

1	24	10	13	9	15	12	20	18
9	15	21	17	17	21	10	18	19
17	26	28	20	34	25	27	36	25
25	38	41	50	53	50	41	39	59
33	48	45	51	57	62	62	69	69
41	82	85	87	89	105	116	102	97
49	107	101	128	143	134	160	155	145
57	190	182	154	221	223	243	208	250
65	266	297	275	294	320	352	383	425
73	370	430	462	465	508	538	524	584
81	591	676	682	740	751	849	858	873
89	964	1048	1133	1211	1223	1321	1298	1464
97	1503	1629	1733	1845	1931	2065	2290	2245
105	2370	1359	5	8	7	3	4	5
113	2	5	5	3	1	9	4	2
121	5	4	3	8	6	5	5	0

Run No. 249. Pressure: 0.0015 torr. Channel Width: 0.0814 μsec. Pulse Period: 16 μsec. Proton Count: 3.52×10^{-3} coul. Time: 1.28×10^{4} sec. Photon Background: 0.48 counts/sec.

1	35	25	24	36	29	21	31	32
9	42	25	33	29	23	34	33	35
17	34	37	31	44	27	26	28	29
25	31	31	34	37	36	16	44	35
33	34	31	29	21	26	31	20	31
41	23	36	31	44	27	33	27	19
49	31	26	26	33	27	32	36	26
57	28	26	27	25	31	27	28	25
65	35	32	32	30	28	19	21	27
73	35	32	26	30	21	26	37	32
81	33	33	43	30	34	20	35	36
89	30	29	35	37	33	31	28	33
97	28	29	35	27	37	38	25	39
105	26	41	31	50	50	47	60	71
113	92	161	214	223	30	30	37	28
121	30	21	38	27	31	29	35	0

LIST OF REFERENCES

1. A. C. G. Mitchell and M. W. Zemansky, Resonance Radiation and Excited Atoms (Cambridge University Press, Cambridge, 1961).

2. T. Holstein, Phys. Rev. 72, 1212 (1947).

3. T. Holstein, Phys. Rev. 83, 1159 (1951).

4. L. M. Bieberman, J. Exptl. Theoret. Phys. (U.S.S.R.) 17, 416 (1946).

5. K. T. Compton, Phys. Rev. 20, 283 (1922); E. A. Milne, J. Lond. Math. Soc. 1, 1 (1926).

6. M. G. Payne, J. E. Talmage, G. S. Hurst, and E. B. Wagner (in preparation).

7. C. E. Klots and V. E. Anderson, J. Chem. Phys. 56, 120 (1972).

8. D. G. Hummer, Mon. Nat. R. Astr. Soc. 125, 21 (1962); D. G. Hummer, Final Report, AFSWC Contract No. AF29(601)-6013.

9. D. M. Bartell, Dissertation, University of Kentucky (1972).

10. N. Thonnard and G. S. Hurst, Phys. Rev. A 5, 1110 (1972).

11. N. Thonnard, Dissertation, University of Kentucky (1971).

12. P. K. Leichner (in preparation).

13. J. E. Parks, Dissertation, University of Kentucky (1970).

14. J. E. Parks, G. S. Hurst, T. E. Stewart, and H. L. Weidner, J. Chem. Phys. 57, 5467 (1972).

15. G. S. Hurst, T. E. Bortner, and R. E. Glick, J. Chem. Phys. 42, 713 (1965).

16. G. S. Hurst, T. E. Bortner, and T. D. Strickler, Phys. Rev. 178, 4 (1969).

17. T. E. Stewart, Dissertation, University of Kentucky (1970).

18. T. E. Stewart, G. S. Hurst, D. M. Bartell, and J. E. Parks, Phys. Rev. A 3, 1991 (1971).

19. H. L. Weidner, Dissertation, University of Kentucky (in preparation).

20. G. S. Hurst, T. E. Stewart, and J. E. Parks, Phys. Rev. A 2, 1717 (1970).

21. M. G. Payne and J. D. Cook, Phys. Rev. A 2, 1238 (1970).

22. J. J. Hopfield, Astrophys. J. 72, 133 (1930).

23. R. E. Huffman, J. C. Larrabee, and Y. Tanaka, Appl. Opt. 4, 1581 (1965).

24. Y. Tanaka and K. Yoshino, J. Chem. Phys. 53, 2012 (1970).

25. P. G. Wilkinson, Can. J. Phys. 45, 1715 (1967).

26. G. S. Hurst, T. E. Bortner, and T. D. Strickler, J. Chem. Phys. 49, 2460 (1968).

27. T. E. Stewart, G. S. Hurst, T. E. Bortner, J. E. Parks, F. W. Martin, and H. L. Weidner, J. Opt. Soc. Am. 60, 1290 (1970).

28. U. Fano, Phys. Rev. 70, 44 (1946).

29. P. Warneck, J. Opt. Soc. Am. 55, 921 (1965).

30. J. F. Janni, Air Force Weapons Laboratory Technical Report No. AFWL-TR-65-150 (September 1966).

31. J. A. R. Samson, Techniques of Vacuum Ultraviolet Spectroscopy (John Wiley and Sons, Inc., New York, 1967), pp. 69-74.

32. The design and operation of this model is described by W. G. Wolber, B. D. Klettke, and P. W. Graves, Rev. Sci. Instr. 41, 724 (1970).

33. I am indebted to E. B. Wagner at ORNL for the design of this circuit.

34. D. F. Heath and P. A. Sacher, Appl. Opt. 5, 937 (1966).

35. A. H. Laufer, J. A. Pirog, and J. R. McNesby, J. Opt. Soc. Am. 55, 64 (1965).

36. W. G. Wolber, B. D. Klettke, and H. K. Lintz, Rev. Sci. Instr. 40, 1634 (1969).

37. W. L. Wiese, M. W. Smith, and B. M. Glennon, Atomic Transition Probabilities, NBS NSRDS 4, Vol. 1 (U. S. Dept. of Commerce, Washington, D.C., 1966).

38. M. T. Kelley at ORNL has developed a conversational language (ORCAL) for use on the ND-812 computer, ORNL-TM-3697 (February 1972).

39. P. J. Walsh, Phys. Rev. 116, 511 (1969).

40. P. R. Berman and W. E. Lamb, Phys. Rev. 187, 221 (1969).

41. G. M. Lawrence, Phys. Rev. 175, 40 (1968).

42. The lithium fluoride transmission efficiencies were kindly determined by E. T. Arakawa at ORNL.

43. G. S. Hurst and E. B. Wagner (in preparation).

44. E. N. Lassettre, A. Skerbele, M. A. Dillon, and K. J. Ross, J. Chem. Phys. 48, 5066 (1968).

45. A. V. Phelps and J. P. Molnar, Phys. Rev. 89, 1202 (1953).

46. L. Colli, Phys. Rev. 95, 892 (1954).

47. A. H. Futch and F. A. Grant, Phys. Rev. 104, 356 (1956).

48. E. Ellis and N. D. Twiddy, J. Phys. B 2, 1366 (1969).

INTERNAL DISTRIBUTION

1. Biology Library
4. Central Research Library
5. Document Reference Section
6. Reactor Division Library
7-31. Laboratory Records Dept. (LRD)
32. Laboratory Records (ORNL-RC)
33. ORNL Patent Office
34-35. Y-12 Technical Library
36. J. A. Auxier
37. C. F. Barnett
38. R. D. Birkhoff
39. T. A. Carlson
40. L. G. Christophorou
41. R. N. Compton
42. S. Datz
43. W. R. Garrett
44. F. F. Haywood
45-69. G. S. Hurst
70. G. D. Kerr
71. C. E. Klots
72-86. M. G. Payne
87. R. H. Ritchie
88. H. C. Schweinler
89. W. S. Snyder
90. J. A. Stockdale
91. J. H. Thorngate
92. J. R. Totter
93-103. E. B. Wagner
104. C. D. Cooper (C)
105. G. Cowper (C)
106. H. David (C)
107. E. Gerjuoy (C)
108. H. Harrenstien (C)
109. W. G. McMillan (C)
110. L. V. Spencer (C)

EXTERNAL DISTRIBUTION

111. Peter Ausloos, Radiation Chemistry Branch, National Bureau of Standards, Gaithersburg, Maryland 20760.
112. D. M. Bartell, Dept. of Physics, University of Western Ontario, London 72, Ontario, Canada.
113. J. W. Boring, Research Lab of Engineering Science, University of Virginia, Charlottesville, Virginia 22901.
114. T. E. Bortner, 100 Endicott Lane, Oak Ridge, Tennessee 37830.
115. Werner Brandt, Dept. of Physics, New York University, New York, N.Y. 10003.
116. R. S. Caswell, Radiation Physics Laboratory, National Bureau of Standards, Washington, D.C. 20234.
117. Joseph C. Y. Chen, Institute for Radiation Physics and Aerodynamics, University of California, LaJolla, California 92037.
118. P. J. Chantry, Westinghouse Research Laboratories, Pittsburg, Pennsylvania 15235.
119. L. W. Cochran, Administration Bldg., University of Kentucky, Lexington, Kentucky 40506.
120. R. W. Crompton, Research School of Physical Sciences, The Australian National University, Ion Diffusion Unit, Box 4, P.O., Canberra, A.C.T., 2600 Australia.

121. D. C. Conway, Dept. of Chemistry, Texas A and M University, College Station, Texas 77843.
122. Wendell C. DeMarcus, Dept. of Physics and Astronomy, University of Kentucky, Lexington, Kentucky 40506.
123. Fletcher Gabbard, Dept. of Physics and Astronomy, University of Kentucky, Lexington, Kentucky 40506.
124. W. A. Glass, Battelle Northwest Labs, P. O. Box 999, Richland, Washington 99352.
125. R. E. Glick, Institute of Molecular Biophysics, Florida State University, Tallahassee, Florida 32306.
126. B. R. Gossick, Dept. of Physics and Astronomy, University of Kentucky, Lexington, Kentucky 40506.
127. Alex E. S. Green, Dept. of Physics and Astronomy, University of Florida, Gainesville, Florida 32601.
128. R. H. Huebner, Argonne National Laboratory, 9700 S. Cass Avenue, Argonne, Illinois 60439.
129. Mitio Inokuti, Radiation Physics Division, Argonne National Laboratory, 9700 S. Cass Avenue, Argonne, Illinois 60439.
130. H. C. Jacobson, Dept. of Physics, University of Tennessee, Knoxville, Tennessee 37916.
131. William P. Jesse, 1324 Maple Ave., Downers Grove, Illinois 60515.
132. R. Katz, Dept. of Physics, University of Nebraska, Lincoln, Nebraska 68508.
133. R. E. Knight, Dept. of Physics and Astronomy, University of Kentucky, Lexington, Kentucky 40506.
134. H. A. Koehler, Lawrence Radiation Laboratory, P. O. Box 808, Livermore, California 94550.
135. E. N. Lassettre, Mellon Institute, 4400 Fifth Ave., Pittsburgh, Pennsylvania 15213.
136. P. K. Leichner, Dept. of Physics and Astronomy, University of Kentucky, Lexington, Kentucky 40506.
137. D. C. Lorents, Stanford Research Institute, Menlo Park, California 94025.
138. E. W. McDaniel, School of Physics, Georgia Institute of Technology, Atlanta, Georgia 30332.
139. Marcus T. McEllistrem, Dept. of Physics and Astronomy, University of Kentucky, Lexington, Kentucky 40506.
140. J. E. Parks, Dept. of Physics, Western Kentucky University, Bowling Green, Kentucky 42101.
141. J. C. Person, Argonne National Laboratory, 9700 S. Cass Ave., Argonne, Illinois 60439.
142. A. V. Phelps, Joint Institute for Laboratory Astrophysics, University of Colorado, Boulder, Colorado 80302.

143. H. H. Rossi, Radiological Research Laboratory, Columbia University, 630 West 168th St., New York, N. Y. 10032.
144. Wimberly C. Royster, Dean of the Graduate School, University of Kentucky, Lexington, Kentucky 40506.
145. Donald Sands, Dept. of Chemistry, University of Kentucky, Lexington, Kentucky 40506.
146. G. J. Schulz, Mason Laboratory, Yale University, 400 Temple St., New Haven, Connecticut 06520.
147. Maxine Sheets, Division of Biomedical and Environmental Research, U.S. Atomic Energy Commission, Washington, D.C. 20545.
148. T. E. Stewart, Midwestern Baptist Theological Seminary, 5001 N. Oak Street Trafficway, Kansas City, Missouri 64118.
149-158. J. E. Talmage, 105 Principia Lane, Oak Ridge, Tennessee 37830.
159. N. Thonnard, Dept. of Teresstrial Magnetism, Carnegie Institute of Washington, 5241 Broad Branch Rd., NW, Washington, D.C. 20015.
160. D. A. Vroom, Gulf Radiation Technology, Gulf General Atomic, Inc., P.O.Box 608, San Diego, California 92112.
161. H. L. Weidner, 185 Donabrook Court, Apt. C-12, Lexington, Kentucky 40503.
162. ORAU Library.
163-164. ORAU Fellowship Office.
165. Research and Technical Support Division, ORO.
166-167. Technical Information Center (TIC).